Hydrodynamic coefficients of a dropper line in North Sea conditions

On the drag and inertia coefficients of a Mytilus edulis dropper line submerged in water for a wide range of Keulegan-Carpenter numbers and high Reynolds numbers

L.M.D. Hendriksen

Delft University of Technology

TU Delft

Semeraro A. ILVO

Hydrodynamic coefficients of a dropper line in North Sea conditions

On the drag and inertia coefficients of a Mytilus edulis dropper line submerged in water for a wide range of Keulegan-Carpenter numbers and high Reynolds numbers

by

L.M.D. Hendriksen

Student Name	Student Number
Louk Hendriksen	4595831

Project Duration:	March, 2022 - May, 2023	
Thesis Committee	Dr.-Ing. S Schreier	TU Delft, Chair
	Dr. G. Wang	TU Delft,Supervisor
	Dr. Ir. G.H. Keetels	TU Delft, Supervisor
	Marc Huygens	Coastbusters, Supervisor

Cover: Mussel Dropper line at the Coastbusters site at De Panne by Alexia Semeraro

TU Delft

Preface

The last year has been a rollercoaster that has finally come to its destination. I am very happy that I can present this thesis report with pride. It is the cherry on the cake of my journey at the Technical University of Delft. At this place, I have grown not only as an academic student but also as a person through encountering different challenges and accomplishments. I have learned to set boundaries and push them beyond that, and have found loving friends with who I could enjoy this time that has come to an end.

I would like to thank Marc Huygens and all others that took the time for me to learn as much about the Coastbusters experiments, and the whole idea behind it. The meetings were necessary to not let the whole target of the thesis get out of sight. I am proud to have contributed to this and hope that it has an impact on the long line systems in the future.

I would also like to thank Gil Wang who I had my weekly meetings with, even at the beginning of my thesis when I was still looking for a specific subject to do my thesis about. These sessions really helped me to get the thesis to where it is now. Also, I would like to thank Sebastian Schreier, especially for the meetings. At the start the meetings were monthly but a month before the experiment until my green light meeting these meetings were weekly. This improved my process a lot, and I am very thankful for that. I would also like to thank Geert Keetels for taking the time to participate in my graduation committee, giving its input, and asking critical questions.

And at last, I want to thank my family and friends for supporting me throughout this thesis because at times there were some setbacks. You all know how much that means to me.

Enjoy reading!

L.M.D. Hendriksen
Delft, April 2023

Summary

Coastal communities around the world are facing significant challenges such as erosion, flooding, and storm surges. These issues highlight the need for nature-based coastal management solutions that can help mitigate the negative impacts of these events. Coastbusters Consortium developed such a solution in the North Sea. This solution is a system that utilizes a bivalve long line approach, where blue mussels are allowed to grow and eventually attach to the seabed, forming a reef structure that can help induce natural accretion of sand, attenuate storm waves, and reinforce the foreshore against coastal erosion. This reef structure can help to enhance coastal protection and reduce the impacts of these significant challenges on coastal communities.

To enhance the current long line system, it is imperative to develop numerical models that can accurately predict the forces acting on the slender cylinders in current and waves. One approach to this is to use the Morison equation, which accounts for both drag and inertia force. However, there is a lack of understanding regarding the drag and inertia coefficients in the literature that are used in the Morison equation. To address this issue, the present research conducts three experiments on a 3D-printed model of a dropper line, at a one-to-one scale, in a towing and wave tank. To treat the dropper line as a cylinder, a characteristic diameter is used. The 3D model is developed based on a thorough evaluation of the existing dropper lines at De Panne. These experiments aim to determine the drag and inertia coefficients for the dropper line in different steady and oscillatory flows, which can aid in the design of more efficient and effective bivalve aquaculture systems and integration into numerical models.

To determine the drag coefficient of the current towing experiments were conducted and forced oscillations and waves experiments were conducted to determine the drag and inertia coefficient in waves. The parameters used were based on the current and wave regimes at De Panne, and were expressed in terms of Reynolds and Keulegan-Carpenter numbers. The results showed that for continuous current, the drag coefficient of a dropper line containing blue mussels was determined to be C_D = 1.2 for Reynolds numbers between $3.0 * 10^4$ and $1.0 * 10^5$. In oscillatory flow, the drag coefficient varied between C_D = 2.3 - 3.5, and the inertia coefficient varied between C_M = 1 - 2.5 for Keulegan-Carpenter numbers between KC = 5 - 28.

The experiments conducted in this study included evaluations of the characteristic diameter and shape of the dropper line. Results also showed that a difference existed between the coefficients obtained from the forced oscillation and wave experiments. Possible explanations for this difference were investigated, including free surface effects and flow differences. The results obtained from this study can be applied to the design of bivalve aquaculture systems and their integration into numerical models. These findings contribute to improving the efficiency and effectiveness of nature-based coastal management strategies for mitigating the effects of erosion, flooding, and storm surges on coastal communities. Further research is needed to fully understand the complex dynamics of the bivalve long line system and its interactions with the coastal environment.

Contents

Nomenclature

Abbreviations

Abbreviation	Definition
CFD	Computational fluid dynamics
COV	Coefficient of variance
IQR	Interquartile range
LAR	Least absolute residual
MSE	Mean square error
PETG	Polyethylene terephthalate glycol
PSD	Power spectral density
PVC	Polyvinyl chloride
RMSE	Root mean square error
SSE	Sum of square
SSR	Sum of squares regression
SST	Sum of squares about the mean
VIV	Vortex-Induced Vibrations

Symbols

Symbol	Definition	Unit
a	Acceleration	m/s^2
A	Wave amplitude	m
C_a	Added mass	-
C_D	Drag coefficient	-
C_M	Inertia coefficient	-
D	Diameter	m
D_{char}	Characteristic diameter	m
D_{outer}	Outer diameter	m
f	Vortex shedding frequency	1/s
f_c	Cutoff frequency	1/s
F	Force	N
F_D	Drag force	N
F_I	Inertia force	N
g	Gravitational acceleration	m/s^2
H	Wave height	m
H_s	Significant wave height	m
k	Wave number	-
KC	Keulegan-Carpenter	-
L	Length	m
Re	Reynolds	-
R	Radius	m
St	Strouhal Numer	-
T_{avg}	Average wave period	s
T_p	Peak period	s
U	Velocity	m/s
$\dot{U}$	Relative acceleration	m/s^2

Symbol	Definition	Unit
U_b	Velocity moving body	m/s
U_C	Current velocity	m/s
U_{car}	Velocity towing carriage	m/s
U_{max}	Maximum velocity oscillation	m/s
u	Velocity water particle in x-direction	m/s
v	Kinematic viscosity	m^2/s
v_{fresh}	Kinematic viscosity freshwater	m^2/s
v_{sea}	Kinematic viscosity sea water	m^2/s
ρ	Density	kg/m^3
ω	Wave frequency	rad/s
λ	Wave length	m
θ	Polar angle	rad
σ	Standard deviation	-

1

Introduction

1.1. Problem introduction

Dunes, seawalls, and dikes currently protect most North Sea shorelines. Those measures are nature-based soft solutions or conventional solutions and provide protection from floods and coastal erosion. However, when considering climate change events such as the accelerating sea-level rise and the increasing force and rate of storms, the existing hard solutions are becoming less and less efficient in their current dimensions and configurations (Cazenave and Llovel 2010; Nicholls, Wong, and Burkett 2008). For this reason, the coastal zone needs additional measures to be taken to protect against flood disasters. Measures such as pumping stations, flood detention areas, or the heightening of current dunes, dikes, and seawalls will become unsustainable in the future due to their ecological impact and use of resources (Cheong, Silliman, and Wong 2013). For this reason, a variety of sustainable nature-based coastal management solutions are currently being explored, for example, restoring mangroves, salt marshes, and oyster and mussel reefs (Slobbe, Vriend, and Aarninkhof 2013; Day, Boesch, and Clairain 2007; Barbier and Koch 2008).

The use of ecological engineering and nature-based coastal management solutions provides a unique synergetic approach. The engineering intervention protects the inland from floods and erosion and helps the local ecosystems thrive. For example, planting mangroves to reduce the wave impact also traps sediments. Together with the mangrove roots, it forms a stabilizer preventing coastal erosion while providing shelter and a surface for diverse biology (Mcleod and Salm 2006). Hence, the strategy of ecological engineering creates benefits for society and the ecosystems through its holistic approach, as can be seen in figure 1.1.

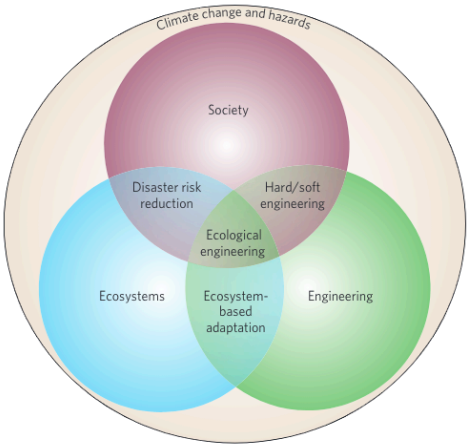

Figure 1.1: Combining strategies for coastal adaptation (Cheong, Silliman, and Wong 2013)

As figure 1.1 displays there are large benefits of ecological engineering for society and the environ-

ment, and there are lots of different applications. One of the pioneers in nature-based coastal management is Coastbusters. Coastbusters has developed solutions that offer long-term coastal resilience, embracing the naturally changing coastal ecosystem using the bivalve reefs. This progressive research project brings together the unique knowledge of Flemish companies DEME, Jan De Nul, Sioen industries, with the research expertise of the Institute for Agricultural, Fisheries, and Food Research (ILVO) and the Flanders Marine Institute (VLIZ). The project developed pioneering steps towards biogenic reefs as an additional tool for ecosystem-based flood defense (Consortium 2021).

In one of the concepts of Coastbusters, a long line system brings the *Mytilus edulis* (blue mussels) in place on the sea floor. These long line systems consist of a horizontal line on which lines are attached vertically. Those vertical attached lines are called dropper lines and contain the *Mytilus edulis*. A schematic overview of a long line system is given in figure 1.2.

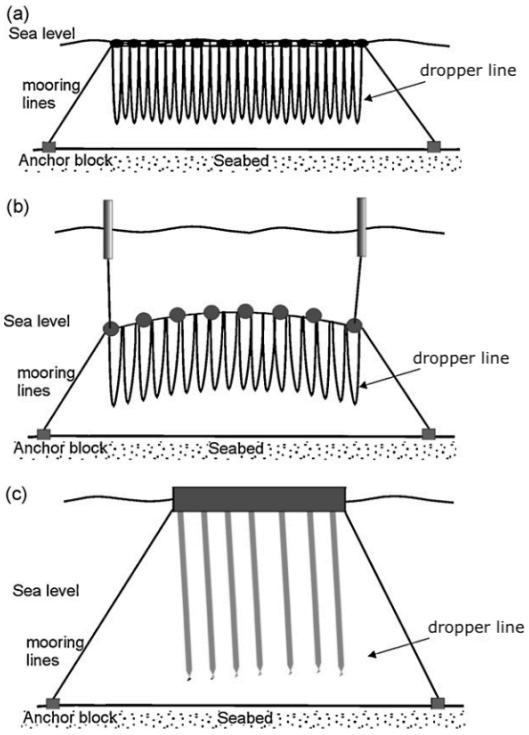

Figure 1.2: Different long line systems (Stevens, D. Plew, and Hartstein 2008)

This nature-based coastal defense concept uses the accumulation process of mussels, on the seabed, to bio-build barriers that can act as a submerged breakwater (Scyphers, Powers, and Heck 2011). The mussels are cultivated on a long line system positioned at the desired location in front of the coast. The long lines are situated parallel to the coast and anchored on both ends. The mussels attach themselves and grow on a dropper line that is vertically attached to the long line. When the mussels are fully developed, they drop onto the seabed and slowly accumulate, bio-building a reef (Cheong, Silliman, and Wong 2013).

1.2. Problem definition

The Coastbusters consortium is constantly improving its design so there is a necessity for accurate force estimations acting on long line systems. The type of long line system that is used is one with a horizontal long line on the sea surface and dropper lines vertically attached to it. A clear representation of a dropper line is shown in figure 1.3. The force estimations can be used to investigate what kind of setup is best for the specific site or to see if the materials used in the setup can be altered considering that right now mostly plastics are used. In order to create accurate models the right hydrodynamic coefficients have to be taken as input for the dropper lines, but those lack in the literature.

Figure 1.3: Clear representation of dropper lines (Prince Edward Island Aquaculture Alliance (PEIAA))

1.2.1. Gap in the literature

Different research has been conducted on the hydrodynamic behavior of the dropper lines. In table 1.1 those different researches are shown, and what the research was based on.

Table 1.1: Different shapes used according to different sources

Source	Shape
Wolfram (1985)	Cylinder with glued mussels (species not given)
Plew (2005)	Dropper line (P. Canaculis)
Raman-Nair and Colbourne (2008)	Roughened cylinder
Stevens et al. (2008)	Roughened pile
Gagnon and Bergeron (2011)	Dropper line (species not given)
Xu (2020)	Rough and sharp cylinder
Landmann et al. (2021)	Dropper line (Mytilus Edilus)

The drag and inertia coefficient of a dropper line is dependent on several components, including the aspect ratio (length/diameter), roughness, amplitude of vortex-induced vibrations (VIV), and Reynolds number (Re). Table 1.2 provides a summary of the available data on drag and inertia coefficients. Wolfram tested the effects of marine fouling on the fluid loading of cylinders and did empirical experiments using a cylinder with mussels glued on it. The data presented by Plew are based on relatively short (0.5m to 0.9m) live and physical models of mature *P. canaculis*, glued on a rope, and tested in a fixed vertical position in a flume tank (D. R. Plew 2005). Raman-Nair & Colbourne wanted to model the dynamics of a mussel long line system and modeled mussel dropper lines as rigid or flexible cylinders that were roughened, and took the drag and inertia coefficient out of the existing research on rough cylinders. In the research by Stevens, that explains the physics of open-water shellfish aquaculture, the dropper is assumed to be an ultra-roughened pile and acquires the coefficients out of empirical experiments done on roughened piles. Gagnon did research on the drag coefficient of a live dropper line by dragging a live dropper behind a boat in the ocean. The influence of waves and current were not included in the outcome. Xu investigated the drag and wake of a long-line mussel dropper under tidal current, where a computational fluid dynamics analysis was done on a rough and sharp cylinder. The most recent experiment was conducted by Landmann, which investigated drag and inertia coefficients of live and surrogate shellfish dropper lines under steady and oscillatory flow. This was done by empirical experiments in a wavetank (Landmann et al. 2021).

Table 1.2: Different C_D, and C_M for steady and oscillatory flow according to different sources

	Steady flow		Oscillatory flow			
Source	C_D	$Re(*10^4)$	KC	$Re(*10^4)$	C_D	C_M
Wolfram (1985)	1.2	0.1 - 20	-	-	-	-
Plew (2005)	1.1	0.4 - 1.2	-	-	-	-
Raman-Nair & Colbourne (2008)	1.2	-	-	-	-	-
Stevens et al. (2008)	1.7	-	-	-	-	-
Plew et al. (2009)	1.27	1 - 7	-	-	-	-
Gagnon and Bergon (2011)	1.25	3.5 - 10	-	-	-	-
Xu (2020)	1.1-1.2	0.39 - 10	-	-	-	-
Landmann et al. (2021)	1.6	2.3 - 14	1.5 - 7.5	-	2.3	2.1

The data presented in table 1.2 show that the coefficients coherent to a dropper line in oscillatory flow are fairly unexplored. Only in the studies of Landmann inertia is taken into account as well. Currently, this is the only research where the inertia coefficients are examined by submerging it into the oscillatory flow (inertia) instead of only a steady current (drag).

1.3. Research objective

Therefore, the efforts in this thesis are focused on finding the drag and inertia coefficient and investigating the drag and inertia forces on a model representing the dropper line at the site of Coastbusters near De Panne, Belgium. These hydrodynamic coefficients are to be found by conducting experiments.

1.3.1. Research question

Following the previous work done, the research question for this study can be formulated as:

What are the drag and inertia coefficients of a dropper line in flow with high Reynolds and intermediate Keulegan-Carpenter numbers?

To answer this, the following sub-questions are formulated:

1. How do the results compare to the literature?
2. What defines the difference between forced oscillation and wave experiments?

1.3.2. Modelling the problem

In this study, three methods for acquiring drag and inertia coefficients are discussed, namely analytical, numerical, and physical experiments. Based on the analysis of the different experimental methods, is concluded that physical testing is the most appropriate approach, and therefore, three different experiments are conducted to obtain the correct values of these coefficients.

For the drag coefficient experiment, the current speed is varied to acquire accurate values. Additionally, two experiments are performed to acquire the drag and inertia coefficients in an oscillating environment using waves and forced oscillations with varying wave amplitudes and periods. The effects of waves, free surface effects, and end effects are considered, which depend on the dimensions of the cylinder (Brennen 1982; Rockwell, Ozgoren, and Saelim 2004). To minimize the interference of surface effects, bottom effects, or wall effects, the model will be a rigid cylinder-like shape in a water-filled basin with dimensions following the ITTC guidelines (ITTC 2014), and end plates will be attached to both sides of the cylinder in order to keep the flow two dimensional.

The experiments will be conducted at a one-to-one scale for Reynolds number (Re) and Keulegan-Carpenter number (KC). The flow will be uniform, unidirectional, and with constant current and the waves are unidirectional waves in the same direction.

2

Theoretical background

In this chapter, the theory and different aspects of the experiments are discussed to set up the design parameters for the experiments. First, the theory of the forces acting on the long line system is explained, and then the theory of the drag and inertia coefficients separately. At last, is discussed it can be applied to the preparation of the experiments.

2.1. Forces due to real fluids

In 1950 J.R. Morison, J. Johnson, and S. Schaaf developed a semi-empirical equation of the forces on a cylinder in an oscillatory flow called the Morison equation. The equation was developed by using experimental results and the equations of velocity and accelerations of water particles due to waves. The Morison equation consists of two out-of-phase force components:

- drag force that is proportional to the velocity squared
- an inertia force that is proportional to the horizontal component of the acceleration

The Morison equation is shown in equation 2.1. It requires both a known drag and inertia coefficient, which are often obtained empirically or from approximations (Morison, Johnson, and Schaaf 1950).

$$F = \frac{1}{2}\rho D L C_D U|U| + \frac{1}{4}\pi\rho D^2 L C_M \dot{U} \tag{2.1}$$

where:

D	=	diameter (m)
L	=	length (m)
C_D	=	drag coefficient (-)
ρ	=	density (kg/m^2)
C_M	=	water depth (m)
$\dot{U}$	=	m/s^2

The Morison equation contains both a drag and an inertia component. The L denotes the length of the cylinder, but over a longer cylinder, the L is taken in shorter ranges, because the drag and inertia coefficient change over the length as well. Both are multiplied by either the drag or inertia coefficient. The coefficients depend on the shape, roughness, and flow characteristics.

2.2. Drag coefficient

Equation 2.2 shows how the drag coefficient is calculated, where F_D denotes the drag force, ρ the density, U the relative velocity between the water and the cylinder, and D the diameter. The C_D is used to find the drag forces. The drag coefficient has a different value if the flow changes between

laminar and turbulent flow. Therefore it is often expressed in terms of Reynolds, which is based on the speed of the surrounding medium.

$$C_D = \frac{F_D}{0.5\rho U^2 D} \tag{2.2}$$

2.2.1. Reynolds number

The Reynolds number (Re) is named after O. Reynolds who studied laminar and viscous flows and the transition between these flows. It is an important parameter in fluid dynamics because it helps predict the onset of turbulence. A low Reynolds number indicates a laminar flow, while a high Reynolds number indicates a turbulent flow. The formula of Re is shown in equation 2.3, in which v denotes the kinematic viscosity of water and U_c is the relative current velocity.

$$Re = \frac{U_c D}{v} \tag{2.3}$$

It has been stated in research that the drag coefficient depends on the Reynolds number, the geometry, and the surface roughness (Clancy 1975). When research continued it was discovered that it also depends on oscillations in the flow. This means that in regular waves, the U_C is replaced by the water particle velocity u, calculated in equation 2.4. The water particle velocity is based on the linear wave theory which means that the amplitude of the wave should be small compared to the wavelength (ak<2 π). The wave particles may not penetrate the bottom or leave the surface, and the waves may only be subjected to gravity (Holthuijsen 2007).

$$u = \frac{agk}{\omega}\frac{cosh(kz + kd)}{cosh(kd)}cos(kx - \omega t) \tag{2.4}$$

$$a_x = agk\frac{cosh(kz + kd)}{cosh(kd)}sin(kx - \omega t) \tag{2.5}$$

where:

ω	$= \frac{2\pi}{T}$	$=$	wave frequency (rad/s)
k	$= \frac{2\pi}{\lambda}$	$=$	wave number (rad/m)
z		$=$	elevation (+ is upward) from the still water level (m)
H		$=$	wave height (m)
d		$=$	water depth (m)
T		$=$	wave period (s)
λ		$=$	wave length (m)
a		$=$	amplitude of the wave (m)
u		$=$	velocity water particle in x direction (m/s)
g		$=$	gravitational acceleration

2.3. Inertia coefficient

The inertia coefficient is expressed as C_M, and is used to find the inertia forces. Equation 2.6 shows how to calculate the inertia coefficient, where F_I is the inertia force, and $\dot{U}$ is the relative acceleration.

$$C_M = \frac{F_I}{0.25\pi\rho\dot{U}D^2} \tag{2.6}$$

The inertia coefficient of a body in a fluid medium is composed of two distinct force components, namely the Froude-Krylov and added mass forces. The Froude-Krylov force can be understood by visualizing the body being replaced with an equivalent volume of water in waves, which would experience

an acceleration and thus a force. This force would be equivalent to the Froude-Krylov force acting on the body and can be calculated by integrating the pressure of the incident wave over the surface of the body, unaffected by its presence. This can be seen in equation 2.3 where v is the velocity of the cylinder.

$$F = \rho\frac{1}{4}\pi D^2\dot{u} + \rho C_a\frac{1}{4}\pi D^2(\dot{u} - \dot{v}) + \frac{1}{2}\rho C_D D \tag{2.7}$$

In this equation, the first term is the Froude-Krylov force, and the second term is the hydrodynamic mass force. So the inertia force is made up of two components. When these two forces are rewritten the inertia coefficient is as in equation 2.8.

$$C_M = 1 + C_a \tag{2.8}$$

On the other hand, the added mass component of the inertia coefficient is due to the distortion of the fluid flow caused by the presence of the body. This effect can be seen by considering a body accelerating through a stationary fluid, where the added mass force can be interpreted as the extra force per unit acceleration compared to the situation in air.

The force around an oscillating cylinder in still water is not identical to that of an oscillating flow past a fixed cylinder. This is because there is no ambient dynamic pressure gradient in still water so the Froude-Krylov is now equal to zero. However, another force is added due to the forced oscillations. In this situation, there also has to be accounted for the mass times the acceleration of the cylinder in the air compared to water.

The inertia coefficient is often expressed in terms of Reynolds and Keulegan-Carpenter numbers. Before 1958, the oscillatory properties of the flow related to the structure were not extensively described. G.H. Keulegan and L.H. Carpenter discovered how to describe this, which is now given by the Keulegan-Carpenter number (KC) (Keulegan and Carpenter 1958). This number is shown in equation 2.9, in which u is the relative water particle velocity, T is the wave period, and D is the diameter.

$$KC = \frac{uT}{D} \tag{2.9}$$

The numerator is proportional to the motion. When the KC is small, the orbital motion of the water particles is as well, which means that the waves are low compared to the cylinder. This number can predict flow patterns (Dhanak and Xiros 2016). In 1950 Morison, Johnson, and Schaaf found that the drag coefficient does not only depend on the Re, and Keulegan and Carpenter showed that it depends on the KC number as well.

The KC number can also be used to determine whether the drag of inertia is dominant in the Morison force. The rule for this is that if KC is less than 3 the inertia is dominant and the drag can be disregarded, and if the KC is higher than 40 the drag is dominant and the inertia can be disregarded. In the region between 3 and 40, both play a role. This can be seen working out the ratio of the amplitudes of the drag and inertia forces. The phase difference is neglected here. Where $\dot{U} = 2 * \pi/T * u_a$

$$\frac{F_{Da}}{F_{Ia}} = \frac{\frac{1}{2}\rho C_D D u_a|u_a|}{\frac{\pi}{4}\frac{2*\pi}{T}C_M D^2\omega u_a} \tag{2.10}$$

Which can be rewritten as:

$$\frac{F_{Da}}{F_{Ia}} = \frac{1}{\pi^2} * \frac{C_D}{C_M} * \frac{u_a * T}{D} \tag{2.11}$$

Where the KC can be applied:

$$\frac{F_{Da}}{F_{Ia}} = \frac{1}{\pi^2} * \frac{C_D}{C_M} * KC \tag{2.12}$$

So for lower KC numbers, the drag force becomes less significant, which can be explained by that the flow does not travel far enough relative to the cylinder diameter to generate much of a boundary layer. For higher Kc numbers the inertia force becomes less significant which can be explained by that the vortex shedding frequency becomes high compared to the wave frequency so the flow tends to behave more and more like a uniform flow.

2.4. Translation from study to experiment

The Re and KC numbers describe tidal current and wave regimes. These can translate site-specific parameters to parameters for a lab environment to come up with the right conditions for the experiments. So, equation 2.3 and 2.9 are used for calculating the Re and KC that are related to the site. With these values, the correct parameters for the experiment can be computed.

3

Environmental background

This chapter elaborates on the environmental conditions to see in which kind of steady flow and oscillatory flow the longline system is situated. The theory of chapter 2 is used to describe this. First, the location is shown with all its parameters regarding waves and currents. These parameters are used to define the drag and inertia wave regimes of the site. Lastly, this data is translated to Re and KC values.

3.1. Environmental conditions De Panne

The location of the site is near De Panne in Belgium. There is both a sheltered site (closer to shore and in between two sandbanks) and an unsheltered site (further in the sea). For this research, the unsheltered site is chosen due to the more offshore environment with no influence of sandbanks, which is more applicable to other ocean environments as well. Coastal management for breaking waves is more relevant in an offshore environment than in an onshore environment. For both sites, there are different measurement stations, for the unsheltered site the 'Trapegeer' buoy is used for the measurements as seen in figure 3.1.

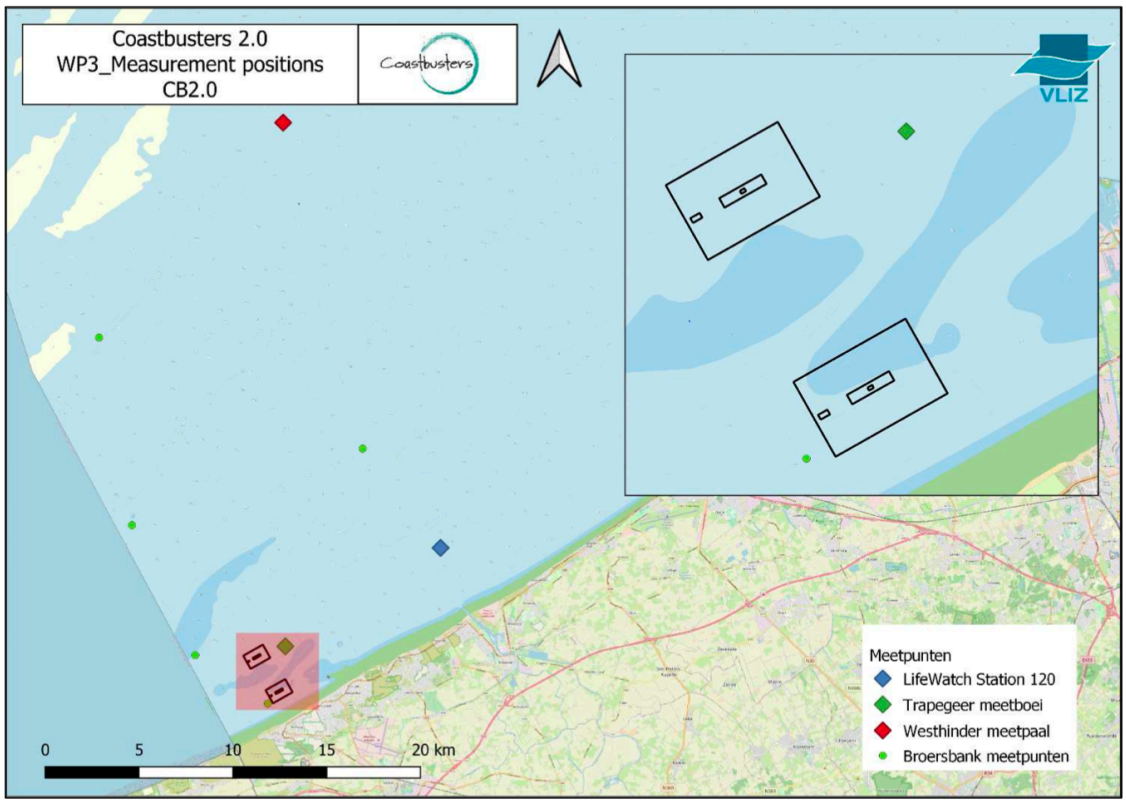

Figure 3.1: Location of the Coastbusters setup and measurement stationsLangedock, Johnen, and Pirlet 2020

3.1.1. Wave Data

The significant wave height, the 10 % highest waves, the wave period, and the height of the swell are recorded every 15 minutes. These data records are given monthly in Table 3.1. As can be seen in table 3.1, the wave height occasionally exceeds three meters during heavy winter storms from November to February. During the summer, from June to September, the significant wave height is below 1 meter at most times and rarely exceeds 1.5 meters. In the spring the wind speeds get higher and the waves exceed 2 meters regularly.

Table 3.1: Wave heights Trapegeer (Langedock, Johnen, and Pirlet 2020

	Jan	Feb	Mar	Apr	May	Jun	Jul	Aug	Sep	Oct	Nov	Dec
Maximum H_s [cm]	327	272	262	306	223	201	191	197	218	252	321	337
Average H_s [cm]	67	59	59	49	48	54	49	48	56	68	69	72
Median H_s [cm]	48	52	43	42	39	50	43	41	46	56	56	58
10th percentile H_s [cm]	20	17	17	17	18	22	27	21	26	30	25	26
90th percentile H_s [cm]	142	112	123	91	91	89	81	84	99	123	129	134

3.1.2. Tidal current

In figure 3.2 the tidal current data for the three years between 2017 and 2020 is given both in the surface current and in the bottom current. The current is either a northeasterly (NE) current or a southwesterly (SW) current, since the currents run parallel to the Belgian coast. The current goes up to the 1.2 m/s on the surface in the NE direction and in the SW direction it goes up to 0.8 m/se. The same counts for the bottom current where the NE direction goes up to 0.6 m/s and in the SW direction goes up to 0.4 m/s.

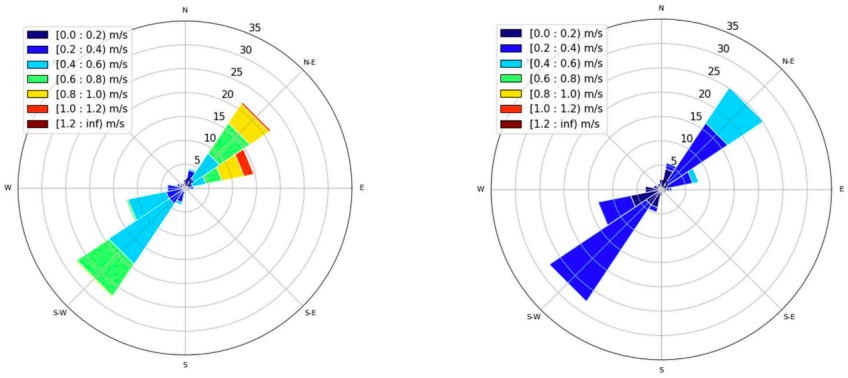

(a) Surface current at the site (Langedock, Johnen, and Pirlet 2020)

(b) Bottom current at the site (Langedock, Johnen, and Pirlet 2020)

Figure 3.2: Current at the site

3.1.3. Wave period

The wave period between January 2019 and January 2020 can be seen in Table 3.2. The maximum wave period is 6.2 seconds, but the overall average wave period is between 3 and 4 seconds.

Table 3.2: Wave periods Trapegeer (Langedock, Johnen, and Pirlet 2020)

	Jan	Feb	Mar	Apr	May	Jun	Jul	Aug	Sep	Oct	Nov	Dec
T_{avg} (s)	3.80	3.26	3.63	3.29	3.47	3.19	3.26	3.03	3.36	3.40	3.63	3.33
T_{max} (s)	5.85	6.20	6.09	5.09	5.58	6.08	5.30	4.18	5.07	5.96	6.45	5.48

3.1.4. Drag and inertia wave regimes

To see by what wave force regime the system is affected the Chakrabati scheme can be used (figure 3.3). It clearly displays the relation between the diameter of a cylinder, the wave height, the wavelength, and what kind of forces are active. The diameter of the dropper line varies between 2 to 30 cm, but the average diameter is 12 cm. The wave height varies between 7 and 304 cm and the wavelength between 6.4 and 41.5 meters. Based on these numbers the total domain possible is displayed as a red triangle in figure 3.3 (Bergdahl 2017).

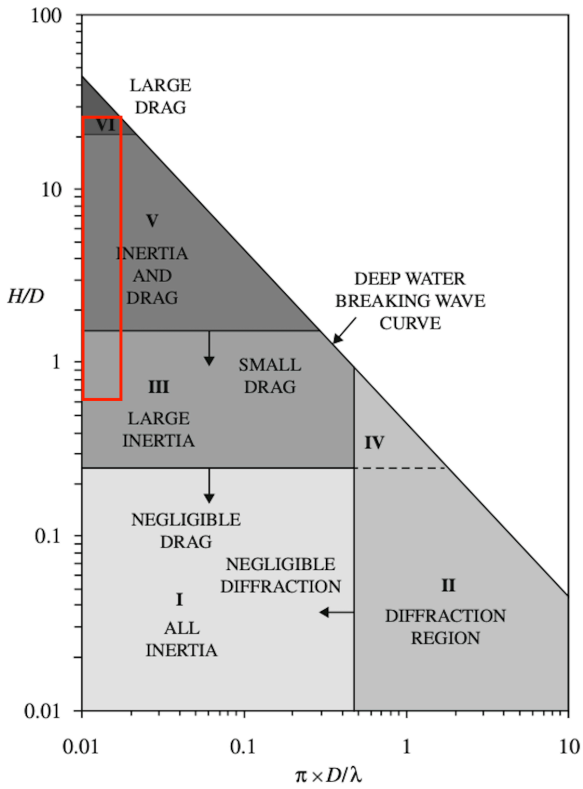

Figure 3.3: Different wave force regimes (Chakrabarti 1987)

The Chakrabarti scheme shows that there is a necessity for both the inertia and drag coefficients in an oscillating flow. The drag induced by the tidal current shows the necessity for a drag coefficient in a steady flow. A physical experiment is needed to come up with these coefficients.

3.2. Translation to experiment

In order to conduct experiments in a laboratory, it is necessary to calculate the values of KC and Re based on the parameters at the site, so that they can be translated to the parameters in the lab. The tidal current data is used to determine the parameters for towing experiments, and it is observed that the current does not exceed 0.8 m/s, as shown in table 3.2a. This results in a maximum Reynolds number of $1.0 * 10^5$ using equation 2.3. A histogram is constructed using the total current data of a year to determine the probabilities of the current state, as illustrated in figure 3.5a.

The wave heights and periods used as test parameters in the laboratory experiments are based on operational conditions. In this case, the average 90th percentile of the significant wave height over a year is used, resulting in a wave height of 108 cm. The corresponding wave periods are chosen based on the wave height of the waves at the site, as shown in figure 3.4. This selection of wave parameters ensures that the laboratory experiments closely replicate the real-world conditions at the site, which is crucial for accurate testing and reliable results.

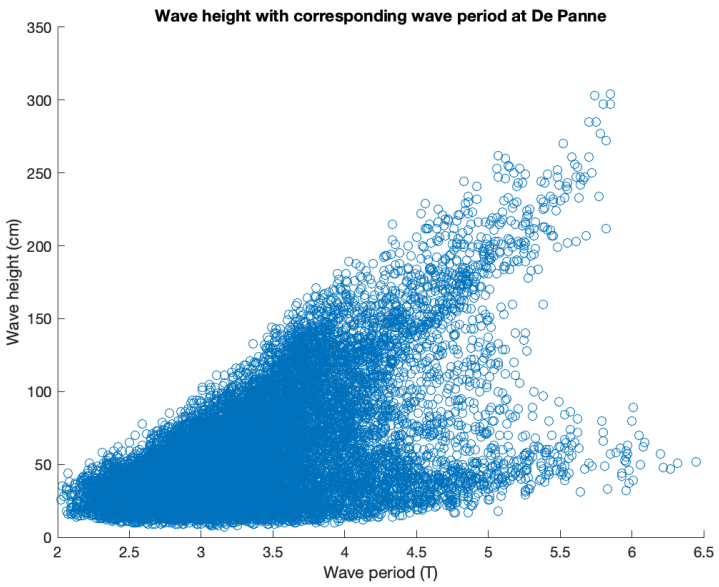

Figure 3.4: Wave height and period data of the Trapegeer buoy at De Panne

Figure 3.4 clearly illustrates that there are no blue dots above a certain wave height and period due to the maximum steepness limit. The 90th percentile of the waves, as shown in table 3.1, is on average at H = 108 cm. It is chosen to use this as the maximum for the amplitude of waves, while this covers most of the waves, so for the serviceability limit-state design conditions. The ultimate limit-state is too hard to test for due to the limit in space in the laboratory and the complexity of scaling the model. These specific wave heights and periods are then utilized to calculate the corresponding values of Re and KC at the site, with an average dropper line diameter of 0.12 m.

The Reynolds number is calculated using equation 2.3, where the velocity is determined by the wave particle velocity computed from the wave height and period, as per equation 2.4. The depth is chosen to be 1.5 m, which is half the length of the dropper line. On the other hand, the KC is calculated utilizing equation 2.9 with the same wave particle velocity. This process yields a range of KC and Re values for the waves displayed in figure 3.5b.

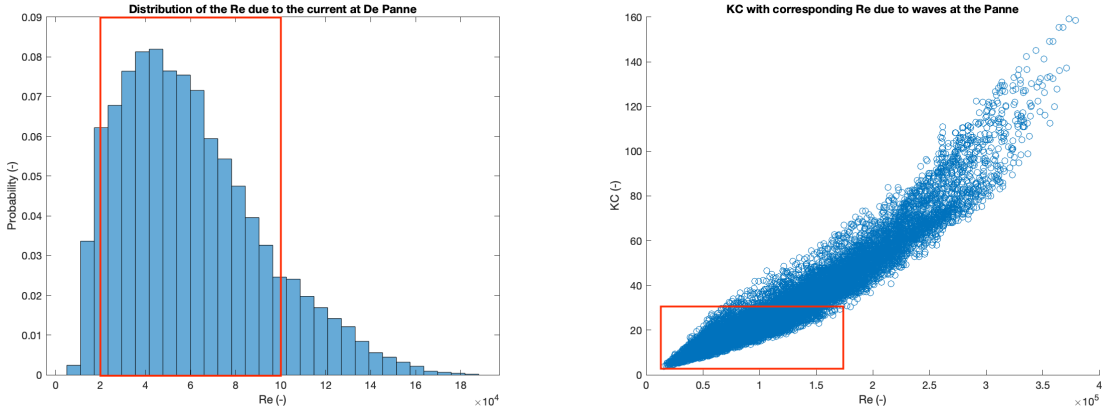

(a) Distribution of the Reynolds values of the current at De Panne

(b) KC with corresponding Re at De Panne

Figure 3.5: Current and waves at De Panne expressed in Re and KC'

Figures 3.5 depict the different regimes that require testing as red rectangles. These are combined with the data presented in table 1.2. Landmann had left off at a KC value of 7.5, which is where this research will commence. This is illustrated schematically in figure 3.6. These values of Re and KC

numbers will be the focus of the experiments and are presented in table 3.3. These values represent the range of conditions that are relevant for understanding the dynamics of waves and currents at the site. The experiments conducted within this range will provide valuable insights into the physical phenomena involved, allowing for better modeling and prediction of wave and current behavior.

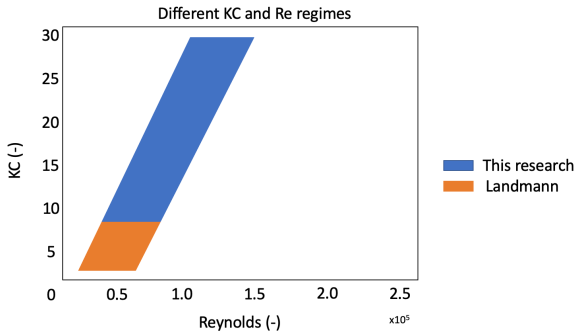

Figure 3.6: The visualized gap in existing research

Table 3.3: Re and KC numbers considered in the current research

	Current	Waves
Re $(*10^5)$	0.3 - 1.0	0.5 - 1.5
KC	-	10 - 25

4

Experiment

To empirically determine the unknown drag and inertia coefficients, an experiment was conducted following a systematic approach. First, the experimental method was carefully selected, taking into consideration the research objectives and limitations of the available facilities. The modeling of the dropper line model was also thoroughly prepared, with choices made to ensure the model was as realistic as possible. Using the model and relevant information from relevant chapters 2 and 3, the appropriate parameters were determined for the correct KC and Re. Once the model and experimental parameters were established, the remaining setup was designed. Finally, the steps during the experiment conduction are discussed.

4.1. Experiment methodology choice

There are three main methods of modeling a problem in the field of hydrodynamics: analytically, empirically, or using simulations. All these methods have their up and downsides. Experiments have their problems but do obtain their results successfully (Boccotti, Arena, and Fiamma 2013; Sarpkaya 1976). Due to the high Reynolds numbers, combined with free surface effects and waves, analytical methods such as the linearized Navier-Stokes equation or using potential theory are not viable options (Streeter and Wylie 1979). Simulation of a cylinder in high Reynolds numbers flow is known to be problematic (Sreenivasan and Iyer 2019). Computer programs that use empirical or semi-empirical solutions are also used, such as VIVA, VIVANA, and SHEAR7. The problem is that these methods still give results with large uncertainties, sometimes safety factors of 10 to 20 are required (Wang, Fu, and Baarholm 2014). As experiments can give the most accurate results, these are chosen as the main method.

To determine the drag coefficient in steady flow a current can be simulated by towing the dropper line model with a towing carriage in a towing tank. The methods to determine the drag and inertia coefficients in oscillatory flow are waves simulated by a wave maker in a wave tank or forced oscillations by for example a linear motor. In this research, it was chosen to conduct the experiments on a one-to-one model. The model is not downscaled because the acceleration and velocity would become too large due to the scaling of the Reynolds numbers.

4.2. Test facility

There are different test facilities present at the Department of Maritime and Transport Technology, but only wave tank 2 was available during the time of this research. The test facility will have to be able to simulate current, allow for free surface effect, generate waves, and have the right dimensions to allow for the required waves and Reynolds numbers. Also, it needs enough space for horizontal or vertical linear forced oscillations. The test facility that is available at the Department of Maritime and Transport Technology at the Delft University of Technology is towing tank 2. The tank is equipped with a single-paddle wavemaker used in piston-type mode and a wave-damping beach at the other end. The specifications are displayed in table 4.1.

Table 4.1: Specifications of wave tank 2

Facility	U_{max} (m/s)	λ (m)	Max depth (m)	B (m)	L (m)
Towing tank 2	3	0.4 - 20	1.25	2.75	85

The specifications of the tanks dictate the maximum and minimum values of Re and KC at which can be tested. The width of the tank should be 2.4 times the diameter of the cylinder according to ITTC (ITTC 2014), as wall effects will influence the results if there is not enough distance between the cylinder and the walls. The Reynolds number is dictated by the maximum velocity that can be simulated. Other limitations are based on the maximum forces that are allowed on the carriage of the towing tanks.

Using the values obtained, a design and test ranges that fall within the limits are calculated. The cylinder's diameter, underwater length, and maximum current velocity were chosen in these calculations to satisfy boundary conditions. As there are assumptions within the calculations, they are shown in detail. The limitations of the wave maker are shown in figure 4.1.

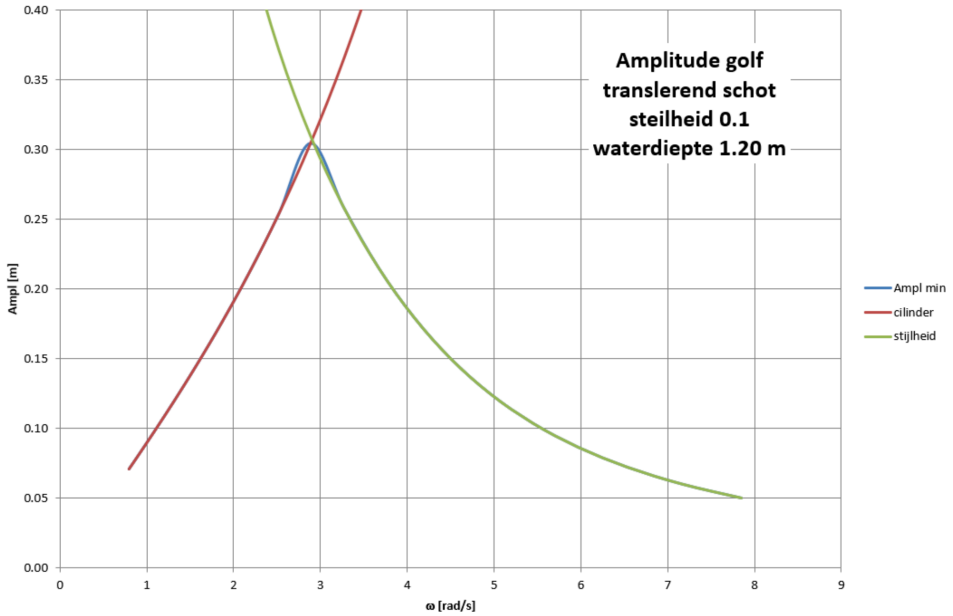

Figure 4.1: Limitations for waves produced by the wave maker from Dr. ing. S. Schreier

This figure shows the maximum amplitude that can be reached per radian frequency for a wave steepness of 0.1 and a water depth of 1.2 m. The waves are limited by their shape. When the waves become too steep they will break. The region beneath the red line before intersecting with the green line and the region beneath the green line after intersecting with the red line is able to be produced.

4.3. Horizontal orientation

The model is situated in the wave tank in a horizontal position, because the space was too limited for a vertical orientation, because of the linear oscillations. Since the coefficients are based on the shape of the model it is not a problem that it is horizontally orientated. Only for the wave testing the orientation does matter, which is explained in appendix B.2.

4.3.1. Reynolds number for towing

The Reynolds number is calculated using equation 2.3. In the equation, U_{max} is the maximum towing velocity, D is the characteristic diameter of 0.12 m, elaborated further on in section 4.4.4, and v the dynamic viscosity. The dynamic viscosity of freshwater at a temperature of 17 °C gives a value of v = $1.05{\cdot}10^{-6}$ m^2/s (ITTC 2014).

$$Re = \frac{U_{max} D}{v} \tag{4.1}$$

This gives a maximum value for the Re number of $3.4 * 10^5$. While the maximum Re determined in section 3.2 was $1.0 * 10^5$.

4.3.2. KC and Re numbers for waves

The KC number has been calculated using equation 2.9, where u is the velocity of the water particle, and calculated using equation 2.4 combined with the wave maker limitations of figure 4.1. The KC and Re numbers of the waves by the wave maker are plotted in figure 3.5b to see what the limitations are.

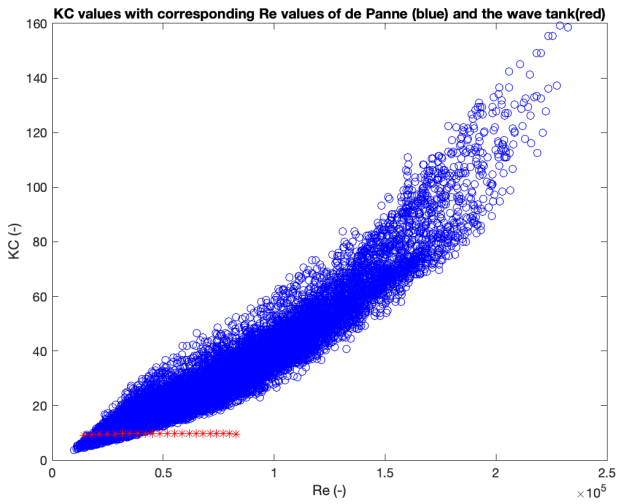

Figure 4.2: KC values with corresponding Re values of de Panne (blue) and the wave tank(red)

The red crosses in figure 4.2 are based on the limitations of the wave maker. It can be observed that the maximum KC values that the wave maker can produce are around 12, and the Re values do all suffice. However, for this particular research, the KC values of the waves produced by the wave maker are not high enough, and thus another method is used. To create higher amplitudes, the model will be oscillated horizontally by a linear motor.

4.3.3. KC and Re numbers for oscillations

The use of a linear motor means that there are no limitations on the velocity and acceleration of the model, so there are no restrictions on the range of Re values that can be tested. However, there is a limitation on the available space for the experiment due to the movement of the model in the water beneath the towing carriage. The linear motor used in the experiment has a stator that measures 2000 mm, and the guide rails are 3380 mm in length. A model carriage is used to hold the model and attach it to the guide rails, with a length of 880 mm. The stator is capable of extending over the edge of the carriage on the left side. The available space between the model carriage, the linear motor, and the towing carriage is illustrated in figure 4.3.

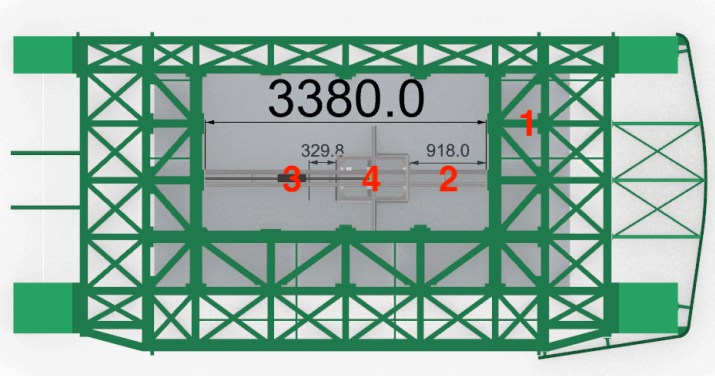

Figure 4.3: The available space for oscillations on the carriage (dimension given in mm) 1. Towing carriage 2. Guide rails 3. Linear motor 4. Model carriage

In this figure can be seen that the distance the model carriage can move to the left before it reaches the linear motor is 330 mm, and the distance it can move to the right before it reaches the towing carriage is 918 mm. This means that the total oscillation length is 1248 mm. The amplitude concluded from section 3.2 was 108 cm, so there is no limitation in space for forced oscillations.

4.4. Model

It was not possible to use a real dropper line for the experiments due to issues like dying on the journey to the wave tank or in the freshwater of the wave tank. Different options were reviewed to come up with the most realistic model for a dropper line like making a mold of a dropper line. Eventually, the model was made in Rhinoceros, which is a 3D computer graphics and CAD software program, to design a 3D printable model based on the real dropper lines of the Coastbusters setup and on the little literature on mussel growth on dropper lines.

4.4.1. Spatial organization mussels

To obtain a comprehensive understanding of the spatial organization of a mussel dropper line, several variables must be considered, including the diameter of the rope, the length, and the number of mussels, as well as their cylindrical-polar coordinates and orientation. The cylindrical-polar coordinates of a mussel on a rope are defined by the radius, height, and polar angle of a reference point on the mussel. The orientation of the mussels can be described by three rotations: pitch, yaw, and roll, relative to the rope.

The pitch rotation is the angle between the longitudinal axis of the mussel and the circumferential plane of the rope. The yaw rotation is the angle between the longitudinal axis of the mussel and its polar radius after the pitch rotation. The roll rotation is the angle between the plane of symmetry of the mussels and the longitudinal axis of the rope after the pitch and yaw rotations. These rotations provide a complete description of the orientation of the mussels relative to the cylindrical-polar coordinates system.

In addition, the number of byssus threads per mussel should be considered, as they are used to attach the mussels to neighboring mussels and to the rope. By describing these variables, a detailed understanding of the spatial organization of a mussel dropper line can be obtained. These terms and coordinates are shown in figure4.4.

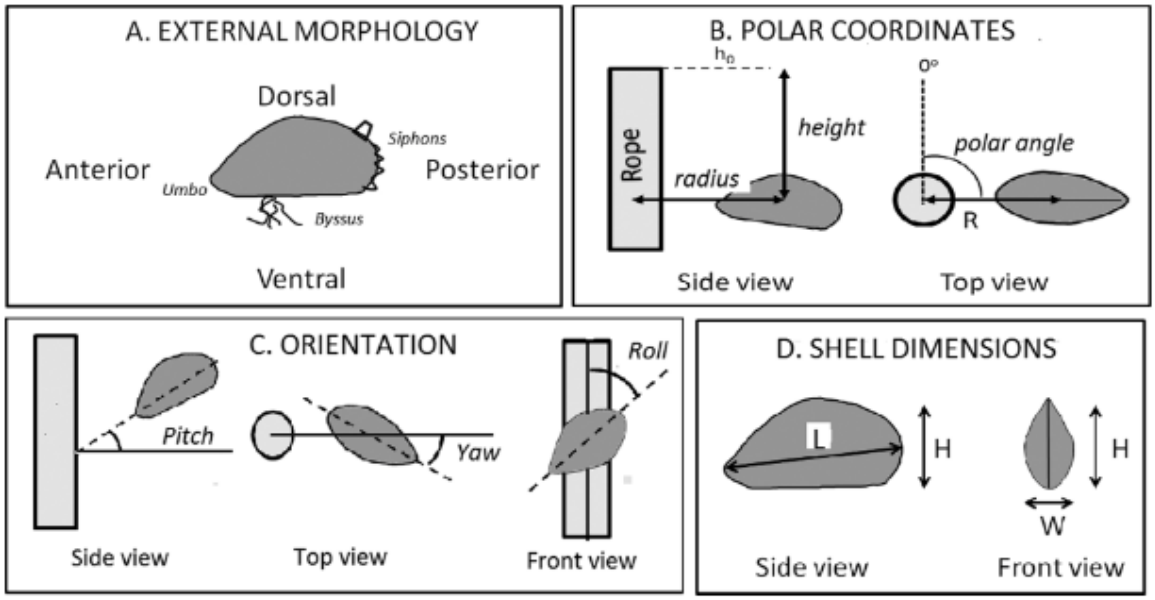

Figure 4.4: A) External mussel morphology. B) Mussel polar coordinates relative to the rope axis; R = Polar radius. C) Mussel orientation relative to the rope axis. D) Shell dimensions: L = length, H = height, W = width (Gagnon 2019)

Research on the spatial organization of dropper lines is relatively limited. However, based on available studies, it appears that in a side view of the collector, the arrangement of mussels appears as rows oblique to the rope's axis, with approximately 6-8 mussels per turn (360°). Mussels are oriented with their anterioposterior (length) axis perpendicular to the rope, with the umbo towards the rope and the siphons towards the exterior (pitch=0°). The plane of symmetry of most mussels is within 30° of being parallel to the rope axis, with the ventral side facing either upwards (roll=0°) or downwards (roll=180°). In the case of half-grown collectors, the mussels form rows that are parallel to the rope's circumference, and some parts of the suspensions may be multilayered (Gagnon 2019).

4.4.2. Application of theory to the model

In this study, seven different mussels are used that were selected because of their variation in length, height, width, and shape. These mussels are all of the species *Mutilus Edulis*, and they were collected from the province of Zeeland. The dimensions and shapes of those seven mussels are shown in appendix E.

A dropper line typically consists of multiple layers of mussels, and this study focuses on a bi-layered dropper line since it is the most common. The mussels attach to each other, and to determine at which point the second layer starts, the mean length is calculated of the seven mussels. This mean length was found to be 54 mm, and the diameter of the rope where the first layer of mussels attaches is 22 mm.

The layout of the bi-layered dropper line is shown in figure 4.5, where the dotted lines represent the seven different mussels, and the circles represent the bounds of the first and second layers of mussels. By using these representative mussels and a bi-layered dropper line outline insight is gained into the spatial organization of mussel suspensions.

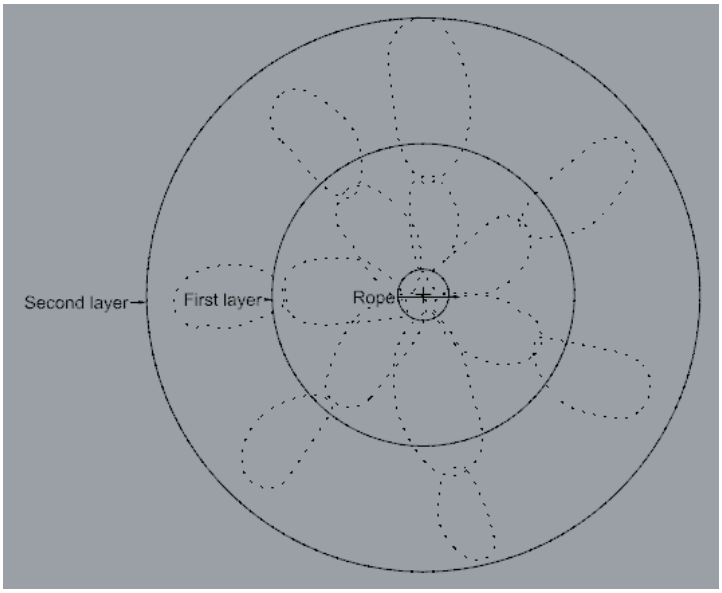

Figure 4.5: Layout of the bi-layered dropper line used in this study, where the dotted lines represent the seven different mussels and the circles represent the average bounds of the first and second layers of mussels.

To determine the range of the number of mussels that attach per row in a dropper line, Gagnon reports that the bi-layered population (second layer of mussels) is twice that of the mono-layered population (first layer of mussels). Therefore, the largest and smallest mussels were modeled in the first layer to determine the range of the number of mussels per row. The amount obtained from the modeling was then multiplied by two to give the minimum and maximum amount of mussels per row, as shown in figure 4.6.

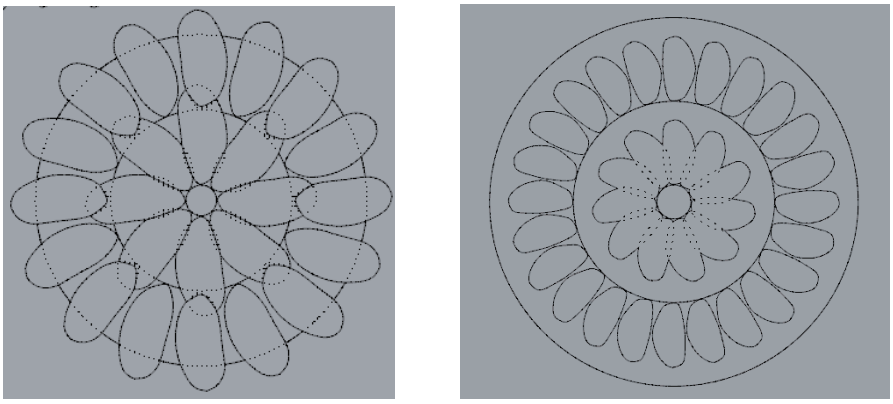

(a) Largest mussel on both first as the second layer, where the first layer contains 8 mussels and the second layer 16 mussels

(b) Smallest mussel on both first as the second layer, where the first layer contains 11 mussels and the second layer 22 mussels

Figure 4.6: Maximum and minimum numbers of mussels per row

4.4.3. Dropper line

The dropper line used in the Coastbusters setup has a length of 3 meters and an average diameter of 15 cm, which is similar to the bi-layered outline given in figure 4.5. Based on Gagnon's research and the images of the dropper line provided by Coastbusters, a 3D specimen was designed in Rhinoceros. Figure 4.7 shows an example of the dropper line with dimensions added.

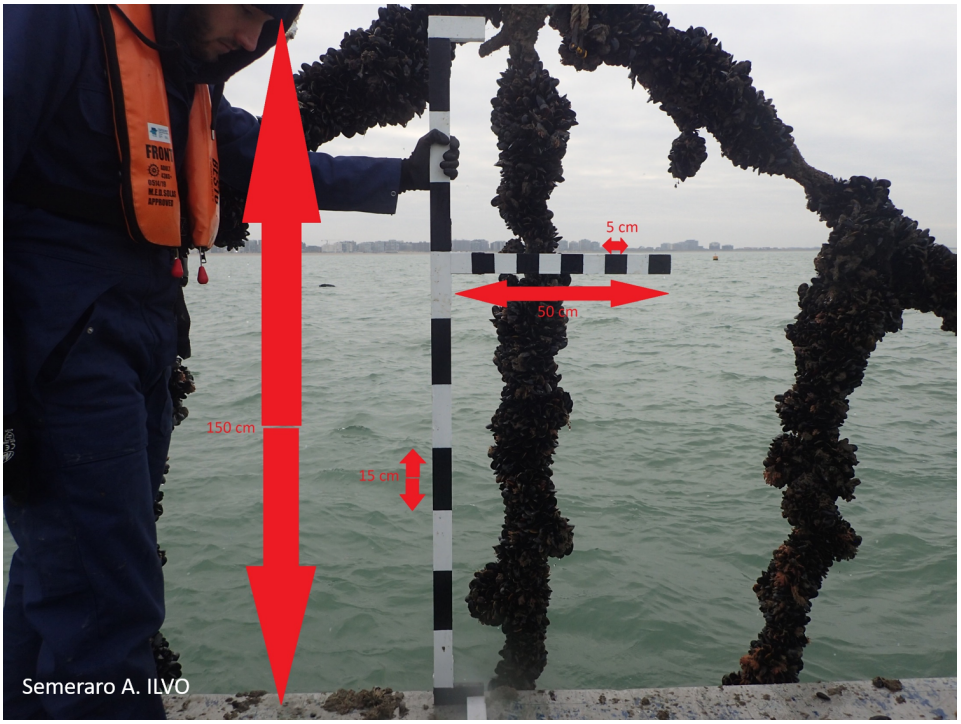

Figure 4.7: Dimensions of the dropper line of the Coastbusters setup

The 3D model of the dropper line was designed with a segment length of 10 cm, as the 3D printer had a height limitation of 15 cm. The development of the model is shown in figure 4.8, which includes the dropper line it was based on, the Rhinoceros model, and the final 3D printed model of the dropper line. However, unlike a real dropper line, which varies in diameter over its total length and contains soft growth like algae between the mussels, the 3D model does not incorporate these features, as it would further complicate the structure.

(a) Dropper line of 0.5 m **(b)** Rhino model of the dropper line of 0.5 m **(c)** 3D printed model of 0.5 m

Figure 4.8: The development of the model

4.4.4. Characteristic diameter

Due to the irregular shape of the dropper line, its diameter is not like a circular cylinder due to the mussel shape. If its outer diameter is used in the Morison equation the computed forces will be too high. To tackle this problem the characteristic diameter of a dropper line is determined (Gagnon and Bergeron 2017). There are four different approaches to determine this:

1. Average diameter: over the length of the dropper line the diameter is measured several times and then divided by it amount of measurements taken
2. The multiple of mussel length: twice the amount of average mussel length is taken
3. Spatial organization model: it works by defining relationships between mussels and the spatial arrangement of these mussels
4. Displaced volume method: the diameter is calculated based on the total volume of the dropper and its length.

In this research, the characteristic diameter is calculated based on the displaced volume method. While in a design program, the volume of a model is accurately calculated. For a dropper, the total volume is accurately calculated by putting it in a container with water and measuring how much water is displaced. This method makes it possible to compare droppers and 3D-printed models easily and is the most accurate of the methods. This results in a characteristic diameter (D_{char}) of 0.12 meters.

The multiple mussel length approach was found to be too sensitive since there were only seven mussel types, and the average diameter approach was difficult to compare a real dropper to a 3D model, making it complicated to apply the results to a numerical model of a real long line system. The spatial organization model was used for mono-layered dropper lines, and since this research used a bi-layered dropper line this method was excluded.

4.4.5. Length of the model

The length of the model was selected based on the available force transducers and the width of the wave tank, which was 2.75 meters. The force per meter was calculated for a cylinder with a characteristic

diameter of 0.12 meters, which resulted in a maximum hydrodynamic force per meter of 140 N/m based on the Morison force equation and the drag and inertia coefficients of a cylinder. The force due to the acceleration of the system was not taken into account due to the unknown mass. The force transducers available had capacities of 5, 8, 15, or 20 kg, and two force transducers were required to attach the model on both sides. After considering various options, a 0.5-meter length for the model with two 8 kg force transducers was chosen to limit the wall effects and to ensure a maximum hydrodynamic force of 70 N. The force exerted by the model due to Newton's second law of motion was estimated to be 13.3 N. With two force transducers having a maximum of 160 N, the maximum force measured would be 83.3 N, which gives a safety factor of two.

4.5. Steady current test parameters

In the drag test, the model is towed in the towing tank. In this experiment, the Reynolds numbers of the current at the site have to be imitated. The Re values that presented the steady current at the site are shown in section 3.2, but these have to be scaled to lab parameters. This is done by filling in equation 2.3 for the Reynolds numbers at the site. To acquire the right velocities for the carriage these Reynolds numbers have to be scaled from seawater to freshwater. The model is a 1 to 1 scale so the diameter does not have to be scaled. That results in the following equation.

$$u_{carriage} = u_{current} * \frac{v_{fresh}}{v_{sea}} \tag{4.2}$$

The test parameters were based on the different boundaries of the Re in steady current and three tests in between the boundaries to see if the drag coefficient changes over the Re regime. The parameters for the towing experiment, calculated in equation 4.2, are shown in table 4.2.

Table 4.2: The different towing speeds with corresponding Re values

v (m/s)	0.25	0.4	0.55	0.7	0.85
Re (-)	$3 * 10^4$	$4.6 * 10^4$	$6.3 * 10^4$	$8.0 * 10^4$	$1.0 * 10^5$

More data will minimize errors in the results, therefore the test time is of importance to the quality of the tests. The test time is found by calculating the maximum acceleration and deceleration by equation 4.3, the drag force is neglected because it is very small compared to the force of the towing carriage. Here C_f is the estimated friction coefficient, and m is the mass of the carriage estimated at 4000 kg.

$$a_d = a_a = \frac{m * g * c_f}{m} = 1.0 m/s^2 \tag{4.3}$$

The minimum time for an experiment is calculated in equation 4.4. Where the maximum driving length of the small wave tank is 60 meters and is denoted as L_{tank}, the minimum test time is $t_{test,min}$, and the maximum speed is u_{max} (0.85 m/s).

$$t_{test,min} = \frac{L_{tank}}{u_{max}} - \frac{u_{max}}{a_a} - \frac{u_{max}}{a_d} \tag{4.4}$$

This equation is derived from the time that it takes before the carriage reaches the end at a constant speed, shown in equation 4.5, minus both the time it takes for the acceleration and deceleration of the carriage, shown in equation **??**.

$$t = \frac{L_{tank}}{u_{max}} \tag{4.5}$$

$$u_{max} = u_{begin} + at \tag{4.6}$$

since the carriage starts at rest u_{begin} is zero. So, equation 4.5 can be written as shown in equation **??**.

$$t = \frac{u_{max}}{a} \tag{4.7}$$

Which results in a minimum test time of approximately 65 seconds.

4.6. Oscillatory flow test parameters

To determine the appropriate KC and Re values for the experiment, it is necessary to first determine the correct parameters. The wave amplitude is one such parameter that needs to be considered, as the wave tank has a maximum capacity for the wave height, beyond which the tank would overflow. With a water depth of 1.25 meters, the maximum wave height is limited to 25 centimeters. This is insufficient for the range of KC values under consideration. Therefore, in order to achieve the necessary wave amplitudes, the waves are simulated by oscillating the model. By oscillating the model, it is possible to achieve larger amplitudes of motion, which are needed to test the range of KC values under consideration.

4.6.1. Forced oscillation test parameters

To acquire higher KC numbers forced oscillations experiments were conducted. The setup oscillates in the x-direction on the guiding rails pushed and pulled by the linear motor. The linear motor that is used is a P01-48x360F by LinMot and the slider is 2000 mm with a diameter of 28 mm. A position meter was attached on the opposite side of the linear motor on the guiding rails to measure the oscillations.

For the oscillatory experiment, the desired parameters are a KC of 10 to 25 and a Re of $0.15 * 10^5$ to $1.5 * 10^5$. The boundaries of the total KC and Re domain are known, but the steps between the boundaries have to be determined. As can be seen from the research of Sarpkaya in 1976 for a cylinder the drag and inertia coefficient change substantially in the KC domain of 10 to 25. This can be seen in figure 4.9, where the circles represent the drag coefficient, the asterisks represent the inertia coefficient, and K represents the Keulegan-Carpenter number.

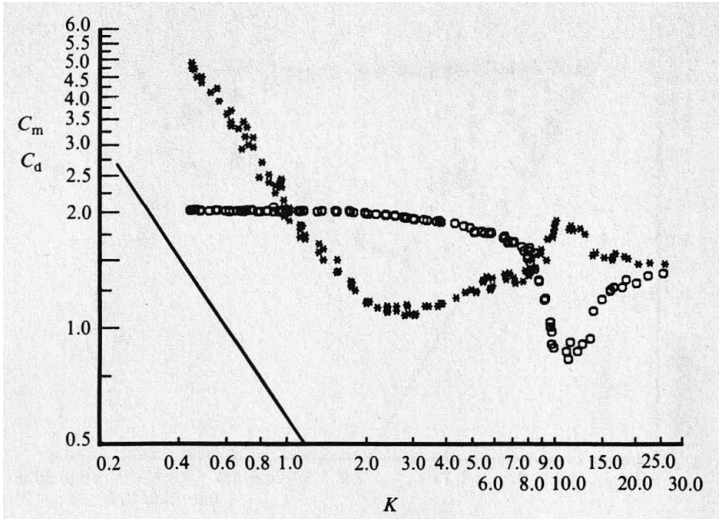

Figure 4.9: drag and inertia coefficient of a cylinder over KC (Sarpkaya 1976)

Figure 4.9 displays the drag coefficient and inertia coefficient as functions of the KC number, where the stars represent the drag coefficient and the circles represent the inertia coefficient. It is observed that these coefficients exhibit significant variation over the range of KC values from 10 to 25. In order to ensure that the experimental data captures the shape of the model cylinder while also limiting the total duration of the experiment, it was decided to use an interval of 2.5 for the KC number. To determine the appropriate range of Reynolds numbers for each KC value, figure 3.3 was used as a reference, and the boundaries of each KC range were chosen along with three additional points to ensure a sufficient number of data points per KC value.

Equations 4.10 and 4.9 were used to determine the appropriate parameters for the oscillation experiments. To obtain these parameters, the KC and Re values needed to be translated to linear oscillations. The amplitude of the oscillations was based on the KC range, while the frequency was based on the Re range. The amplitude was determined using equation 4.9, which combines equation 4.8 and equation 2.9.

$$U_{max} = A * \frac{2\pi}{T} \tag{4.8}$$

$$A = \frac{D * KC}{2/\pi} \tag{4.9}$$

The period is obtained by combining equation 2.3 and equation 4.8 into equation 4.10 using the amplitude obtained earlier.

$$T = \frac{A * 2\pi * D}{v * Re} \tag{4.10}$$

In table 4.3 the KC and Re numbers are shown that are tested during the forced oscillations experiment.

Table 4.3: KC and Re values of the oscillation experiments

KC (-)	Re(-) $*10^4$				
9	2.4	3.0	3.6	4.1	4.8
12	2.4	3.0	3.6	4.2	4.8
15	3.6	4.8	6.0	7.2	
18	4.8	6.0	7.2	8.3	9.6
21	4.8	6.0	7.2	8.4	9.6
24	5.9	7.2	8.3	9.7	10.8
27	7.2	8.4	9.6	10.8	12.0

Using equation 4.9 and 4.10 and table 4.3 the parameters for the forced oscillations tests are computed and shown in table 4.4.

Table 4.4: Parameters of the oscillation experiments

A(m)	T(s)				
0.18	2.70	3.13	3.57	4.30	5.35
0.24	3.57	4.12	4.76	5.75	7.14
0.3	2.98	3.57	4.55	5.88	
0.36	2.70	3.13	3.57	4.35	5.36
0.42	3.13	3.57	4.17	5.00	6.25
0.48	3.23	3.57	4.17	4.76	5.88
0.54	3.23	3.59	4.03	4.62	5.36

The minimum test time required for forced oscillation experiments depends on the oscillations of the model, as well as the time it takes for the resulting waves to reflect off the wave maker or beach and travel back to the model. This distance, which the wave must traverse, is approximately 80 meters. The speed at which the waves travel can be calculated using equation 4.11, where L is the wavelength, k is the wave number, g is the gravitational acceleration, and d is the depth.

$$c_g = \frac{(\frac{g}{k} tanh(kd))^{0.5}}{2}(1 + \frac{4\pi d/L}{sinh(4\pi d/L)}) \tag{4.11}$$

Based on the calculations, the testing time for the wave experiments is expected to range from 42 to 105 seconds, depending on the period of the wave being tested. During each test, a total of 20 waves were produced, with 6 of these waves being used to gradually increase and decrease the wave amplitude. This resulted in a total of 14 waves with their full amplitude being used for the actual test.

4.6.2. Wave experiment test parameters

The wave maker and wave tank have limitations on the maximum values of the KC and Re numbers that can be achieved, as illustrated in figure 4.2. The region beneath the red stars in the figure represents the KC and Re values that are achievable in practice. To further illustrate this, five different waves are identified that close the boundaries of this region. In order to conduct wave experiments, it is necessary

to carefully control the values of KC and Re. To this end, figure 4.10 provides a closer look at the KC and Re values of the waves used in the experiment, which are represented as light blue dots. To reduce the time required for tuning the waves, it was decided to maintain the period of the waves at a constant value twice for T =5.24 s and 3.69 s.

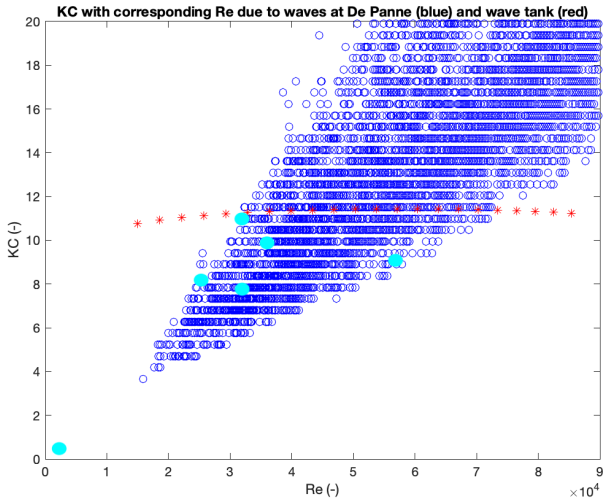

Figure 4.10: Indication of the different waves as light blue dots

In this research regular waves created using a hydraulic wave maker in the towing tank are investigated. The waves were tuned beforehand in order to acquire the right wave height and period. The values that are tested are chosen to achieve the goal of the research while being within the limits of the test facility. The smallest wave (T=1.19 s, A=0.03 m) was added in order to have a deep-water wave as a reference point. The other waves are all intermediate-depth waves.

Table 4.5: KC and Re numbers from figure 4.10

Re (-) $*10^4$	0.5	5.7	3.5	2.8	2.9	2.1
KC (-)	0.4	8.4	9.5	7.5	8.3	10.5

To determine the correct wave parameters figure 4.2 is used. These last five waves are shallow depth waves, which do not result in a sinusoidal measured wave height. Therefore one deep water wave is added with the same wave steepness as the wave with the lowest period. In Table 4.6 the parameters of the waves are shown, where A is the wave amplitude, λ is the wavelength, and T is the wave period.

Table 4.6: Parameters of the waves experiments

T (s)	1.19	2.73	3.69	3.69	5.24	5.24
A (m)	0.03	0.12	0.10	0.080	0.090	0.070
λ (m)	2.21	8.48	12.1	12.1	17.8	17.8

In wave experiments, the minimum test time is determined by the time required for the waves to reflect on the beach and travel back to the model. This time is calculated using equation 4.11. The testing time prior to the reflected wave reaching the model has a minimum of 15 times the wave period. Therefore the build-up of every test run is the same as for the forced oscillations.

In preparation for the experiments, it was necessary to tune the waves to ensure they had the correct amplitudes. This involved adjusting the voltages used to control the wave maker to obtain the desired wave height while keeping the wave period constant and equal to the signal period. Specifically, the voltage used to determine the amplitude of the wave was modified for each wave period, and the measured wave height was checked to ensure that it was consistent with the desired amplitude. Once the waves were properly tuned, the experiments could be conducted using the tuned wave signals.

4.7. Design of experimental setup

The setup consists of multiple parts, for example, the model, end plates, and guide rails. In this section, the design of the setup is explained along with the different parts. The whole setup is shown in figure 4.11.

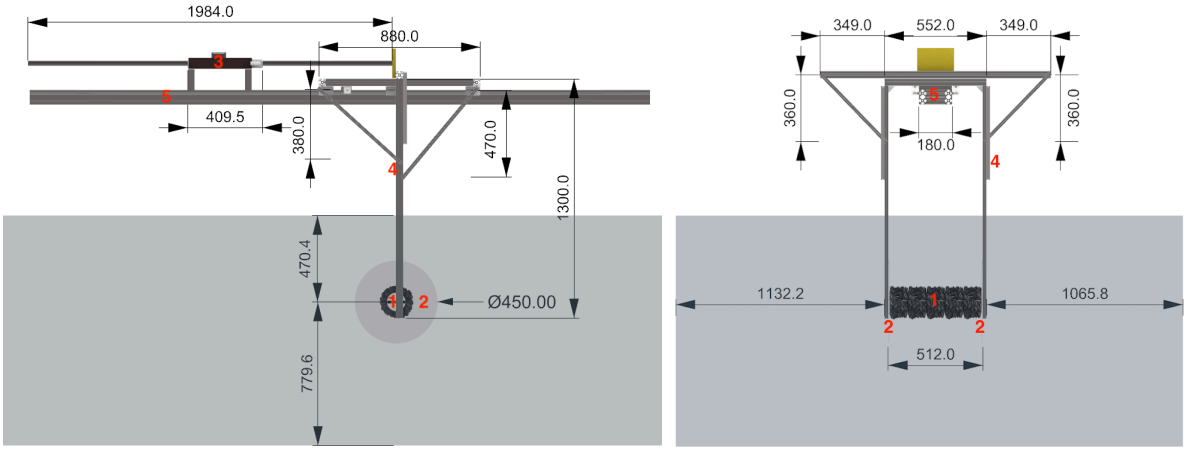

(a) Side view of the whole setup in Rhino

(b) front view of the whole setup in Rhino

Figure 4.11: Overview of the setup in Rhino in mm 1. Model 2. End plates 3. Linear motor 4. Carriage 5. Guide rails

4.7.1. Model attachment

The model is attached to the installation by four 3D-printed blocks. Two on each side with the force transducer in between them to isolate the forces on the model and the forces on the installation. These blocks are printed using PETG plastic, which is water-resistant. The bolts used to attach the blocks and the force transducers are made from aluminum to make sure the force transducers will not erode. The dimension and different parts are shown in figure 4.12.

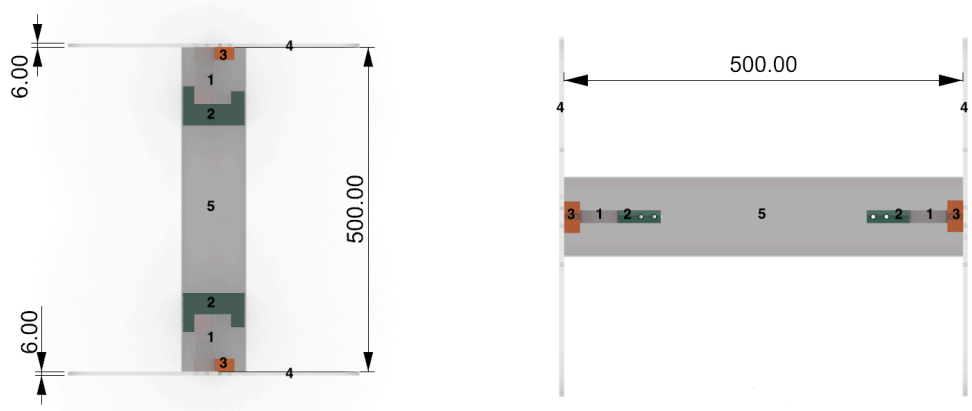

(a) Model attachment top view

(b) Model attachment front view

Figure 4.12: Model attachment views in mm where 1. Force transducers 2. Blocks to attach PVC tube to force transducer 3. Block to attach force transducers to end plates 4. End plates 5. PVC tube

4.7.2. End plates

The inertia and drag coefficients are coefficients based on the flow across the model. To accurately determine these coefficients, it is important to take the flow that passes the model on the sides, instead of going over the model, into account as well. One common method for blocking this flow around a model is to use end plates. The diameter of the end plates should be at least two to three times the diameter of the model in order to ensure that there is no flow around the model (Fu, Y. Xu, and Chen 2014). In this case, the end plates have been determined to be three times the diameter of the model, which ensures that there is definitely no flow around the model. The end plates are made of perspex

and are 6 mm thick. The sides are sanded so the shape is oblique and the flow is minimally affected. The end plates with their dimensions are shown in figure 4.13.

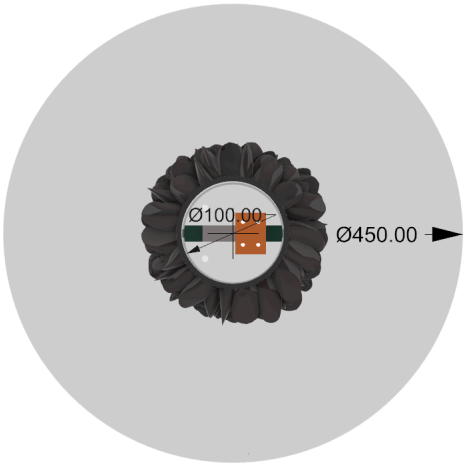

Figure 4.13: Sideview of the endplates and the model attachment in mm

4.7.3. Guide rails with model carriage

The linear motor will use its magnetic field to make the rod inside go back and forth. This oscillation will resemble the movement of waves on the model. To make sure that this movement is purely axial, guide rails are used so the model will oscillate smoothly in the appropriate direction. Due to the forces acting on the model, a moment is created. To cancel this moment out the carriage has four rollers attached to the guide rails with an arm 0.42 m from the center of rotation. Also, two arms are attached sideways to create stiffness in these directions as well. The guide rails and carriage are shown in figure 4.14.

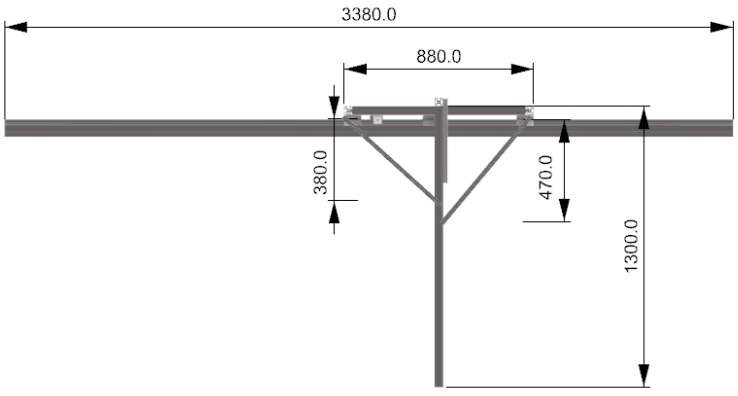

(a) Side view of the whole setup in Rhino

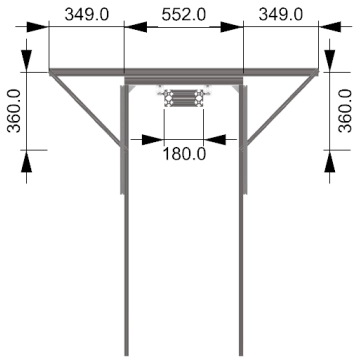

(b) front view of the whole setup in Rhino

Figure 4.14: Sideview of the guide rails and carriage in mm

4.7.4. Linear motor

The linear motor is placed on top of the guide rails. The linear motor uses magnetic fields that push the slider inside to the desired position. This stator is attached to the carriage by a wooden board exactly in the middle of the carriage. Due to the symmetry of the system and the alignment of the linear motor, there is no torsion in the system.

4.7.5. Vortex-Induced Vibrations

Vortex-induced vibrations (VIV) are a type of fluid-structure interaction where fluid flow around a bluff body (like a cylinder or pipe) creates vortexes in its wake. These vortexes are formed due to the flow

that detaches from the structure's surfaces. The cylinder can experience vibrations due to this vortex shedding, which can become motions due to constant excitation.

Since the model is placed in between the arms of the guide rails carriage there are no rotational effects. The relevance of vortex-induced vibration is assessed using the dimensionless Strouhal number. The Strouhal number at which vortex-induced resonance occurs is dependent on the Reynolds number. For the assessed current, with a velocity of 0.25 to 0.85 m/s the Strouhal number is 0.25 (Z. Xu, Qin, and Li 2020). The equation for the vortex shedding frequency is given in equation 4.12 where u is the current velocity and D is the diameter of the model.

$$f = \frac{St * u}{D} \tag{4.12}$$

This results in a maximum vortex shedding frequency of 1.8 Hz. The natural frequency of the system is elaborated on in chapter 5 and given in table , ranging from 5 to 42 Hz. Since the maximum vortex shedding frequency and the minimum natural frequency are not in each other's range there will be no lock-in (Kallinderis, Schulz, and Jester 2001).

4.7.6. Free surface and bottom effects

Free surface effects refer to the behavior close to a boundary, such as the surface of a body of water or the interface between two fluids with differing densities. Free surface effects can lead to disturbances on the surface of the fluid and these disturbances can increase the drag coefficient by creating additional turbulence or by inducing pressure changes that act to slow down the motion of the body. Also, these influences may significantly affect a body's motion and, consequently, the inertia coefficient. This is because the fluid in contact with the free surface tends to resist changes in motion, leading to a larger effective mass for the body (Batchelor 2000).

The influence of this effect will vary depending on a number of variables, such as the fluid's characteristics, the body's size, shape, and motion. For instance, a body moving quickly through a fluid with high viscosity may see a bigger rise in drag coefficient as a result of free surface effects than a body moving more slowly through a fluid with a lower viscosity (Batchelor 2000).

The distance between the center of the model and the bottom of the wave tank is 780 mm, and between the center of the model and the free surface is 470 mm. The best way to determine the influence of bottom and free surface effects is to make an analysis using Computational Fluid Dynamics (CFD).

4.8. Experimental setup

The setup was made using 40 x 40, and 40 x 20 aluminum ITEM beams. Six different 20 x 20 aluminum ITEM cross beams were attached to make the beams holding the model stiff. The two load cells inside the model are of the type L6J-C3D-8kg-0.45B by Zemic. These load cells were made waterproof. The model is 3D printed using PETG, which is waterproof. The cylinder, to which the model is attached and containing the load cells, is a PVC tube with an outer diameter of 100mm and thickness of 2mm. In the setup, the drag force and the inertia force are the quantities of interest. These are both in the x-direction, which is alongside the wave tank, and negative in the direction of the waves and current. Therefore the load cells are placed in the x-direction, and in between the end plates and the model to isolate the forces from the rest of the setup. In figure 4.15 the setup is shown.

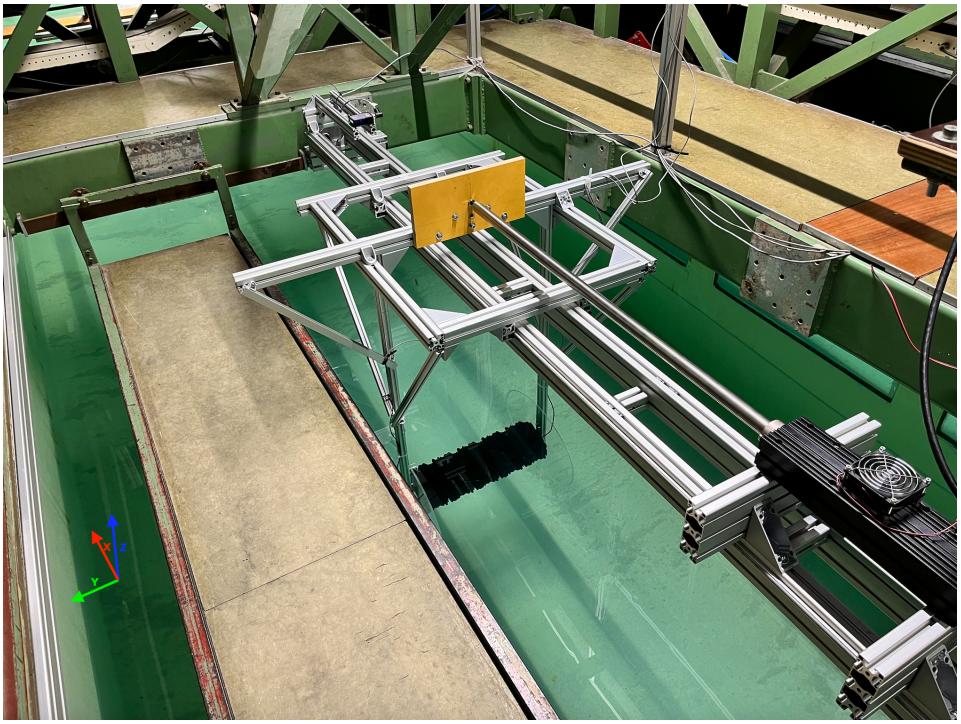

Figure 4.15: Overview of the setup

4.8.1. Sensor placement

The sensors are placed in different positions. The position sensor is placed on top of the guide rails and uses the yellow attachment board of the linear motor, which is also shown in figure 4.15, as the reference point. The wave probes are indicated as blue dots and the position sensor as a pink dot in figure 4.16. The force transducers are located on both sides of the model as shown in figure 4.12a.

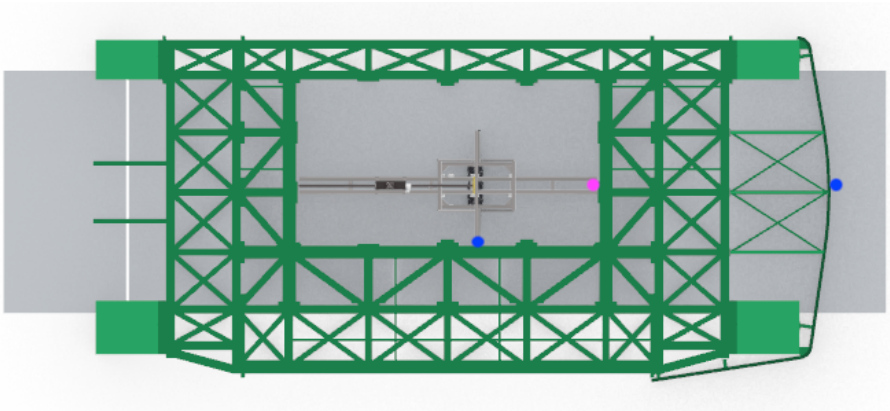

Figure 4.16: Placement of sensors

4.8.2. Data acquisition

The wave height is measured by two acoustic wave probes with a delay of 730 ms connected to the UltraLab ULS Advanced, which has a voltage signal from 0 to 10 V as output. The force transducers are Zemic L6J-C3D-8kg-0.45B and are calibrated and connected to a PICAS amplifier, which has a voltage from -10 to 10 V as output. The calibration is shown in appendix D. They have an accuracy of 0.1 and 0.3 % on a range of 80 N. The position is measured by a laser position sensor called the Baumer OM70-L1500.HH1500.VI, which has an output of 0 to 10 V as well. The signals were filtered by an analog low-pass filter with a cutoff frequency of 100 Hz. Filtered signals were recorded on a PC with National Instruments PCI-6033E. A/D converter card with a sampling rate of 1,000 Hz and 16-bit

resolution.

4.9. Experiment conduction

The testing procedure followed a specific plan for each test run, which included a cool-down time to allow the water turbulence to settle. The duration of this cool-down time depended on the type of experiment and the parameters of the test run, as the energy put into the water could vary. Prior to each test run, a zero run was performed to check for any turbulence or irregularities.

During the towing test, the cool-down time was initially set to 30 minutes. However, it was later determined that for the lowest two velocities, the cool-down time could be reduced to 20 minutes, while for higher velocities, the 30-minute cool-down time was necessary.

For the forced oscillation test, the cool-down time was also set to 30 minutes. However, for the lowest three amplitudes for all periods and the higher amplitude with a period longer than 5 seconds, the cool-down time could be reduced to 20 minutes. As waves tend to dampen out over time, the frequencies of the oscillations were altered to avoid amplifying the wave in the water.

In wave tests, the waiting time was determined during the tuning of the waves. It was found that a 30-minute cool-down time was sufficient for reliable results, and no exceptions were observed. The wave frequencies were also adjusted to avoid amplification of the waves in the water.

On top of the tasks per experiment, there were also tasks to do on a daily basis. The temperature of the water was measured daily and was around 17 $^{\circ}$C. A hook was attached to the wave tank exactly at the water level to check every day if it still was at the same level, and the tank was filled if needed.

5

Data processing

After conducting the experiments a lot of raw data is obtained. The raw data is processed into usable data to come up with the results. The data processing is subdivided into different experiment types because for every experiment the data sets differed a lot. The tools and methods used for the data processing are elaborated on in this section.

5.1. Data processing towing

The first step of data processing involves conducting a thorough examination of the data to confirm that the signal accurately represents the relevant physics. This examination includes evaluating if the force increases as the system accelerates and if the force changes direction in correspondence with changes in the direction of velocity. This raw data used is shown and confirmed in figure 5.1.

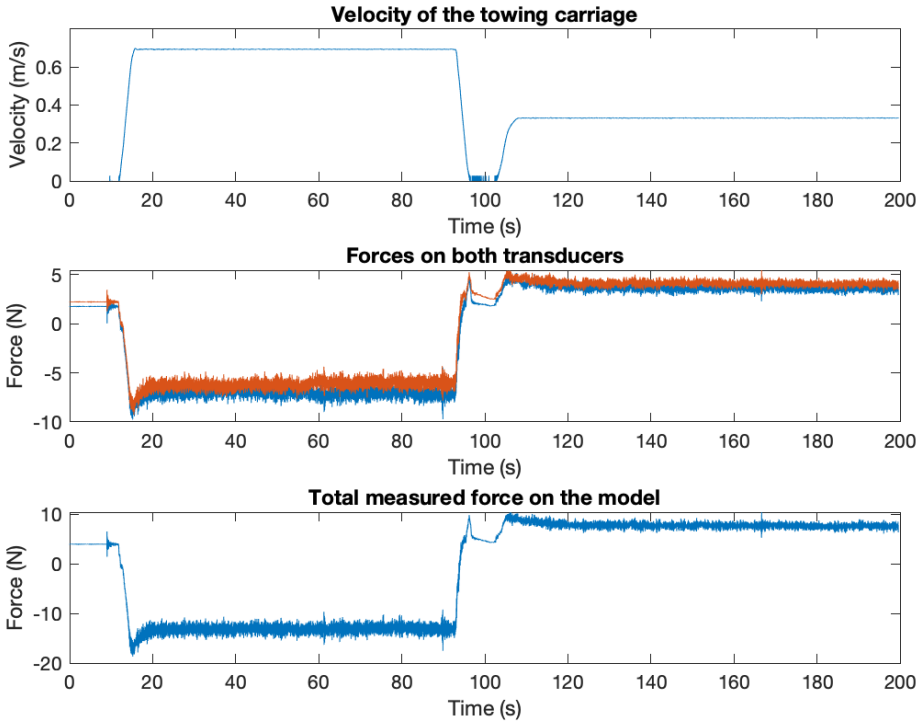

Figure 5.1: Raw data of the velocity and force

Figure 5.1 includes three figures that provide information about the test run. The top figure displays

the velocity over time and shows that the test began from rest, and after 15 seconds the towing carriage accelerated for a few seconds before maintaining a constant velocity of 0.7 m/s for 80 seconds. The carriage then decelerated to rest. It remains at rest for a couple of seconds and then accelerates to a speed of 0.25 m/s to return to its starting position. Notably, the velocity was measured based on frequency, and not direction, resulting in a velocity signal that is always positive, even when moving back to the starting position in the negative x-direction.

The second figure displays the force signal over both transducers. As previously mentioned, the force on the transducers is induced by the towing carriage's velocity, making it necessary to consider the velocity signal when confirming the force signal. The force signals have an offset of around two N while at rest. When the towing carriage accelerates in the positive x-direction between 13 and 17 seconds, the forces decrease to -8 and -7 N. The velocity and force should be in opposite directions, which is the case here. After the acceleration phase, the force remains constant over the time that the velocity stays constant. During the deceleration phase, the forces return to their offset with a slight overshoot due to the induced current from the towing carriage overtaking it. The force then stabilizes at its offset. During the towing carriage's acceleration back to the starting position, the force increases which shows that the velocity signal does not measure direction.

The third plot adds up the force of both transducers over time. The plot follows the same trajectory as the second plot, but the values are doubled due to the addition of the two signals.

In summary, the three plots in the presented figure provide valuable insights into the test. The figure shows the velocity which induces the forces and shows when the force should increase, decrease or remain constant. The force signals provide information about the transducers' behavior during the test. By adding up the force signals from both transducers, the third figure shows the combined force of both transducers.

5.1.1. Power spectral density

Different factors can influence the signal during the measurement. For example, the natural frequencies of the system can be measured by the transducers because the towing carriage is a stiff moving construction. There can also be remaining movement in the water. To see what frequencies the measurement contains, a power spectral density (PSD) is computed. A PSD is a mathematical function computed using a Fourier transform and used to describe the distribution of power of a signal over its frequency components. PSD is typically represented as a graph, with frequency on the x-axis and power on the y-axis. A high PSD value at a particular frequency indicates that the signal has significant power at that frequency. Conversely, a low PSD value at a particular frequency indicates that the signal has less power at that frequency. For the test of figure 5.1 a PSD was computed and that PSD is shown in figure 5.2.

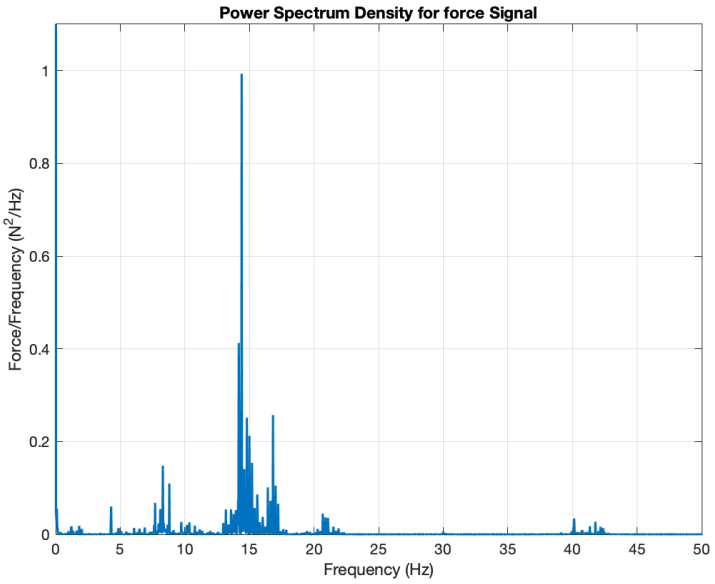

Figure 5.2: the power spectral density of a towing experiment test run

Figure 5.2 displays multiple peaks in the PSD graph over the time interval indicated by the red box in figure 5.3. There is a peak at 0 Hz while the mean of the signal is not zero. Several small peaks are present around 5, 7, 21, and 41 Hz, and larger peaks appear around 8, 14, and 17 Hz. The primary frequencies of interest are the natural frequencies of the system. To identify these natural frequencies, three different tests were conducted, each triggering a natural frequency by tapping the system in a specific direction (x, y, or z). The measurements were taken during each test, and a PSD was computed for each test. These PSDs are shown in appendix C, and the identified peaks represent the natural frequencies of the system. Table 5.1 displays the natural frequencies for each direction.

Table 5.1: The natural frequencies in x,y and z-direction

Direction	Natural Frequency								
x	5	7	8	14	28	31			
y	5	7	8	14	17	21	33	37	42
z	5	7	8	14	28				

The PSD of the test run shows peaks at frequencies of 5, 7, 8, 14, 17, 21, and 41 Hz. When this information is combined with the natural frequencies identified in Table 5.1, it becomes apparent that the noise in the power of frequencies in the signal is entirely caused by the natural frequencies of the system. As these force measurements are not relevant for calculating the drag coefficient in a steady current, a filter must be applied to remove these frequencies from the signal.

5.1.2. Filtering

In this study, the decision was made to use a low-pass filter. The selection of a low pass filter with a low cut-off frequency was deemed to be more appropriate than using a high pass filter with a high cut-off frequency because the frequencies of the analyzed forced oscillations and waves were lower compared to the natural frequencies. Therefore, the theory of low-pass filters was explored and deemed to be the most suitable approach for this research.

The Butterworth low-pass filter was selected for this research. The theory and differences between various low-pass filters are discussed in detail in appendix C. The oscillation frequencies and natural frequencies in this research were quite close. The low-pass Butterworth filter has a flat frequency response and therefore this was found most suitable filter for this research.

Prior to every run, a zero-test run is done. To calculate the offset of the force transducer the average force of the test run is taken as the offset. This offset is subtracted from the force signal. Afterwards,

this signal is filtered by the low-pass Butterworth filter with a cut-off frequency of four Hertz, which is the lowest natural frequency, to filter out the noise that is on the force signal. Figure 5.3 shows the difference between the total force measured force and the filtered force both without the offset.

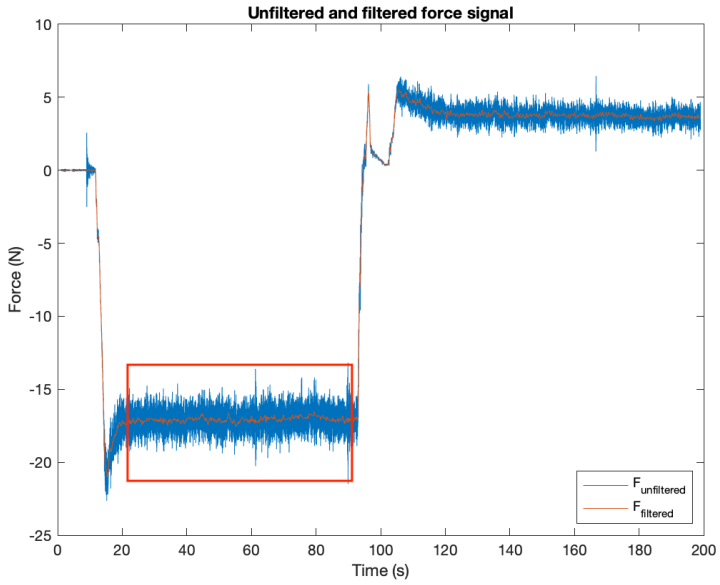

Figure 5.3: Comparison of the raw and filtered data both without the offset

As shown in figure 5.3, it can be observed that the filtered force follows a similar trajectory as the unfiltered force. However, it is particularly noticeable, especially during the interval where the force is constant, that the noise is eliminated through filtering. The line still exhibits minor oscillations. The red box in the figure highlights the interval where the force is constant, and the filtered force during this interval is used to compute the drag coefficient. For the velocity signal, a PSD is computed as well, but there are no peaks for the power of the frequency in the signal. Therefore, the signal does not have to be filtered. Over this interval, the mean velocity, force, and standard deviation of both are calculated.

5.1.3. Drag coefficient

Equation 5.1 is used to calculate the drag coefficient per sample rate for the time interval shown as the red box in figure 5.3, where F is the force in N, and U is the velocity of the towing carriage in m/s, D is the characteristic diameter of 0.12 m, and rho is the density of fresh water at 17 °C, which is 997 kg/m^3. The results are presented in chapter 6 as a mean drag coefficient and its standard deviation.

$$C_d = \frac{F}{0.5\rho U^2 D} \tag{5.1}$$

5.2. Forced oscillation data processing

To validate if the signal accurately represents the expected physics, the initial step is to examine the raw data of the position and force signals to determine if there is a connection between the motion and the forces. Another criterion is to plot the theoretical function of the Morison equation on the data to see if they match. Additionally, straightforward checks, such as ensuring that the amplitude and period are correct, are also essential. Different plots of the raw data can be seen in figure 5.4.

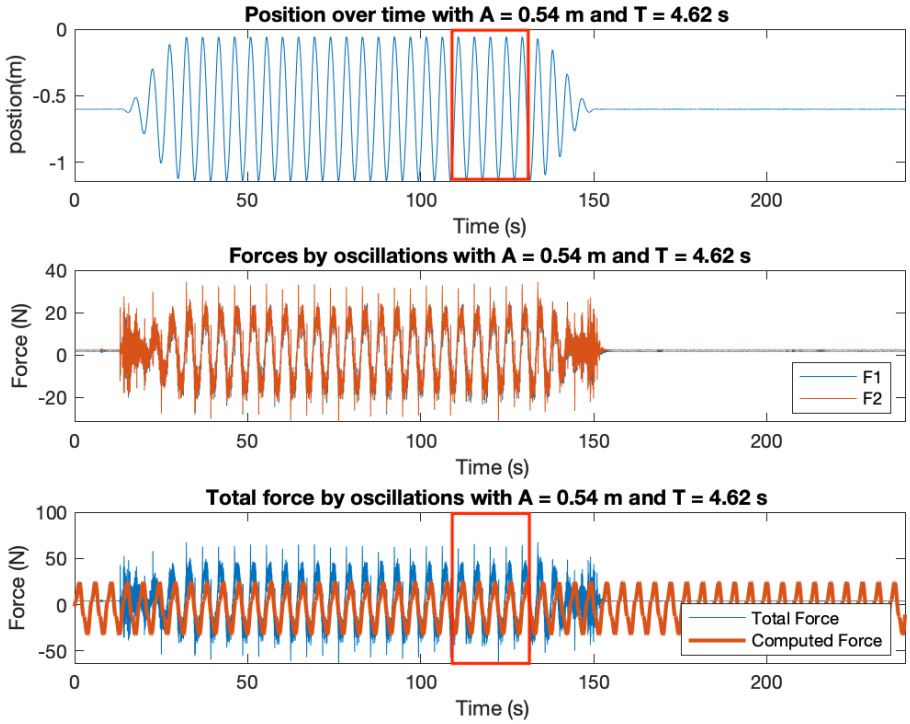

Figure 5.4: First check of the oscillation experiments

As shown in figure 5.4, the upper plot represents the position signal. As described in subsection 4.6.1, the oscillation input signal is composed of 20 oscillations, where the first three oscillations gradually increase, and the last three oscillations gradually decrease, as seen in the measured position signal. The period of all the oscillations in the test run is identical. The period of the measured position signal was verified to be the same as the input period. The measurements start at rest, and then the three build-up oscillations begin. After that, the 14 oscillations with full amplitude begin, which in this test run was 0.54 m, and the model reaches that amplitude. Subsequently, the amplitudes gradually decrease with three oscillations, and the model returns to its starting position at rest.

In the middle plot, both the forces measured by the force transducers are shown. It starts at rest with an offset and then becomes very noisy due to the start of the oscillations when the model carriage is moving. This noisy signal disappears after the three build-up oscillations, and the full force amplitude is reached, causing the forces to move back and forth in the same way with two different peaks every half a period. Both forces follow each other and tend to behave in the same manner. After the full amplitude oscillations, the amplitudes gradually decrease over three oscillations, and when coming to rest, the shivering starts again. When the oscillations are over, and the model is at rest and at its starting position, the force signals return to their offset again.

In the last plot, the total force is plotted together with the computed Morison force to compare the trajectory of both. The Morison force is computed using equation 4.8 times the cosine of the signal for the velocity and its derivative for the acceleration. The total force follows the same trajectory as described for the middle plot, but all values are doubled. The computed force is the Morison force, where the drag and inertia of a cylinder are used. The shape looks the same, and the period is the same as well, but due to the offset, it is a bit shifted, and the plots are not on top of each other. The red rectangles are the last five oscillations of the test run, and that is the data used to determine the drag and inertia coefficient. The last oscillations are chosen while the Morison force is based on a steady-state situation, and the last oscillations are the closest to this situation.

5.2.1. PSD

After confirming the raw data is valid, the signal has to be checked for noise. To check all the power of the frequencies that are in the total force signal a PSD is computed. An example of a PSD of an oscillation experiment is shown in figure 5.5. The boundaries of the oscillation experiments, so lowest and highest amplitude and frequency, and the middle amplitude and frequency, their PSDs are put in appendix C to show the power of the frequencies in the system during oscillations.

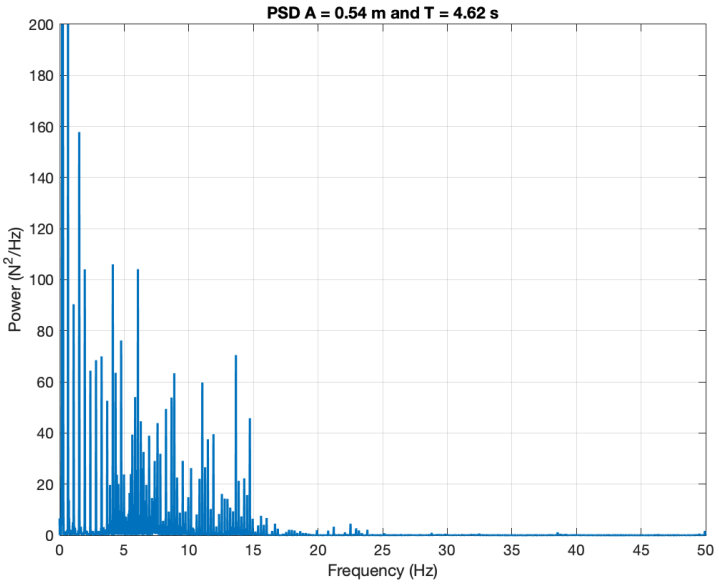

Figure 5.5: PSD for the oscillation experiment with A = 0.54 m and T =4.62 s

The PSD plot in figure 5.5 shows several peaks between 4 and 15 Hz and some peaks before 4 Hz with a regular interval. These peaks are in the nth order of the oscillations frequency. Where n is 1,3,5,7 and so on. These orders are substantiated by figure 5.6 and table 5.2.

Table 5.2: Nth order of the oscillation frequency and the frequency peaks of the PSD

Nth order	1	3	5	7	9	11	13
Frequency of order (Hz)	0.22	0.65	1.08	1.52	1.95	2.38	2.81
Frequency of peak (Hz)	0.22	0.65	1.08	1.52	1.95	2.38	2.81

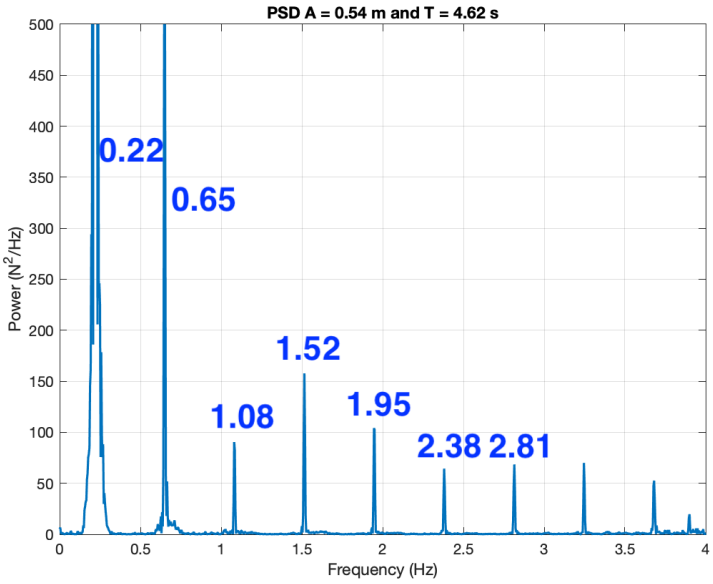

Figure 5.6: PSD for the oscillation experiment with A = 0.54 m and T =4.62 s for 0 to 4 Hz

However, there are also many irregular peaks after 4 Hz. Since the Morison force is the goal to get out of the experiment the cut-off frequency should be set before 4 Hz to eliminate this noise of the linear motor and the natural frequencies. However, the cut-off frequency should not be set too low, while the peaks before 4 Hz are not considered noise since they are at the first, third, fifth, and seventh order of the oscillation frequency. This is a characteristic of the Morison equation as it may remove important data from the signal for the Morison force calculation. Therefore, a careful selection of the cut-off frequency is required to obtain accurate results from the Morison equation. Figure 5.7 shows the influence of the cut-off frequency that is a multiple of the frequency of a typical theoretical Morison force induced by a wave with an amplitude of 54 cm and a period of 4.62 s.

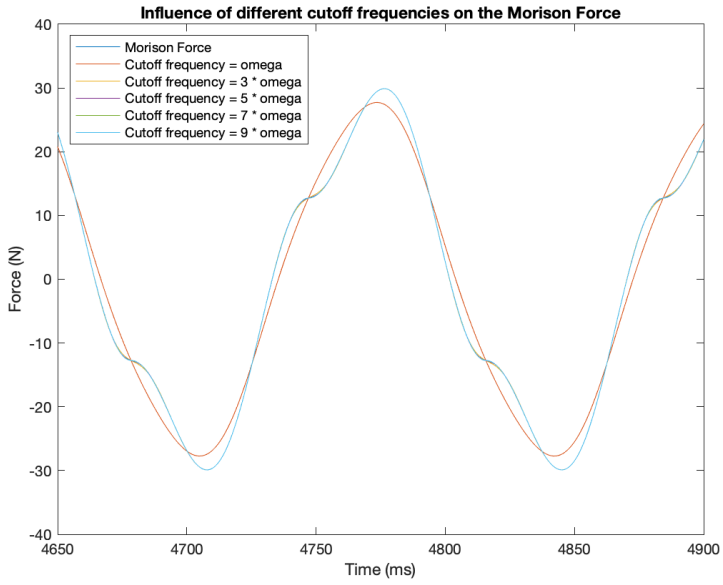

Figure 5.7: Global representation of the Morison equation with different cut-off frequencies

The impact of different cut-off frequencies on the Morison force appears to be negligible on an oscillation scale, except for the cut-off frequency at the oscillation frequency, which is a first-order sinusoid.

Therefore, the choice of the cut-off frequency has a minor effect on the Morison force on an oscillation scale.

To investigate the behavior of the Morison force in more detail, a zoomed-in view of the 'Morison hump' in figure 5.7 is presented in figure 5.8. This will enable a more in-depth analysis of the impact of different cut-off frequencies on the Morison force.

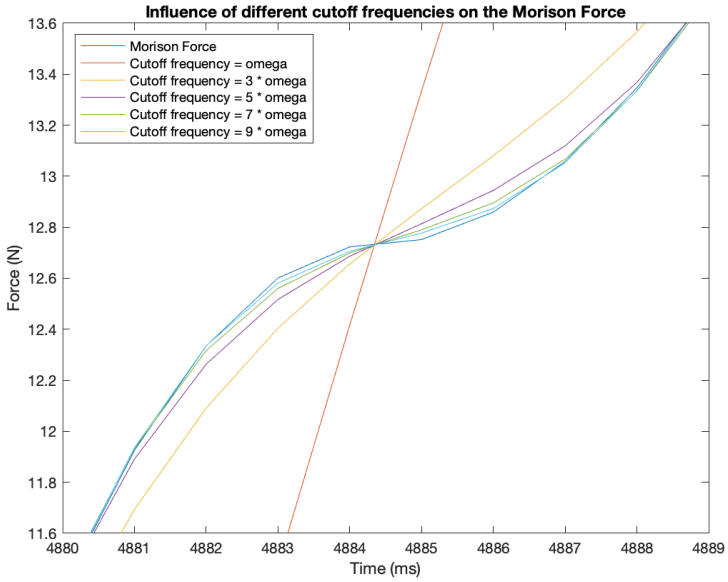

Figure 5.8: zoomed in Morison equation with different cut-off frequencies

The results in figure 5.8 clearly show that as the order of the frequency increases, the difference between the Morison force and the computed force decreases. The maximum amplitude of these plots is 30 N, and for a cut-off frequency of nine times the frequency, the maximum difference compared to the Morison plot is 0.02 N, which is less than 0.1% of the maximum force. Therefore, for each test run, the cut-off frequency is set to nine times the frequency. The maximum frequency in all the test runs is 0.37 Hz, which when multiplied by nine results in 3.33 Hz. This value is lower than the first natural frequency of 4 Hz, making it a reasonable factor for the cut-off frequency. To be consistent all the signals are cut off at 3.33 Hz.

5.2.2. Velocity and acceleration signal

It is a challenging task to obtain an acceleration signal from a position signal. The differentiation process of the position signal twice is required to obtain the acceleration signal. However, the high frequency of the resulting data points of the position signal may lead to difficulty in accurately resolving small changes in position. To overcome this issue, a technique of reducing the sampling rate and taking the average of the corresponding values is utilized. This method increases the distance between data points, thus enabling more precise resolution of position changes. The moving average of the signal is taken to reduce the data points. Further elaboration on the theory behind the differentiation process and the chosen method is provided in appendix C.

In order to accurately model the Morison force using drag and inertia coefficients as variables on the filtered total force, it is necessary to incorporate the velocity and acceleration of the model. In an ideal experimental scenario, the velocity and acceleration would exhibit behavior similar to that of deep ocean waves, which are characterized by first-order sinusoidal patterns. However, in reality, this is not always the case. Therefore, in order to incorporate the velocity and acceleration of the model into the Morison equation as a formula, they must be fitted. The position, velocity and acceleration of the model can be observed in figure 5.9. The theory behind fitting can be found in appendix C.

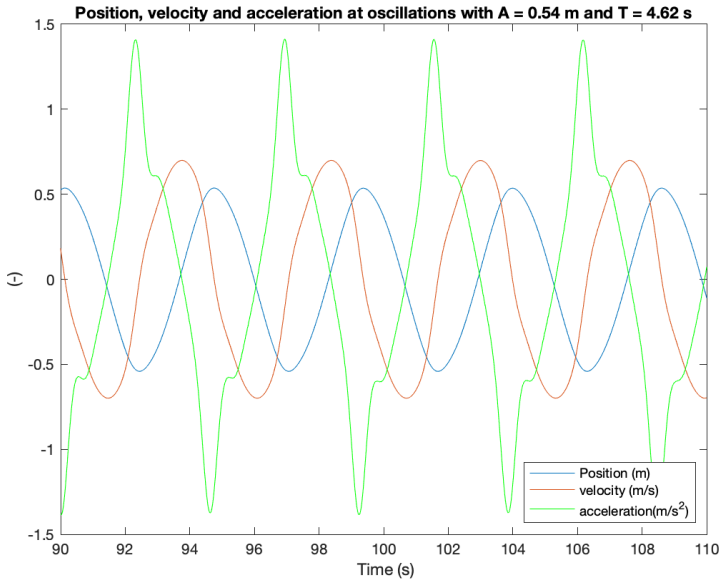

Figure 5.9: Position, velocity, and acceleration of an oscillation

The velocity signal exhibits a sinusoidal pattern with a slight deviation from a perfect sine wave in the first and third quarters of its period, while the second and fourth quarters have a steeper slope. To fit the velocity signal, a sum of two sine waves is used, which has a maximum root mean square error (RMSE) relative to the amplitude of 2% across all the test runs. The RMSE is the square root of the mean of the squared absolute difference between the fit and the data points, which is a tool to show the goodness of the fit. The peculiar shape of the velocity signal is even more apparent in the acceleration signal, which exhibits a large peak due to the steep period and flattened bend in the velocity signal. To fit the acceleration signal, a sum of four sine waves is used, resulting in a maximum RMSE relative to the amplitude of 1%. The accuracy of the fits is detailed in Table A.1 in appendix A, and the fitting process and accuracy definitions are further discussed in appendix A.

5.2.3. Calculating the drag and inertia coefficient

The velocity and acceleration data were modeled using a sum of two sinuses and a sum of four sinuses, respectively. These are the velocity and acceleration used for the Morison equation that fits the data points. The Morison equation was then fit to the data points, with the drag and inertia coefficients being treated as variables. This is shown in equation 5.2. Where rho is the density of water at 17 °C, U is the fitted velocity, L is the length of the dropper line model, D is the characteristic diameter, $\dot{U}$ is the fitted acceleration, and C_D and C_M are the drag and inertia coefficients treated as variables. To compensate for the force due to Newton's second law the last term is introduced where $m_{cylinder}$ is the mass of the model and the water inside.

$$F = \frac{1}{2}\rho D L C_D U|U| + \frac{1}{4}\pi\rho D^2 L C_M \dot{U} - \dot{U} * m_{cylinder} \tag{5.2}$$

The optimization procedure selected the drag and inertia coefficients that minimized the RMSE of the total fit. An illustration of such a fit, including the residual plot, is presented in figure 5.10.

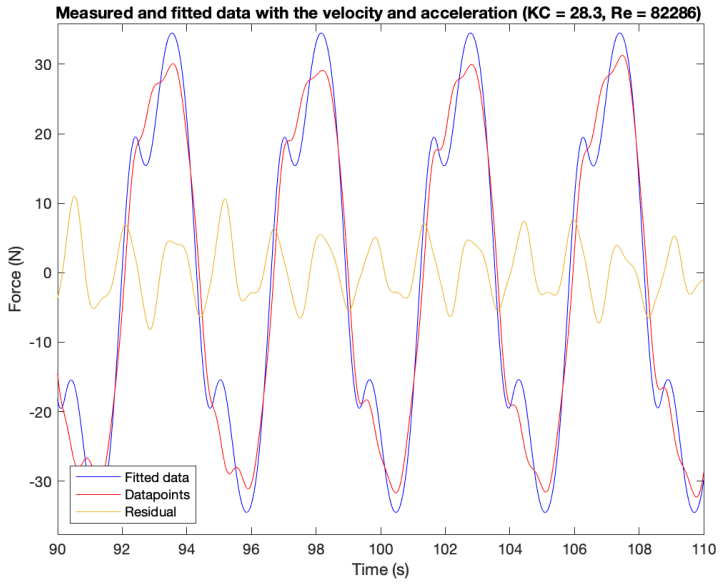

Figure 5.10: Fit of Morison force on the measured force data points

The total filtered force data is shown in figure 5.10 and is represented by the red curve, which exhibits characteristics consistent with a typical Morison curve (as shown in figure 5.7). The blue curve in the figure represents the fit of the Morison equation, which displays an additional oscillation at the Morison hump, as highlighted in figure 5.8. Despite appearing to be a reasonable fit, the RMSE relative to the amplitude is 11.84%. Notably, the fit and the data exhibit differences at the Morison hump and the peak of the amplitude. The accuracy of the fit, including the drag coefficient (C_D) and inertia coefficient (C_M), are presented in Table A.2 in appendix A

In addition to the RMSE, an important factor in determining the accuracy of the drag and inertia coefficients is whether the Morison force's drag and inertial components have their peak at a reasonable location. To assess this, the acceleration and velocity data are plotted alongside the force data and the corresponding Morison equation fit. The resulting plot is depicted in figure 5.11.

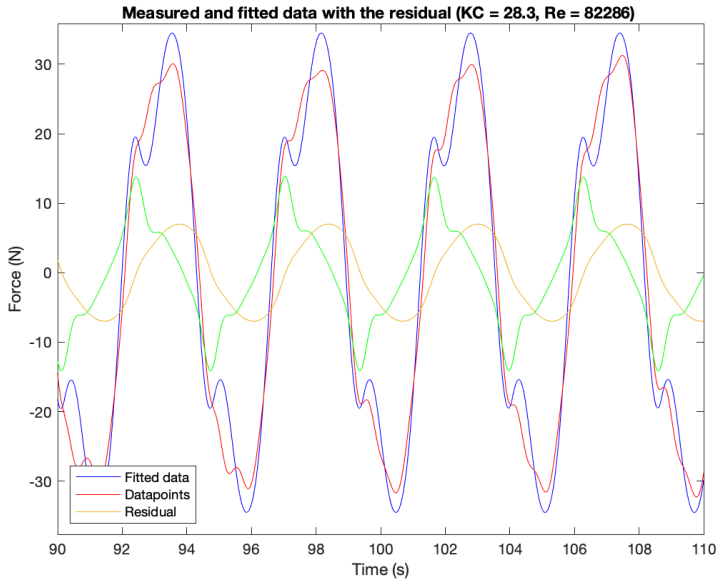

Figure 5.11: Fit of Morison force on the measured force data points with amplified velocity and acceleration

To better visualize the impact of the velocity and acceleration on the Morison force, their plots were amplified by a factor of -10, as they are in the opposite direction of the force and considerably smaller in magnitude. The acceleration exhibits a peak at the Morison hump, whereas the force peaks simultaneously with the velocity. Therefore, the drag coefficient is varied to determine the peak's location and the inertia coefficient to determine the Morison hump's location. Using this information, the obtained drag and inertia coefficients from the curve fit are evaluated in plots similar to figure 5.11 to see if the fits make sense.

5.3. Data processing waves

To ensure the accuracy of calculations for the drag and inertia coefficients in the Morison equation, the wave experiment data must first undergo a thorough examination. Given that the Morison equation operates under steady-state conditions, the ideal approach is to select a segment of the wave data that is as close to a steady state as possible. As such, the last five wave cycles with full amplitude have been determined to be the most appropriate for our calculations. This specific section can be identified as the red rectangles within figure 5.12, representing the most stable and consistent portion of the wave cycle. By using this portion of the data, the precision of the calculations can be maximized.

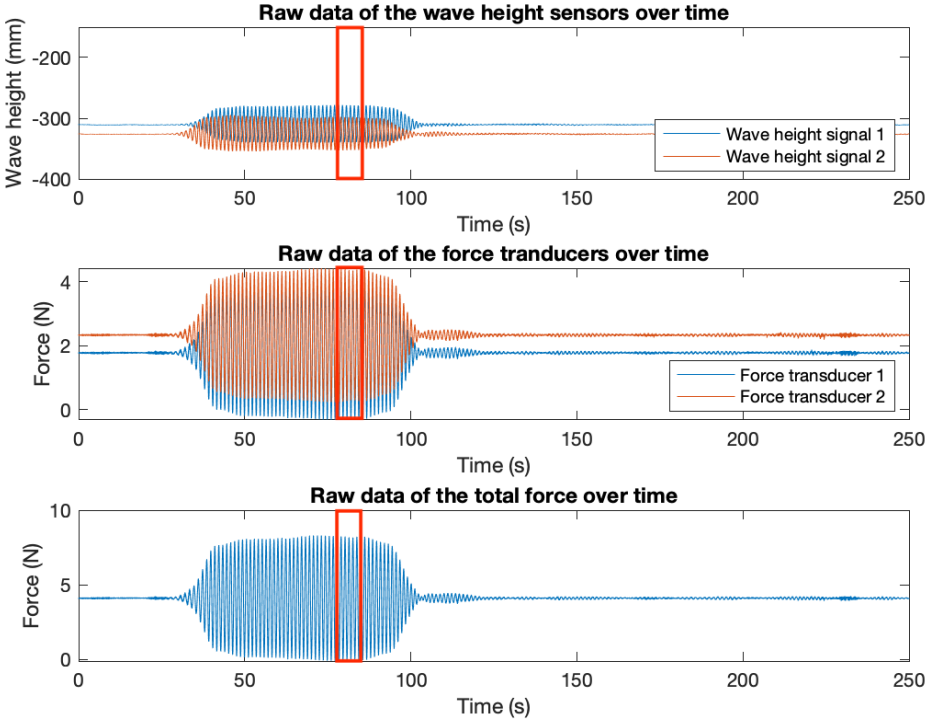

Figure 5.12: Raw wave data

In this experiment, the top plot of figure 5.12 shows that initially, the water was at rest, but waves gradually built up around 35 seconds into the test run. To measure the waves, two wave probes were used, one at the same height in the x-direction but at a higher y-coordinate, and the other at the same height in the y-direction but at a higher x-coordinate. This is shown by the wave height signals indicating that wave height signal 2 measured the waves 2.8 seconds earlier than wave height signal 1. After eight oscillations by the wave maker, full amplitude waves with an amplitude of 3 mm and a period of 1.19 seconds were measured for 40 wave cycles, followed by a decrease in amplitude for eight oscillations of the wave maker. The period of increasing and decreasing amplitudes was longer since the wave maker required a more extended starting and ending period compared to the linear motor. The waves generated by the wave maker had passed around 100 seconds, but the water remained noisy due to the experiment. As the test run progressed, the waves in the water eventually dampened out. This specific

test run involved 40 wave cycles since the reflective wave was negligible for small deep ocean waves. However, for test runs with longer wave periods, 15 full wave cycles were carried out, as described in subsection 4.6.2.

The middle plot of figure 5.12 shows the forces of the force transducer over time. Initially, the system was at rest with an offset for the first 35 seconds, after which the first wave loads were excited on the model. Both transducers responded with the same force amplitude but with different offsets due to their position. After the build-up of eight wave periods, the full amplitude wave loads were measured, and the last five of those full amplitude wave loads were used to calculate the drag and inertia coefficients as they were closest to a steady state. Following the full amplitude wave loads, the loads gradually decreased, and the controlled waves ceased, but some small waves were left that dampened out during the remainder of the test run.

Finally, the last plot of figure 5.12 shows the total force on the force transducers over time, which follows the same trajectory as the middle plot but then doubled. The force data from the red rectangle in this plot is used as data points to fit the Morison equation.

The wave and force data inside the red rectangles from both wave probes and the total force are shown in figure 5.13. Here the offset is subtracted from the signals, and the wave height is converted to meters.

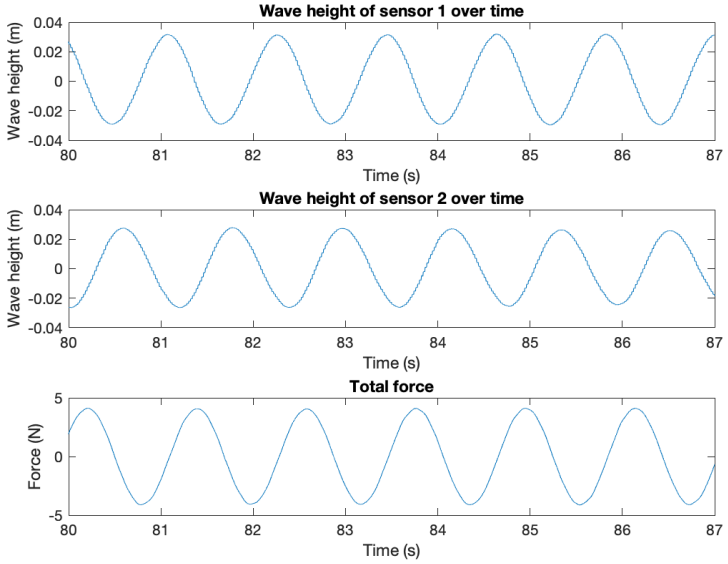

Figure 5.13: Wave data with the five oscillations used

The placement of the sensors is critical to ensure accurate measurements of the waves. Specifically, wave height sensor 1, which has the same x-coordinate as the model, measures the same phase of the wave, while wave height sensor 2, with the same y-coordinate as the model, measures the same amplitude of the wave. In forced oscillation experiments, the velocity and acceleration are determined by differentiating the position signal. However, in wave experiments, the velocity and acceleration are calculated using the amplitude, period, and phase of the wave, as well as the depth of the wave tank and the model.

To determine the phase of the waves, the measured phase from wave height sensor 1 is adjusted for a signal delay of 730 ms. This adjusted phase value is then used in subsequent calculations. To calculate the amplitude and period of the waves, the last five full amplitude waves measured by wave height sensor 2 are considered. The amplitude is determined by measuring the maximum vertical distance between the crest and trough of each wave, while the period is calculated as the time between two consecutive wave crests. Additionally, the depth of the wave tank is known to be 1.25 m, while the depth of the model measured from still water level is 0.48 m. These values are important inputs in the calculations for determining the velocity and acceleration of the wave.

The wave particle velocity and acceleration are calculated by equations 2.4 and 2.5. The phase

of the wave is essential in ensuring that the fit of the Morison equation, which is based on the wave particle velocity and acceleration, accurately matches the data points of the total measured force. Once the phase, velocity, and acceleration have been determined, the Morison force can be fitted to the data points. An example of this process is shown in figure 5.14.

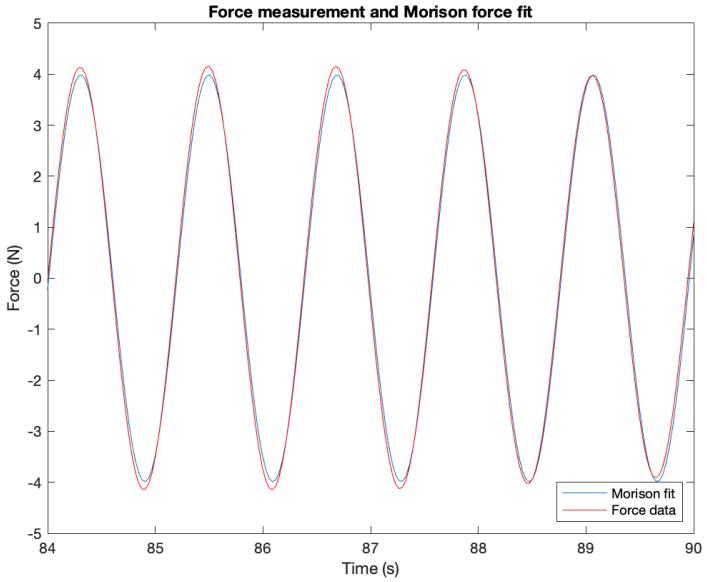

Figure 5.14: Wave data and the computed Morison force

Figure 5.14 depicts the Morison equation (blue curve) fitted to the data points obtained from measuring the total force acting on the model (red curve) in the wave tank. The accuracy of the fit is dependent on the precise determination of the wave particle velocity and acceleration.

The results of the drag and inertia coefficients of the wave tests are presented in appendix A. As can be observed, the Morison force has a different shape in wave tests than in forced oscillation experiments. This is primarily due to the orientation of the cylinder, which is horizontally positioned, which does not have an impact on the force in forced oscillations but it does for waves. This effect is further explained in appendix B.

6

Results and discussion

The results of the processed data from the conducted experiments can be found in this chapter. To evaluate the results the coefficients are calculated using the characteristic diameter and the outer diameter of the model. The results in this chapter begin with the towing experiments to get the drag coefficient and evaluate the results to the literature, afterward, the oscillation experiment to get the drag and inertia coefficient. Thereafter, the wave experiments for the drag and inertia coefficient. At last, the drag and inertia of the forced oscillation and wave experiments are compared.

6.1. Results drag coefficient towing

At every instance, thus the whole steady force interval per sample rate, the drag coefficient is calculated and for these values, the mean, standard deviation, and coefficient of variance are calculated. The coefficient of variance (CoV) shows the ratio of the standard deviation compared to the mean value. This is done for the velocity and force as well to see to what extent the variations in those parameters affect the outcome of the drag coefficient. The results are shown in table 6.1.

Table 6.1: Outcomes towing experiments

Reynolds	Velocity (m/s)			Force (N)			C_D(-)		
Mean	Mean	σ	Cov (%)	Mean	σ	CoV (%)	Mean	σ	CoV(%)
$9.6 * 10^4$	0.843	0.0012	0.14	25.32	0.24	0.93	1.19	0.011	0.94
$7.9 * 10^4$	0.695	0.0012	0.17	17.33	0.15	0.88	1.19	0.011	0.88
$6.2 * 10^4$	0.545	0.0012	0.21	10.44	0.12	1.11	1.18	0.014	1.16
$4.5 * 10^4$	0.397	0.0010	0.26	5.53	0.10	1.17	1.18	0.021	1.76
$2.8 * 10^4$	0.248	0.0010	0.39	2.14	0.07	3.06	1.17	0.036	3.06

Upon analyzing the data presented in table 6.1, is observed that the standard deviation of the velocity remained relatively constant across different velocity values. However, the CoV increased at lower speeds, primarily due to the decreasing mean velocity. This suggests that at lower speeds, there is a higher degree of variability in the velocity data compared to higher speeds relatively speaking.

In contrast, the standard deviation of the force showed a different pattern. The standard deviation of the force exhibited a significant change with increasing force, given that the force increase per run was relatively higher. While the standard deviation of the force decreased with decreasing mean force, the CoV increased. This indicates that the standard deviation was decreasing less as compared to the mean force, thereby increasing the variability in the force data.

Upon analyzing the data, it is observed that the standard deviation of the drag coefficient increased over lower velocities, while the mean remained constant. This results in an increase in the CoV with decreasing velocities. Interestingly, the CoV's of the force and drag coefficient were found to be almost the same, indicating a lack of correlation between the error of uncertainty in velocity and force. Furthermore, the standard deviation and CoV of the drag coefficient only changed due to variations in the force, suggesting that force and velocity are not correlated.

It is worth noting that force is induced by velocity, and as such, any change in force is typically associated with changes in velocity. However, the findings indicate that the variability in the force data is not correlated with the variability of the velocity data.

To provide an overview of the accuracy and median of the drag coefficients at different Reynolds values, the values of the drag coefficient are used to create boxplots. These boxplots are shown in figure 6.1. The boxplots provide a visual representation of the distribution of the drag coefficient values for each Reynolds number. The box in each plot represents the interquartile range (IQR) of the data, with the whiskers extending to the minimum and maximum values within 2.7 times the σ. Outliers beyond this range are shown as individual points.

The boxplots reveal that the median value of the drag coefficient generally increases with increasing Reynolds number, which is consistent with prior research. Additionally, the variability in drag coefficient values decreases at higher Reynolds numbers, with a greater number of outliers present. These findings underscore the higher uncertainty at lower Re values.

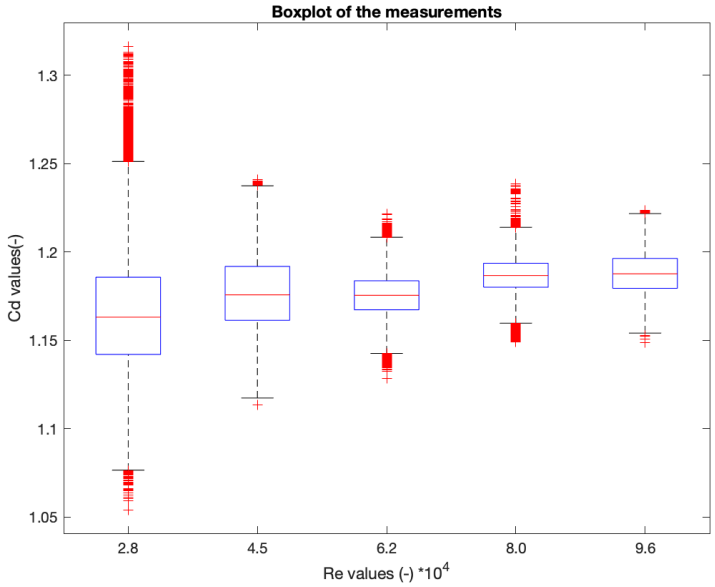

Figure 6.1: Boxplots of the different measurements, where the red crosses are the outliers, the red line is the median, and the blue box is the domain of the 25th and 75th percentile

As previously stated in the introduction of this chapter, the results of the drag coefficient calculations were evaluated by computing the mean drag coefficient using the outer diameter of the model, in addition to using the characteristic diameter. These results are summarized in table 6.2, which provides a comparison of the drag coefficients at different Reynolds numbers using both diameters.

Table 6.2: Evaluation of the effect of the diameter on the drag coefficient

	Outer diameter					Characteristic diameter				
Re $*10^4$ (-)	4.0	6.4	8.8	11.2	13.6	2.8	4.5	6.2	7.9	9.6
C_D (-)	0.82	0.83	0.83	0.84	0.84	1.17	1.18	1.18	1.19	1.19

The results show that the use of the outer diameter yields significantly lower drag coefficients compared to the use of the characteristic diameter, particularly at higher Reynolds numbers. This underscores the importance of carefully selecting the appropriate diameter for calculating drag coefficients, as the choice of diameter can have a significant impact on the resulting values.

To evaluate the different diameters used in table 6.2 a comparison of the drag coefficients is done between the literature and the results of this research. The relevant literature is discussed in section 1.2.1. Figure 6.2 shows the comparison of these drag coefficients.

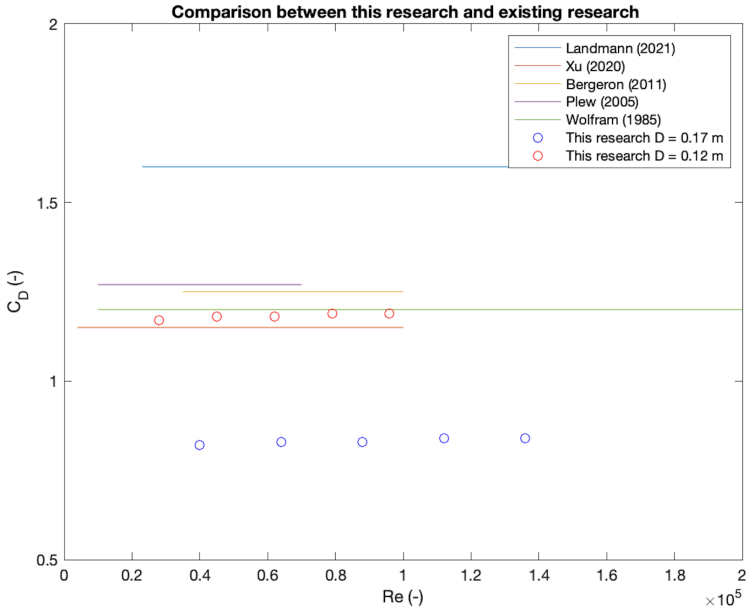

Figure 6.2: Comparison of results of this research with two different diameters and existing literature on dropper lines

To facilitate the comparison, the drag coefficients obtained from the literature are plotted as straight lines, although acknowledged that this is not a realistic representation. Nevertheless, this provides a fair indication of the results because it is noted that this research results in almost a straight line as well, indicating that this approach is reasonable.

In the literature, the lowest drag coefficient is reported in a CFD analysis of a rough and sharp cylinder, which yields a value of $C_D = 1.1$. The cylinder with marine mussel growth tested experimentally by Wolfram has a drag coefficient of $C_D = 1.2$. The drag coefficients obtained from our research using the characteristic diameter are in between these two values, which suggests that our results are reasonable.

The use of the outer diameter in computing drag coefficients resulted in significantly lower values that are difficult to compare to the literature. Therefore, using the characteristic diameter is recommended to compute drag coefficients in future studies.

6.1.1. Influence of the roughness

According to research done by Schoefs, a cylinder with marine growth of blue mussels can also be seen as a cylinder with a roughness of k/d between 0.06 and 0.085. The influence of the roughness is shown in figure 6.3, where the k/d range of the dropper line is shown in between the green lines.

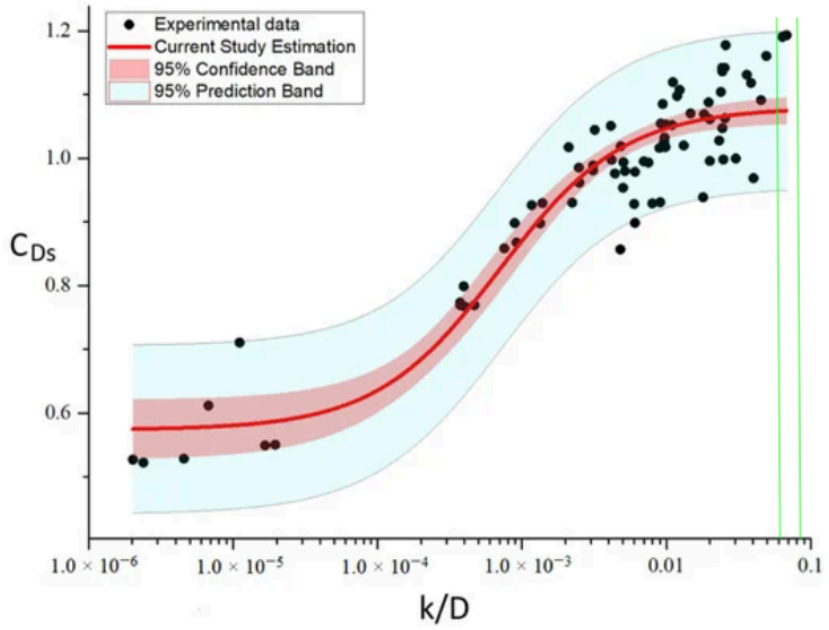

Figure 6.3: The influence of roughness on a cylinder (Schoefs, Bakhtiari, and Ameryoun 2022)

The values that belong to the roughness of a mussel line are in the range of the results of the experiments.

6.2. Results drag and inertia coefficients in forced oscillations

The drag and inertia coefficients of the dropper line were calculated for each experiment and are presented in Appendix A, along with confidence bounds and accuracy. These coefficients can be presented in different dimensionless combinations, but the KC number (Journée, Massie, and Huijsmans 2015) is considered the most realistic and useful parameter, sometimes augmented by using the Re number, β, or roughness as an additional curve. Figure 6.4 shows the drag and inertia coefficients of the dropper line, compared to those of a cylinder for reference.

The error bars in figure 6.4 are calculated based on the drag and inertia coefficients per amplitude of oscillation, rather than on the KC number, which can vary between different test runs. Two types of error bars are used: one based on the confidence interval of the different KC values (horizontal error bars), and the other based on the variability of the measured drag and inertia coefficients (vertical error bars). To account for this uncertainty, the error bar is multiplied by the error of the fits.

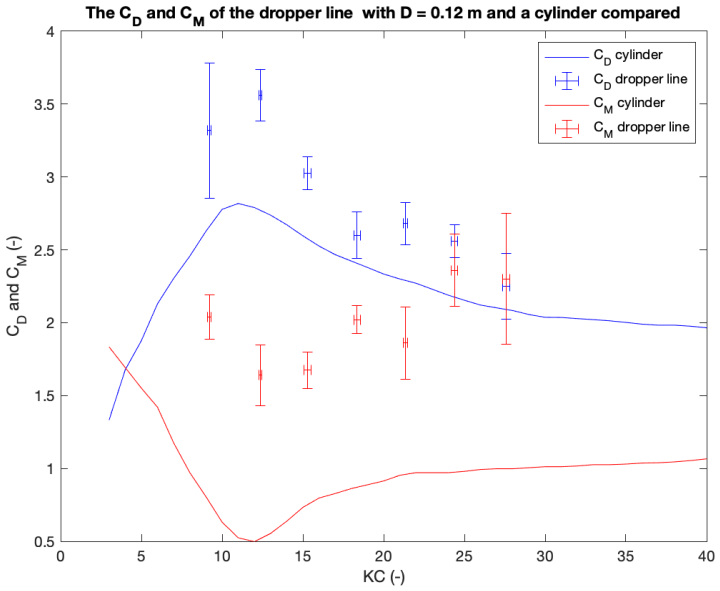

Figure 6.4: C_D and C_M of the dropper line (D = 0.12m) and a cylinder

The figure shows that the shape of the curve for the drag and inertia coefficients of the dropper line using the characteristic diameter resembles that of a cylinder, but the values are significantly higher. This could be attributed to the use of the characteristic diameter in the Morison equation, which was chosen to make the dropper line usable for calculations with the Morison equation. As the diameter increases, the drag and inertia coefficients decrease, but the KC also decreases. To provide a comparison, the drag and inertia coefficients of the outer diameter of the dropper line are also calculated and presented in figure 6.5, along with the drag and inertia coefficients of a cylinder.

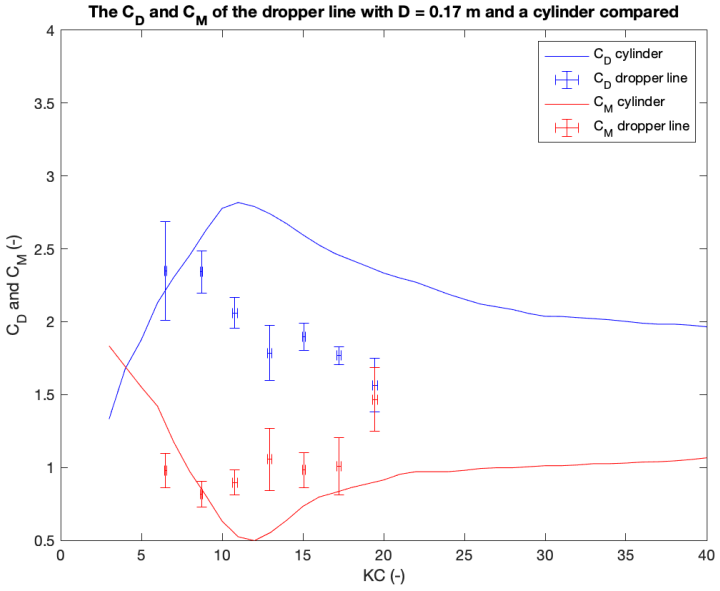

Figure 6.5: Comparison C_D and C_M of the dropper line model (D = 0.17m) and a cylinder

The shape of the curve is shifted towards the left due to the decreasing KC because of the larger diameter used. The values for the drag and inertia coefficient are more in the range of that of a smooth cylinder. Although it is more presumable that the drag and inertia coefficients are higher than that of a cylinder due to its shape. The shape and peaks of the results for the drag and inertia coefficient are

similar to that of the cylinder's drag and inertia coefficients in figure 6.4, which is more plausible than that the values are in range but the shape and peaks are shifted.
As observed in the comparison of the drag and inertia coefficients of the dropper line using characteristic and outer diameter presented in figures 6.4 and 6.5, the use of the characteristic diameter results in a more accurate representation of the peak and their location. This is consistent with the conclusion drawn in the previous section regarding the superiority of the characteristic diameter over the outer diameter.

As the drag and inertia values with the same KC and different Re are taken as a data point the influence of a different Re value with the same KC value is evaluated. To make it more clear which points belong to each other, lines are added but these are no trend lines. The trend line at the bottom of the plot belongs to research by Frank Schoefs on rough cylinders and marine biofouling. The plot is shown in figure 6.6

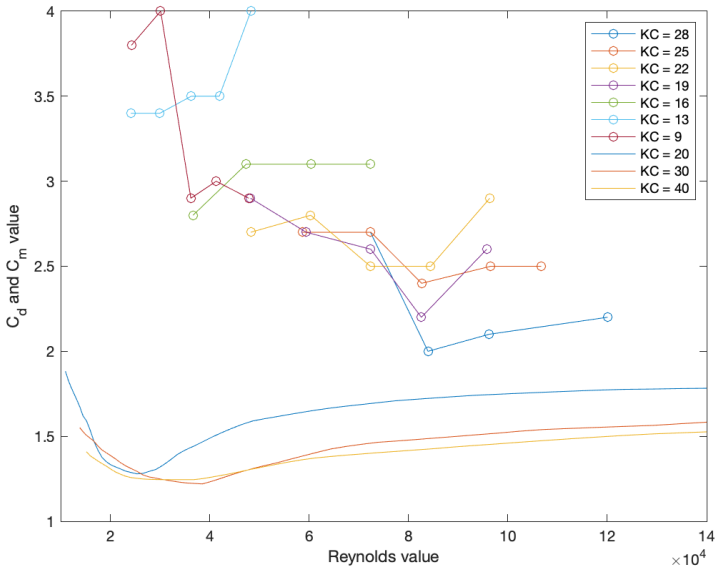

Figure 6.6: Influence of the Re on the drag coefficient of a rough cylinder with the same KC

The behavior of Schoefs' trend lines is somewhat observed in the results, where it can be seen that for Reynolds numbers above $1*10^4$, the lines rapidly decrease, reach a minimum, rapidly increase again, and then reach a stable stage with a slow equal increase. The intensity of this increase and decrease is different per KC value. The minimum is reached earlier and the stable stage is reached earlier for lower KC values. The drag coefficient values at KC values of 28, 25, 22, and 19 are comparable to the trend lines, but the KC values of 16, 13, and 9 are harder to compare because they are far from the trend line values. However, the trend lines do show that for most of the KC and Re value combinations, the drag coefficient should not differ more than 0.1 - 0.2 on the drag coefficient value on the total intervals, so taking the mean and confidence interval of these drag coefficients based on the same KC is reasonable based on the results of Schoefs research although the results of this research are a bit more scattered. It could be that with further research with more runs per data point, the curves would become smoother. In figure 6.6, it can be observed that the majority of the drag coefficients are widely scattered and there is a significant difference in one KC value compared to others. The data points for KC = 16 and KC = 22 are relatively similar, but there is a significant difference for the two lowest KC values. This observation is further supported by comparing the error bars of the drag coefficient from figure 6.4 and figure 6.6. For a lower KC, the range of drag coefficients is wider, indicating a higher degree of uncertainty in the results.

Based on the obtained results, it can be concluded that the dropper line model exhibits a shape that closely resembles that of a rough cylinder, despite the noticeably higher values observed. Nevertheless, the shape of the curve and the larger uncertainty observed with lower KCs suggest that assuming the dropper line's behavior to be that of a rough cylinder is a reasonable approximation. Therefore, these

findings could provide valuable insights to develop more accurate models and make better predictions for dropper line applications in practice.

6.3. Results drag and inertia coefficients in waves

The drag and inertia coefficients for the wave tests are presented similarly to the oscillation tests. However, since there is only one Re value per KC value, no error bars are shown. The results are displayed in figure 6.7. There are five data points per coefficient, except for the drag coefficient at a KC of 0.3, which is too high to fit in the plot. At a very low KC value, the inertia dominates, leading to a high value of the drag coefficient determined by the Curvefit to minimize the RMSE. However, this compensates for the lack of drag force. All the values for the drag and inertia coefficients and RMSEs are shown in Appendix A.

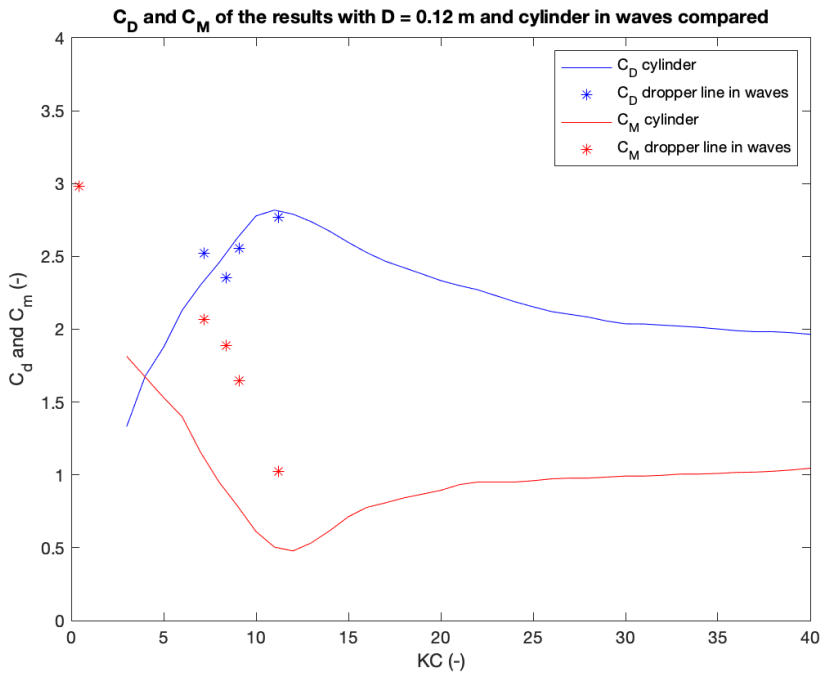

Figure 6.7: C_D and C_M of the dropper line in waves and of a cylinder (D = 0.12 m)

In this figure, the blue line represents the drag coefficient of a cylinder and the blue dots are the drag coefficients of the model. The red line represents the inertia coefficient of the cylinder and the red dots are the inertia coefficient of the dropper line. It can be observed that the dots follow the curves in their decrease and increase but are shifted upwards. The drag coefficient values of the dropper lines are 0.4 higher than those of the cylinder, while the inertia coefficient values of the dropper lines are 0.5 to 0.8 higher than those of the cylinder. To evaluate the influence of the diameter, the drag and inertia coefficients of the dropper line using the outer diameter are calculated again, and the results are shown in figure 6.8.

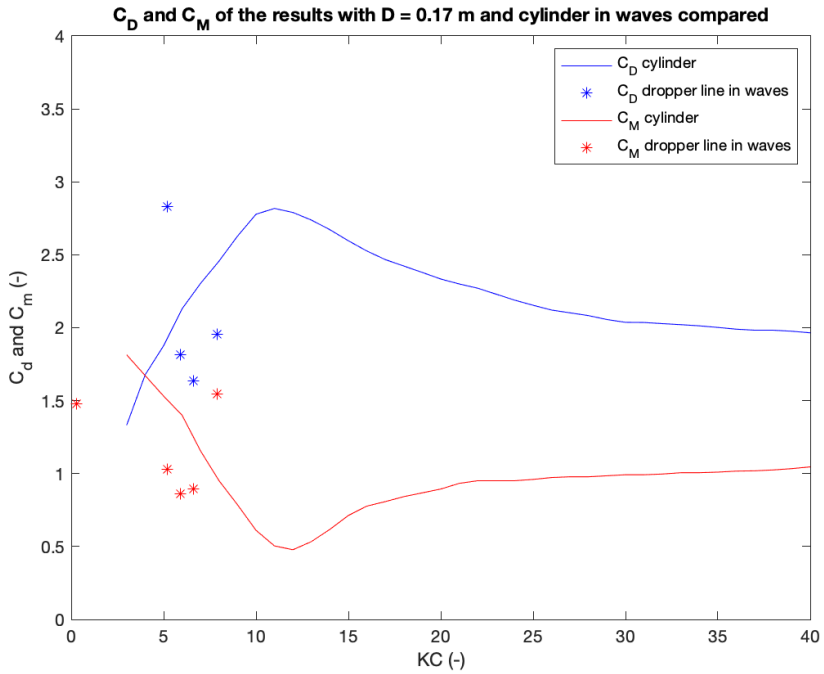

Figure 6.8: C_D and C_M of the dropper line in waves and a cylinder (D=0.17 m)

In figure 6.8 is seen that the drag coefficients of the dropper line are almost all on the line of the drag coefficient of the cylinder except for one real outlier. The inertia coefficient is even 0.6 - 0.8 lower than the inertia coefficient of the cylinder with one data point at KC = 10 where the inertia coefficient is 0.2 higher than the inertia coefficient of the cylinder.

The drag and inertia coefficients of the dropper line model using the characteristic diameter closely resemble the curves of the cylinder's drag and inertia coefficients. On the other hand, the data points of the outer diameter model are scattered and do not fit the curves well, except for three drag coefficient data points that are in close proximity to the cylinder's drag coefficient curve. These results suggest that the characteristic diameter is a more suitable assumption for the dropper line's drag and inertia coefficients in wave experiments.

6.4. Combining and comparing wave and oscillation results

The characteristic diameter seems to be appropriate, so the drag and inertia coefficient results are based on that, but there is a difference between the drag and inertia coefficients of the dropper line model of the forced oscillations and the waves. To put the forced oscillation and wave experiments into perspective the results of them are plotted in figure 6.9.

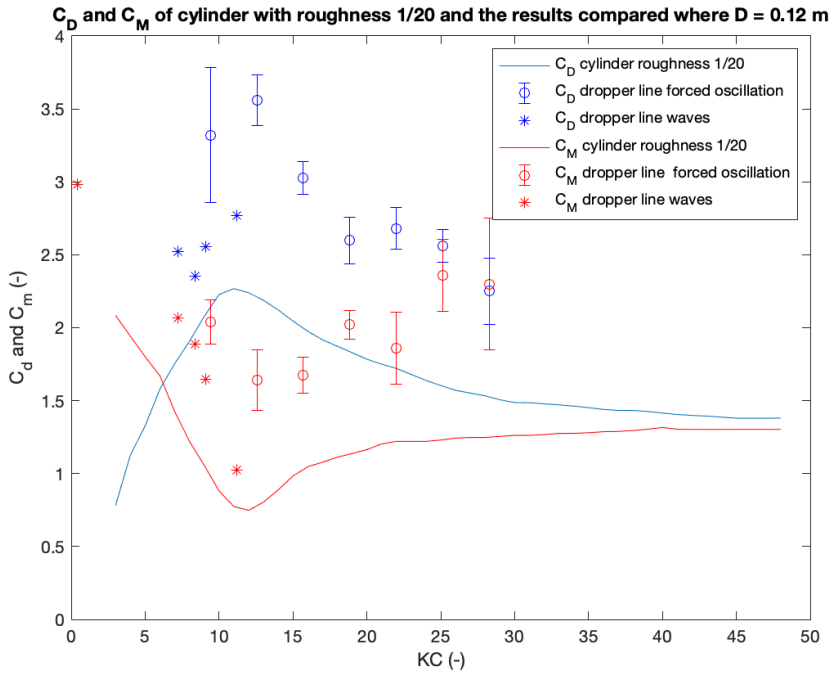

Figure 6.9: C_D and C_M of the dropper line in waves and oscillations and of a cylinder (D = 0.12 m)

In figure 6.9 both figure 6.4 and 6.7 are plotted together with the drag and inertia of the cylinder. For the drag coefficient, the difference between the results for the forced oscillations and waves is around 0.7 - 0.8 at a KC value between 10 and 14. For the inertia coefficient, the difference is around 0.4 - 0.6 at a KC value between 10 and 14. The results of these test runs are shown in table 6.3 to accurately look at this difference. The waves and oscillations runs are numbered for the convenience of reference.

Table 6.3: Comparison of wave and oscillations results

Experiment type	KC (-)	Re $*10^4$ (-)	C_D (-)	C_M (-)
Oscillation 1	9.3	2.4	3.77	1.73
Oscillation 2	9.3	3.0	4.03	1.96
Oscillation 3	9.1	3.5	2.88	2.20
Oscillation 4	9.3	4.1	3.00	2.10
Oscillation 5	9	4.6	2.93	2.22
Wave 1	9.1	3.4	2.56	1.65
Oscillation 6	12.5	2.4	3.36	1.53
Oscillation 7	12.5	3.0	3.42	1.71
Oscillation 8	12.3	3.5	3.49	1.42
Oscillation 9	12.4	4.1	3.50	1.48
Oscillation 10	12.2	4.7	4.02	2.05
Wave 2	11.2	2.9	2.77	1.07

Comparing specific oscillations and waves, oscillation 3 and wave 1 resemble each other with a difference in drag and inertia coefficients of 0.32 and 0.55, respectively. For wave 2, it is harder to make a comparison with a specific oscillation. Oscillations 2 and 7 have almost the same Re value, but the KC value is in between. Therefore, for comparison, interpolation is done to obtain a drag and inertia coefficient for a KC of 11.2. The interpolated drag and inertia coefficients are 3.63 and 1.80, resulting in a difference of 0.86 and 0.73, respectively. However, it should be noted that comparing these single test results and even interpolating has a big uncertainty, and these results are only indicative.

These differences could be due to the free surface effects or by wrongly compensating for the Froude-Krylov force in forced oscillation experiments, which is usually done by draining the wave tank

and conducting the experiments again without any water. However, in this study, the cylinder model was hollow and filled with water, which would still not result in the right Froude-Krylov that needed to be accounted for. To address this, the Froude-Krylov force was calculated based on the mass of the cylinder model, the 3D-printed block, and the water. It is important to note that if the cylinder was solid and the force was directly measured instead of being calculated, the resulting coefficients may differ.

6.4.1. Influence of roughness

As stated in subsection 6.1.1 the k/d of a dropper line is between 0.06 and 0.085. In figure 6.10 the drag and inertia coefficient of cylinders with different roughness are shown. What can be seen is that as the roughness increases the drag coefficient increases and the inertia coefficient decreases. The curve that represents a cylinder with a roughness of 1/20 is close to that of the dropper line.

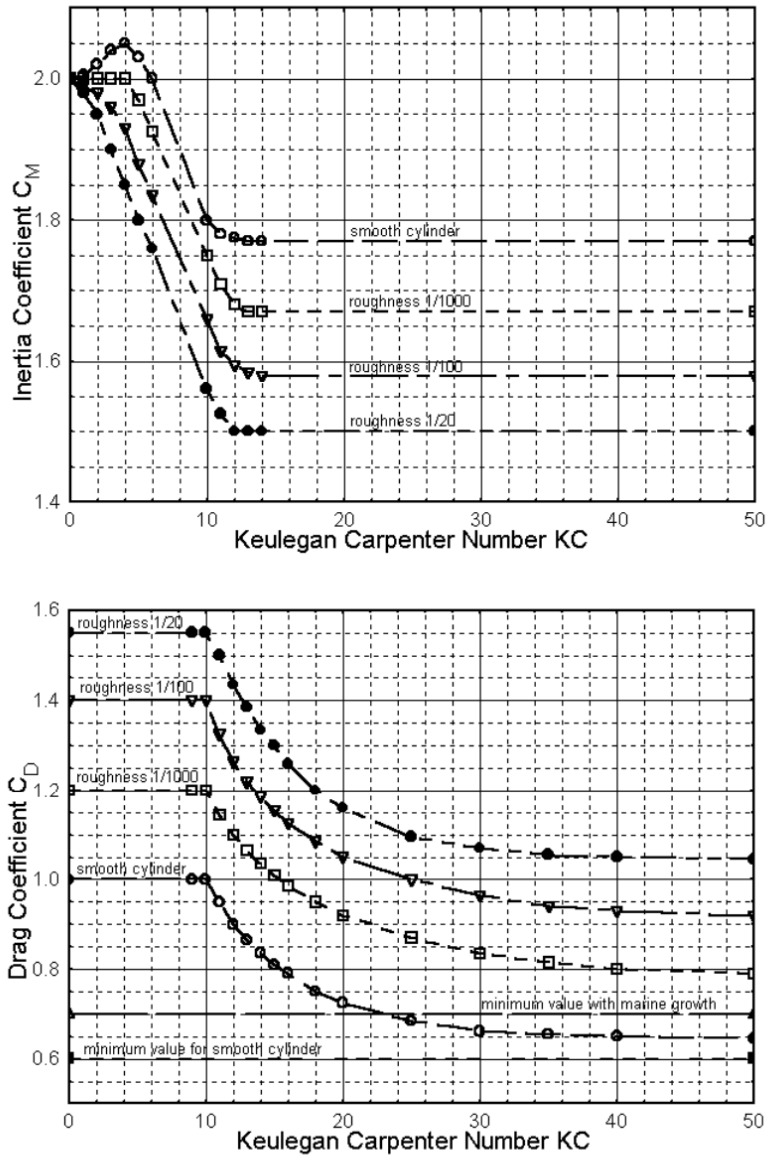

Figure 6.10: Suggested drag and inertia coefficient values from Det Norske Veritas (DNV) (Journée, Massie, and Huijsmans 2015)

So, according to the figure the inertia coefficient of the dropper line should be around 0.27 lower

than that of the smooth cylinder, and the drag coefficient of the dropper line should be around 0.55 higher than the smooth cylinder. The curves of the smooth cylinder are adjusted with the values stated above and shown in figure 6.11

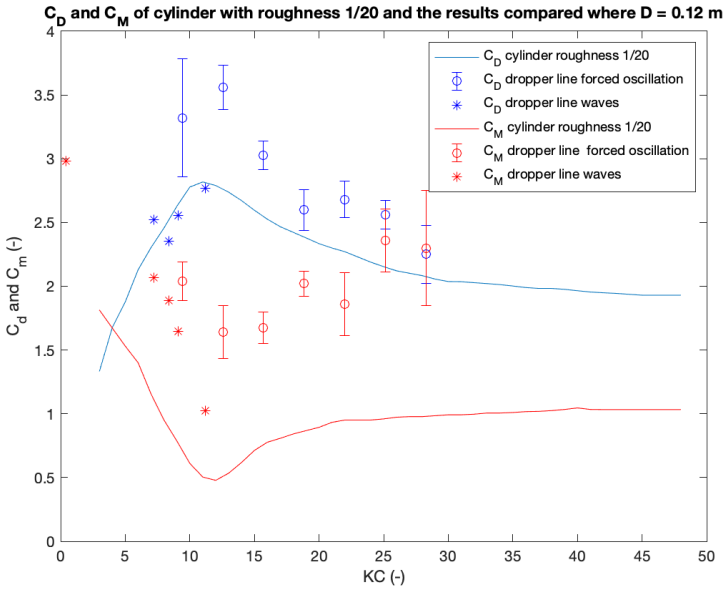

Figure 6.11: C_D and C_M of the dropper line in waves and oscillations and of a cylinder with a roughness of 1/20

The adjustments show that the drag coefficients become really close to each other for the wave experiments and the theoretical cylinder with a roughness of 1/20. The gap between the inertia coefficient for both experiments and the theoretical cylinder with a roughness of 1/20 became bigger.

7

Conclusion

The purpose of this research was to determine the drag and inertia coefficients of a dropper line in high Reynolds and intermediate Keulegan-Carpenter numbers. These numbers were valuable for numerical models of long line systems specifically for Coastbusters since most of the experimental parameters and the model were based on their specific site. It can be used for other parties using long line systems as well. In this chapter, the main research question is addressed and the key conclusions derived from the sub-research questions are presented. The first section draws a conclusion that addresses the sub-research questions, and the next section draws a conclusion that addresses the main research question. Ending with the recommendations provided in the last section.

7.1. Answer to research sub-questions

Research sub-question 1: ***How do the results relate to the literature?***
Over the years several types of research were done on the drag coefficient of a dropper line. Either numerical models for example CFD were used, or physical experiments in either the open ocean or in a wave tank were performed. The outcomes of these experiments and models were shown in figure 6.2. With most literature ranging from 1.1 to 1.3 for the drag coefficient it can be concluded that the shape does resemble a real dropper line comparable to the research of Gagnon or a rough and sharp cylinder comparable to the research of Xu. Landmann's research is not comparable to the values acquired in this research although, the research method is the most similar to this research. In Landmann, no end plates are used, which would even increase the C_D, and the force transducers are positioned so that some forces and moments had to be compensated. The dropper line in Landmann does have soft growth in between the mussels, which possibly increases the drag.

The biggest uncertainty in defining the model is what diameter is used to make it applicable to the Morison equation. From the results of the towing can be seen that the characteristic diameter used is a reasonable diameter. Larger diameters would result in nonrealistic drag coefficients for a dropper line. Landmann concluded that the method of average diameter is best to calculate the characteristic diameter. Although in this research, it was concluded that for practical reasons the displaced volume method is better suited. Since the research is done to create numerical models for a real site it is more convenient to use a practical method of determining the characteristic diameter.

Research sub-question 2: ***What is the difference between forced oscillation and wave experiments?***

The drag and inertia coefficients of the forced oscillation experiments both follow the shape of the drag and inertia coefficients of a cylinder over the KC value. The difference is that the magnitude of the drag coefficient at the forced oscillations is around 0.8 higher and the inertia coefficient around 0.6. The wave experiments are more realistic so the increase in the magnitude of the forced oscillations has to be declared. In the forced oscillations the forces have to be compensated for the Froude-Krylov force. Normally this is done by draining the wave tank and conducting the experiments again, but since the cylinder was hollow and filled with water this would still not be the right compensation. In

the processing, this force is calculated based on the mass of the model, the 3D-printed block, and the water. It could be possible that the coefficients would be different when the cylinder was solid and the force was measured instead of calculated.

Also, in the forced oscillation experiments the model is constantly moving through flow induced by the previous oscillations. Although, in the wave experiments these flows are constantly moving around the model. This could possibly increase the drag and inertia coefficients of the model, or the free surface effects are more relevant in forced oscillations than in waves.

7.2. Answer to main research question

What are the drag and inertia coefficients of a dropper line in high Reynolds and intermediate Keulegan-Carpenter numbers

Due to the gap in the existing literature in this research the drag coefficient in current and the drag and inertia coefficients in oscillating flow in high Reynolds and intermediate Keulegan-Carpenter numbers are examined. The results of all the different experiments are shown in appendix A and displayed with averaged Re in figure 6.9 for both waves and oscillations. A 3D printed dropper line model is used which shows to be an accurate representation of a real dropper line.

The drag and inertia coefficients of the dropper line model resemble the cylinder only the values differ, also for the waves and forced oscillations. The drag coefficient of a rough cylinder is close to the same value only the inertia coefficient differs more. Since the waves are more realistic these values can be used. The data of the forced oscillations can be used as well, but this will probably overestimate the Morison force.

7.3. Overall conclusion

What can be concluded from this research is that the model does resemble a dropper line based on the towing tests, and the wave experiments are more realistic results for oscillatory flow, while the linear motor overestimates the drag and inertia coefficient. In the recommendations, some points are addressed to make the forced oscillations experiments more realistic in the future. Also, the cylinder with a roughness of 1/20 was close to the results of the wave experiments. Several research in the literature stated that a roughened cylinder or pile could be used to imitate the dropper line, which is not a bad assumption based on these results. Only for the inertia coefficient it might be an underestimation.

7.4. Recommendations

This work was focused on simulating the single mussel longline reaction under various environmental circumstances, despite the fact that mussel farms are often vast enterprises with numerous longlines. If changes to environmental variables, such as current shadowing and spatial differences in currents and waves, are taken into consideration, it is anticipated that the approach will be applicable to bigger farms.

Scaling the dropper model was hard due to the scaling of the parameters, although wave experiments are more realistic. In future work, it is possible to try to scale it again or to do experiments on what causes the difference in drag and inertia coefficients in forced oscillations and waves.

Although it was shown that the model did resemble a real dropper line it does have some unrealistic aspects. The spaces in between the segments that are clear of mussels and all the mussels are facing upwards and never downwards, for better printing. In a real dropper line, this would not happen. The model was printed quite roughly, which did increase its realness. Also, the dropper line model has the same diameter all over, has no soft growth, and the mussels are solid with no inhalant and exhalant siphons. These were all well-made choices for this research, but varying the diameter or designing mussels with inhalant and exhalant siphons, or with soft growth might be interesting for further testing.

The model test setup could have been made airtight so the forces of Newton's second law of motion could be measured. This would be more accurate than calculating these forces. Although making it airtight would give a lot of problems when dismantling the cylinder in case something was wrong with the transducers for example.

The acceleration at the forced oscillations experiments was not a sinusoidal shape. This could be improved by tuning the PID controller of the linear motor more elaborately. With a better tuned PID the acceleration could become smoother.

References

Barbier, Edward B. and Evamaria W. Koch (Jan. 2008). “Coastal ecosystem-based management with nonlinear ecological functions and values”. In: *Science* 319 (5861), pp. 321–323. ISSN: 00368075. DOI: 10.1126/science.1150349.

Batchelor, G. K. (2000). *An Introduction to Fluid Dynamics*. Cambridge Mathematical Library. Cambridge University Press. DOI: 10.1017/CBO9780511800955.

Bergdahl, Lars (2017). *Mooring Design for WECs*, pp. 159–202. DOI: 10.1007/978-3-319-39889-1_7.

Boccotti, Paolo, Felice Arena, and Vincenzo Fiamma (2013). “Two small-scale field experiments on the effectiveness of Morison’s equation”. In: *Ocean Engineering* 57, pp. 141–149. ISSN: 0029-8018. DOI: https://doi.org/10.1016/j.oceaneng.2012.08.011. URL: https://www.sciencedirect.com/science/article/pii/S0029801812003277.

Brennen, Christopher E (1982). *A Review of Added Mass and Fluid Inertial Forces*. URL: https://www.researchgate.net/publication/30759285.

Cazenave, Anny and William Llovel (Jan. 2010). “Contemporary sea level rise”. In: *Annual Review of Marine Science* 2 (1), pp. 145–173. ISSN: 19411405. DOI: 10.1146/annurev-marine-120308-081105.

Cheong, So Min, Brian Silliman, and Poh Poh Wong (Sept. 2013). “Coastal adaptation with ecological engineering”. In: *Nature Climate Change* 3 (9), pp. 787–791. ISSN: 1758678X. DOI: 10.1038/nclimate1854.

Clancy, L (Jan. 1975). *Aerodynamics*. John Wiley and Sons.

Consortium, Coastbusters (2021). *Building Biogenic Reefs For Ecosystem-based Coastal Management*.

Day, John W., Donald F. Boesch, and Ellis J Clairain (2007). *Restoration of the mississippi delta: lessons from hurricanes Katrina and Rita*. URL: https://www.science.org.

Dhanak, Manhar and Nikolaos Xiros I (July 2016). *Springer Handbook of Ocean Engineering (Springer Handbooks)*. 1st ed. 2017. Springer.

Fu, Shixiao, Yuwang Xu, and Ying Chen (May 2014). “Seabed Effects on the Hydrodynamics of a Circular Cylinder Undergoing Vortex-Induced Vibration at High Reynolds Number”. In: *Journal of Waterway, Port, Coastal, and Ocean Engineering* 140 (3). ISSN: 0733-950X. DOI: 10.1061/(asce)ww.1943-5460.0000241.

Gagnon, Marc (Nov. 2019). “Self-organization and mechanical properties of mussel culture suspensions: A critical review”. In: *Aquacultural Engineering* 87. ISSN: 01448609. DOI: 10.1016/j.aquaeng.2019.102024.

Gagnon, Marc and Pierre Bergeron (Aug. 2017). “Observations of the loading and motion of a submerged mussel longline at an open ocean site”. In: *Aquacultural Engineering* 78, pp. 114–129. ISSN: 01448609. DOI: 10.1016/j.aquaeng.2017.05.004.

Holthuijsen, Leo H. (2007). *Waves in oceanic and coastal waters*. eng. Cambridge, UK: Cambridge University Press. ISBN: 9780521129954.

ITTC (2014). *Recommended Procedures and Guidelines Captive Model Test Procedure*, p. 20.

Journée, J, W Massie, and R Huijsmans (2015). *Offshore Hydromechanics Third Edition*.

Kallinderis, Y., K. Schulz, and W. Jester (Dec. 2001). “Application of Navier-Stokes Methods to Predict Vortex-Induced Vibrations of Offshore Structures”. In: *Parallel Computational Fluid Dynamics 2000* 1.2, p. 31. DOI: 10.1016/b978-044450673-3/50074-9. URL: http://dx.doi.org/10.1016/b978-044450673-3/50074-9.

Keulegan, G.H. and L.H. Carpenter (May 1958). “Forces on cylinders and plates in an oscillating fluid”. In: *Journal of Research of the National Bureau of Standards* 60.5, p. 423. DOI: 10.6028/jres.060.043. URL: http://dx.doi.org/10.6028/jres.060.043.

Landmann, Jannis et al. (Sept. 2021). “Drag and inertia coefficients of live and surrogate shellfish dropper lines under steady and oscillatory flow”. In: *Ocean Engineering* 235. ISSN: 00298018. DOI: 10.1016/j.oceaneng.2021.109377.

Langedock, Kobus, Geoffrey Johnen, and Hans Pirlet (2020). *Coastbusters 2.0 - Factual data report of existing hydro-meteo background parameters*.

Mathworks (2001). *For Use with MATLAB® User's Guide Curve Fitting Toolbox*. URL: www.mathworks.com.

Mcleod, Elizabeth and Rodney V. Salm (2006). *Managing Mangroves for Resilience to Climate Change IUCN Global Marine Programme*. URL: www.nature.org/marine..

Morison, J.R., J.W. Johnson, and S.A. Schaaf (May 1950). "The Force Exerted by Surface Waves on Piles". In: *Journal of Petroleum Technology* 2.05, pp. 149–154. ISSN: 0149-2136. DOI: 10.2118/950149-G. eprint: https://onepetro.org/JPT/article-pdf/2/05/149/2238818/spe-950149-g.pdf. URL: https://doi.org/10.2118/950149-G.

Nicholls, Robert J., Poh Poh Wong, and Virginia Burkett (Apr. 2008). "Climate change and coastal vulnerability assessment: Scenarios for integrated assessment". In: vol. 3, pp. 89–102. DOI: 10.1007/s11625-008-0050-4.

Plew, David Russell (2005). *The Hydrodynamic Effects of Long-line Mussel Farms*.

Rockwell, D., M. Ozgoren, and N. Saelim (2004). "Self-excited oscillations of vertical and horizontal cylinders in presence of a free-surface". In: *Fluid Mechanics and its Applications,* pp. 201–210. DOI: 10.1007/978-94-007-0995-9_14.

Rodriguez, Karen, Daniela Triana, and Raul Ortiz (Sept. 2019). "Experimental methods for the study of standing waves in strings". In: p. 8.

Sarpkaya, Turgut (1976). "In - line and transverse forces, on cylinders in oscillatory flow at high Reynolds numbers." In: *Offshore Technology Conference*. DOI: 10.4043/2533-ms.

Schoefs, Franck, Arash Bakhtiari, and Hamed Ameryoun (May 2022). "Evaluation of Hydrodynamic Force Coefficients in Presence of Biofouling on Marine/Offshore Structures, a Review and New Approach". In: *Journal of Marine Science and Engineering* 10 (5). ISSN: 20771312. DOI: 10.3390/jmse10050558.

Scyphers, Steven B., Sean P. Powers, and Kenneth L. Heck (2011). "Oyster reefs as natural breakwaters mitigate shoreline loss and facilitate fisheries". In: *PLoS ONE* 6 (8). ISSN: 19326203. DOI: 10.1371/journal.pone.0022396.

Slobbe, E. van, H. J. de Vriend, and S. Aarninkhof (Jan. 2013). "Building with Nature: In search of resilient storm surge protection strategies". In: *Natural Hazards* 65 (1), pp. 947–966. ISSN: 0921030X. DOI: 10.1007/s11069-012-0342-y.

Sreenivasan, A. Aravind Raghavan and B. Kannan Iyer (Sept. 2019). "Enhanced wall turbulence model for flow over cylinder at high Reynolds number". In: *AIP Advances* 9 (9). ISSN: 21583226. DOI: 10.1063/1.5118421.

Stevens, Craig, David Plew, and Neil Hartstein (June 2008). "The physics of open-water shellfish aquaculture". In: *Aquacultural Engineering* 38 (3), pp. 145–160. ISSN: 01448609. DOI: 10.1016/j.aquaeng.2008.01.006.

Streeter, Victor L and Ruth C Wylie (1979). *Fluid mechanics / Victor L. Streeter, E. Benjamin Wylie.* eng. 7th ed. New York: McGraw-Hill. ISBN: 0070622329.

Thompson, Marc T. (2014). *Analog Low-Pass Filters*. Elsevier, pp. 531–583. DOI: 10.1016/b978-0-12-405866-8.00014-0.

Wang, Jungao, Shixiao Fu, and Rolf Baarholm (2014). "Fatigue damage of a steel catenary riser from vortex-induced vibration caused by vessel motions". In: *Marine Structures* 39, pp. 131–156. ISSN: 09518339. DOI: 10.1016/j.marstruc.2014.07.002.

Xu, Zhijing, Hongde Qin, and Peng Li (2020). "Computational fluid dynamics approaches to drag and wake of a long-line mussel dropper under tidal current". In: *Science Progress* 103.1. PMID: 32024433, p. 0036850419901235. DOI: 10.1177/0036850419901235. URL: https://doi.org/10.1177/0036850419901235.

A

Results and accuracy

In this appendix, the results and the accuracy are displayed. For the towing test the accuracy of the velocity, force, and drag coefficient are presented. For the oscillation experiments, the velocity, acceleration, force, drag coefficient, and inertia coefficient are presented. Lastly, for the wave experiments, the accuracy of the drag and inertia coefficient is given.
The velocity, acceleration, and force are fitted using the Curvefit application of Matlab. The Curve fit gives the formula with the lowest RMSE, which is in the table as well. The RMSE is an absolute value so to determine how well the fit is the maximum of the velocity acceleration or force is given. The accuracy is given by the percentage of the RMSE of the maximum.

Table A.1: Accuracy and outcomes of the velocity and acceleration fits

Oscillation		Acceleration			Velocity		
A(m)	T(s)	Accuracy (%)	RMSE	Max a (m/s^2)	Accuracy (%)	RMSE	Max v (m/s)
0.54	5.36	1.28	0.009	0.73	1.66	0.010	0.63
0.54	4.62	1.02	0.010	0.98	1.21	0.009	0.72
0.54	4.03	1.71	0.022	1.27	2.88	0.024	0.82
0.54	3.23	3.80	0.075	1.97	2.43	0.025	1.02
0.48	5.88	1.23	0.007	0.54	2.08	0.011	0.50
0.48	4.76	1.74	0.014	0.81	2.87	0.018	0.61
0.48	4.17	1.52	0.016	1.05	2.28	0.016	0.70
0.48	3.57	1.60	0.023	1.43	2.21	0.018	0.81
0.48	3.23	1.60	0.028	1.78	1.32	0.012	0.91
0.42	6.25	1.52	0.006	0.42	2.37	0.010	0.41
0.42	5.00	1.73	0.011	0.64	2.76	0.014	0.52
0.42	4.17	1.81	0.017	0.92	2.82	0.017	0.61
0.42	3.57	2.26	0.028	1.25	2.83	0.020	0.71
0.42	3.13	3.74	0.062	1.65	1.29	0.011	0.82
0.36	5.36	1.56	0.008	0.48	2.76	0.011	0.41
0.36	4.35	2.01	0.018	0.90	2.98	0.015	0.51
0.36	3.57	1.48	0.016	1.07	2.20	0.013	0.61
0.36	3.13	1.47	0.021	1.40	2.37	0.017	0.70
0.36	2.70	1.40	0.027	1.93	1.73	0.014	0.83
0.3	5.88	1.07	0.004	0.34	1.84	0.006	0.32
0.3	4.55	1.93	0.011	0.55	2.98	0.012	0.40
0.3	3.57	1.65	0.015	0.89	2.87	0.015	0.51
0.3	2.98	1.72	0.022	1.28	2.74	0.017	0.61
0.24	7.14	1.24	0.002	0.19	0.81	0.002	0.21
0.24	5.75	1.01	0.003	0.29	0.65	0.002	0.26
0.24	4.75	1.34	0.006	0.41	2.29	0.007	0.31
0.24	4.11	2.43	0.013	0.55	1.46	0.005	0.36
0.24	3.57	1.33	0.012	0.90	2.87	0.015	0.51
0.18	5.33	1.18	0.003	0.25	1.14	0.002	0.21
0.18	4.29	1.24	0.005	0.38	0.84	0.002	0.26
0.18	3.57	1.69	0.009	0.54	3.06	0.009	0.31
0.18	3.13	1.02	0.007	0.71	2.06	0.007	0.36
0.18	2.70	1.46	0.014	0.94	3.03	0.012	0.40

Table A.2: Accuracy and outcomes of the fit to the measured data points

A(m)	T(s)	C_D	bounds	C_M	bounds	RMSE	F_{amp} (N)	Accuracy (%)
0.54	5.36	2.74	(2.72,2.76)	2.70	(2.65,2.74)	4.70	25.48	18.45
0.54	4.62	2.02	(2.01,2.03)	2.69	(2.66,2,71)	3.93	33.19	11.84
0.54	4.03	2.09	(2.07,2.10)	1.99	(1.97,2.00)	4.63	41.80	11.08
0.54	3.23	2.24	(2.22,2.27)	1.67	(1.61,1.73)	12.60	76.76	16.41
0.48	5.88	2.68	(2.66,2.71)	2.10	(2.09,2.12)	4.56	19.17	23.80
0.48	4.76	2.66	(2.64,2.68)	2.01	(1.98,2.03)	4.50	26.92	16.72
0.48	4.17	2.45	(2.44,2.46)	2.37	(2.34,2.40)	4.72	34.70	13.60
0.48	3.57	2.51	(2.50,2.53)	2.93	(2.91,2.96)	6.54	48.95	13.35
0.48	3.23	2.55	(2.53,2.56)	2.38	(2.35,2.41)	7.76	65.17	11.91
0.42	6.25	2.72	(2.71,2.73)	1.63	(1.61,1.64)	1.33	13.72	9.69
0.42	5.00	2.81	(2.80,2.82)	1.53	(1.52,1.55)	1.99	21.67	9.18
0.42	4.17	2.54	(2.52,2.55)	2.11	(2.08,2.13)	3.73	28.83	12.94
0.42	3.57	2.51	(2.50,2.53)	2.23	(2.20,2.26)	5.43	39.93	13.59
0.42	3.13	2.85	(2.84,2.87)	1.93	(1.91,1.95)	6.44	53.93	11.94
0.36	5.36	2.87	(2.86,2.88)	1.88	(1.86,1.90)	1.55	13.80	11.23
0.36	4.35	2.73	(2.72,2.75)	2.08	(2.07,2.10)	2.00	22.95	8.72
0.36	3.57	2.58	(2.56,2.60)	2.09	(2.07,2.12)	3.67	29.40	12.49
0.36	3.13	2.20	(2.17,2.23)	2.13	((2.09,2.17)	7.50	37.98	19.75
0.36	2.70	2.60	(2.58,2.61)	1.95	(1.92,1.97)	5.33	65.78	8.10
0.3	5.88	2.80	(2.79,2.81)	1.88	(1.88,1.89)	0.59	9.26	6.37
0.3	4.55	3.08	(3.06,3.11)	1.72	(1.70,1.75)	2.39	14.46	16.53
0.3	3.57	3.09	(3.06,3.12)	1.62	(1.59,1.66)	4.70	23.30	20.17
0.3	2.98	3.07	(3.03,3.11)	1.52	(1.47,1.57)	8.03	33.11	24.25
0.24	7.14	3.36	(3.35,3.36)	1.53	(1.52,1.54)	0.35	4.63	7.55
0.24	5.75	3.42	(3.41,3.43)	1.71	(1.69,1.72)	0.64	7.27	8.87
0.24	4.75	3.49	(3.47,3.51)	1.42	(1.40,1.43)	0.95	9.97	9.53
0.24	4.11	3.50	(3.48,3.53)	1.48	(1.45,1.50)	1.84	14.20	12.96
0.24	3.57	4.02	(4.00,4.04)	2.05	(2.04,2.09)	2.22	23.34	9.51
0.18	5.33	3.77	(3.74,3.79)	1.73	(1.71,1.76)	1.10	4.94	22.19
0.18	4.29	4.03	(4.02,4.05)	1.96	(1.94,1.37)	1.18	7.89	14.96
0.18	3.57	2.88	(2.86,2.90)	2.20	(2.19,2.22)	1.23	11.96	10.27
0.18	3.13	3.00	(2.98,3.02)	2.10	(2.09,2.12)	1.33	14.49	9.17
0.18	2.70	2.93	(2.91,2.97)	2.22	(2.21,2.24)	1.86	19.10	9.74

Table A.3: Accuracy and outcomes of the wave experiments

T (s)	A (m)	C_D	Bounds	C_M	Bounds	F_{max} (N)	RMSE (N)	accuracy fit (%)
3.69	0.08	2.28	(2.25,2.30)	1.90	(1.88,1.92)	7.75	0.79	10.14
3.69	0.11	2.45	(2.43,2.46)	1.59	(1.57,1.60)	10.16	1.22	12.04
2.73	0.13	2.48	(2.46,2.50)	1.76	(1.74,1.77)	14.05	1.87	13.31
1.19	0.03	65.98	(65.90,66.08)	2.70	(2.69,2.70)	4.21	0.01	0.16
5.24	0.10	2.77	(2.75,2.80)	1.07	(1.05,1.10)	6.65	0.60	8.95
5.24	0.07	2.71	(2.68,2.74)	2.86	(2.83,2.86)	4.42	0.39	8.91
3.69	0.08	2.77	(2.74,2,79)	2.24	(2.22,2.25)	8.22	1.21	14.71
3.69	0.11	2.67	(2.65,2.68)	1.71	(1.70,1.73)	9.48	1.10	11.57
2.73	0.13	2.19	(2.18,2.21)	2.02	(2.00,2.04)	14.89	1.87	12.56
1.19	0.03	15.34	(14.98,15.71)	3.26	(3.25,3.28)	4.14	0.10	2.46

A.1. Force measurement error

B

Experiment

B.1. Standing wave

A standing wave in water is a wave that does not propagate through space but instead oscillates in a fixed pattern. This type of wave is also known as a ”stationary wave” or ”standing wave pattern.” It is formed when two waves of equal amplitude and frequency, but opposite phases, interfere with each other. This can occur when a wave is reflected by a barrier, such as a shoreline or a dam, or when two waves are generated by opposing sources, such as wind or currents. The resulting pattern is characterized by a series of crests and troughs that do not move along the water surface but instead remain in a fixed position as shown in figure B.2 (Rodriguez, Triana, and Ortiz 2019).

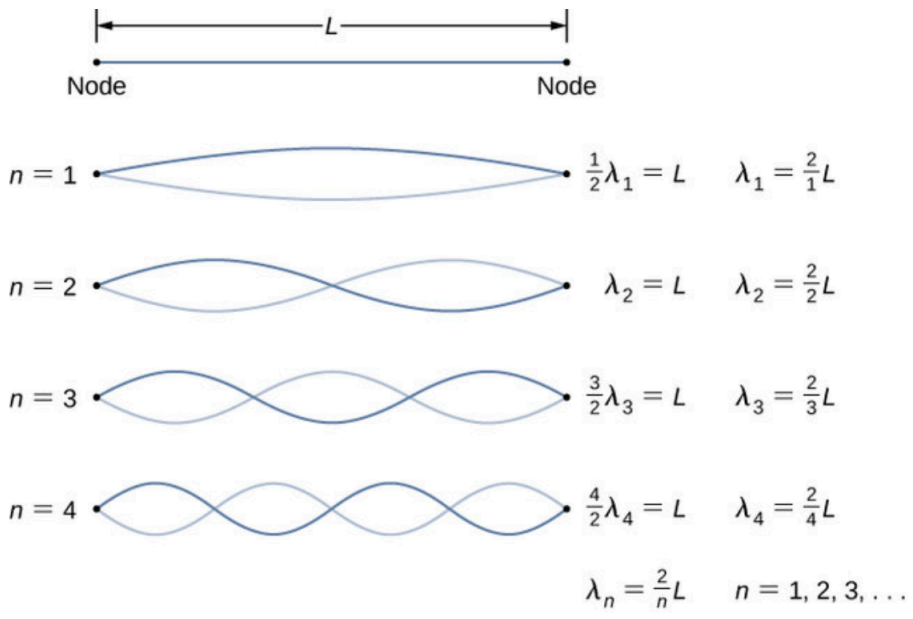

Figure B.1: Different standing waves with nodes

During the zero measurements in the wave tank, a long wave with a period of 50 seconds was measured. According to calculations using the appropriate depth, the wavelength was around 170 meters. The wavelength is exactly twice the length of the wave tank, which means the wave is a standing wave in the tank. Waves are movements of the water, so when towing, the speed of the water also influences the forces.

In this case the wave is in the second mode. In the wave tank, this would result in the following. In this image, red and blue have a phase shift of 180 degrees, and the node is in the middle of the wave tank. The amplitude is the distance between the dotted and the red or blue line. To calculate the speed of the water due to the wave, the following formula can be used:

$$u = \frac{agk}{\omega} \frac{cosh(kz + kd)}{cosh(kd)} cos(kx - \omega t) \tag{B.1}$$

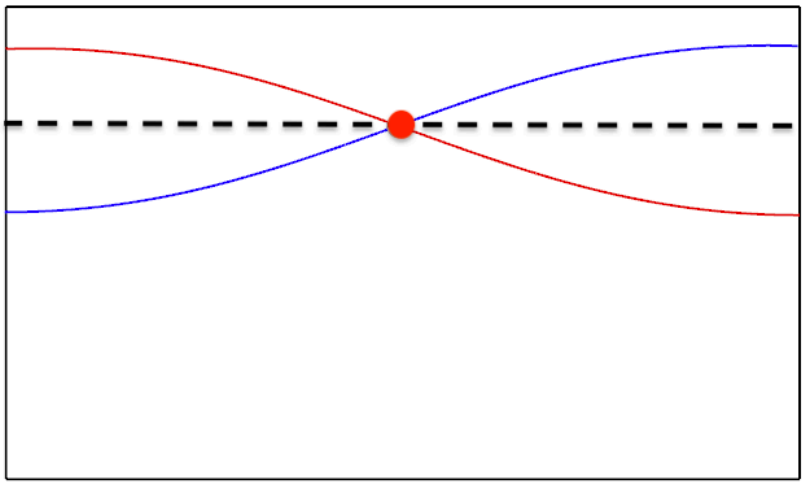

Figure B.2: Standing wave in the tank

A standing wave with an amplitude of for example 1 mm at the height of the model and with the appropriate depth has a horizontal speed of 0.03 m/s. In all the test runs the force of this standing wave is negligible.

B.2. Morison equation on horizontally orientated cylinders

The Morison equation holds for slender vertical cylinders in waves. In this case, the slender cylinder is horizontally orientated, so it is necessary to take into account the elliptical orbits of water particles, therefore the hydrodynamic forces acting on a horizontal cylinder are represented in vector form. It is assumed that the kinematics and associated forces are aligned as depicted in figure B.3.

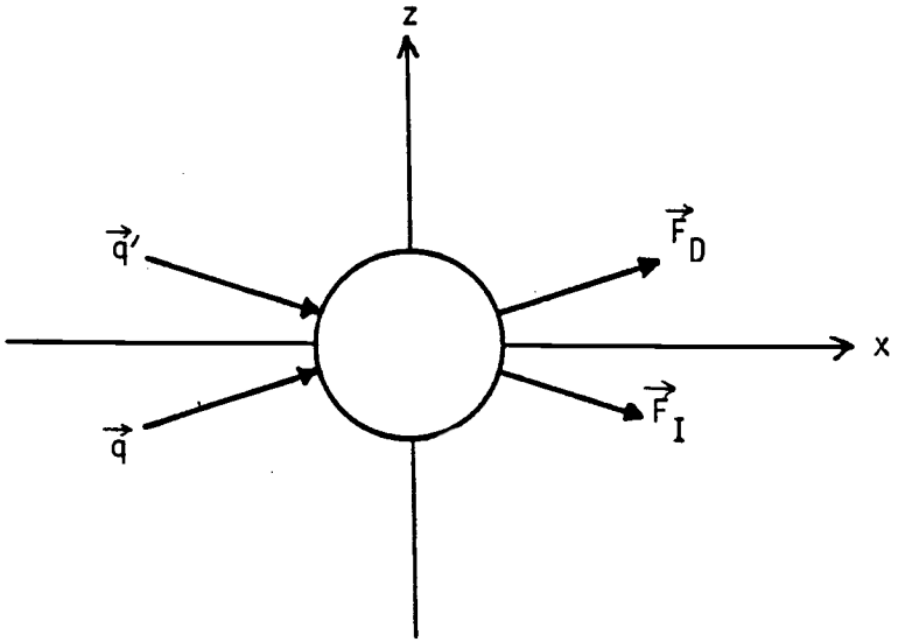

Figure B.3: Wave force and directions of the different components

The vector will rotate around the cylinder so the drag force will have a constant force where the direction differs. In the case of the experiment, the force is solely measured in the x-direction, which means a sinusoidal force is measured. The inertial part of the Morison is always a sinusoidal function with a phase difference. So, the total Morison force on a horizontal cylinder in waves is a sinus instead of the characteristic form.

In the original Morison equation, the non-sinusoidal function is caused by the squared velocity with an absolute component. A vertical cylinder has a moment in time where the drag alters due to the non-consistency of the cylindrical shape when it is upright. This happens at the oscillations as well because the oscillation resembles the wave movement. In the instance that the speed is zero, there is no flow around the cylinder. So for the oscillation experiment, the cylinder can be regarded as a vertically orientated cylinder. The direction does not change but the amplitude does. This has the same effect on the drag force as in the original Morison equation.

C

Data process theory

C.1. Natural frequencies

The PSDs for the test runs where the natural frequencies were triggered are shown for every direction. The scales do differ due to the difference in power of the frequencies. The natural frequencies of the system in the z-direction are shown in C.3, where the small peaks are around 5, 7, and 28 Hz, and the big peaks are around 8, 14, and 31 Hz.

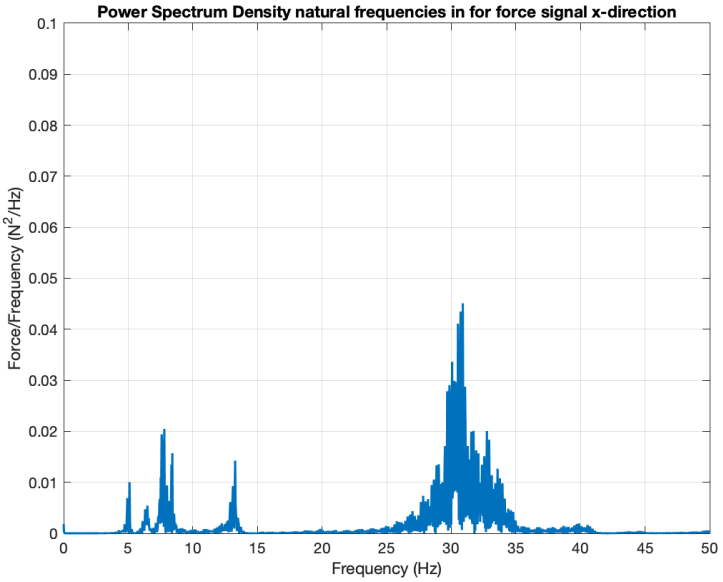

Figure C.1: The PSD of the natural frequencies in x-direction

The natural frequencies of the system in the y-direction are shown in C.2, where the small peaks are around 5,7,17, 21, 33, 34, and 42 Hz, and the big peaks are around 8, and 14 Hz.

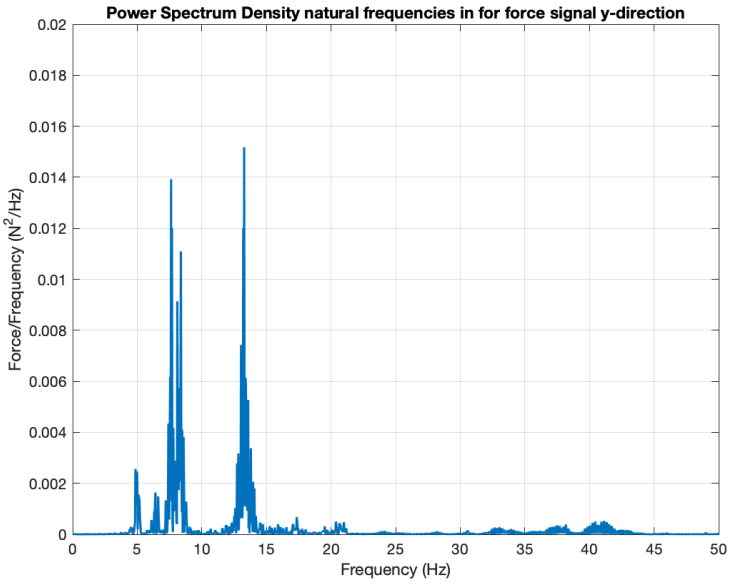

Figure C.2: The PSD of the natural frequencies in y-direction

The natural frequencies of the system in the z-direction are shown in C.3, where the small peaks are around 5, 7, and 28 Hz, and the big peaks are around 8 and 14 Hz.

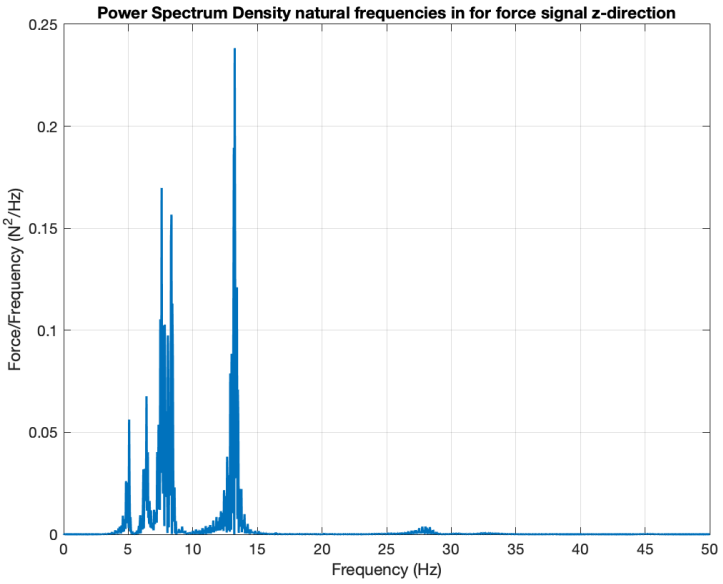

Figure C.3: The PSD of the natural frequencies in z-direction

C.2. PSD of boundaries oscillation experiment

Here the PSDs of the boundaries of the forced oscillation experiments are shown. In figure C.4 the PSDs with the upper bound of the amplitude and both bounds of the frequency is shown and in figure C.5 the PSDs with the upper bound of the amplitude and both bounds of the frequency.

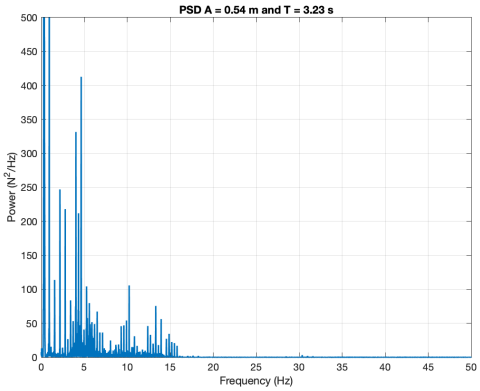

(a) PSD of A = 0.54 m and T = 3.23 s

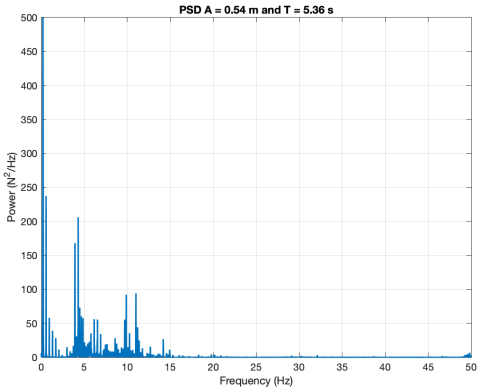

(b) PSD of A = 0.54 m and T = 5.36 s

Figure C.4: PSDs with upper bound of amplitude and both bounds of frequency

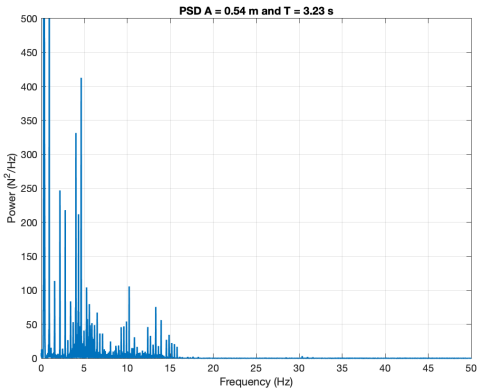

(a) PSD of A = 0.18 m and T = 2.7 s

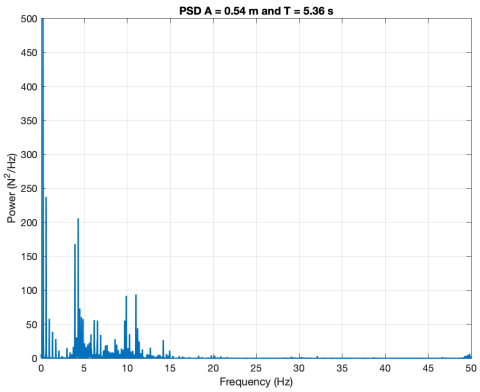

(b) PSD of A = 0.18 m and T = 5.32 s

Figure C.5: PSDs with upper bound of amplitude and both bounds of frequency

C.3. Filter determination

A low-pass filter must be used to acquire the right signal. The low-pass filters come in several varieties, each with unique advantages and disadvantagesThompson 2014. Several of the most popular low-pass filters are listed below:

- Moving Average Filter: This uncomplicated low-pass filter computes the current output by averaging the previous ”n” samples. This kind of filter works best in situations requiring a simple implementation with constrained computational resources.
- Similar to the moving average filter, the weighted moving average filter multiplies each sample by a weighting factor before averaging it. Applications, where greater control over the frequency response is sought, are best suited for this kind of filter.
- Gaussian Filter: This is a type of low-pass filter that uses a Gaussian function to weigh the samples. This kind of filter is suitable for applications where a smooth frequency response is sought since the Gaussian function has the desirable property of being a smooth and bell-shaped curve.
- Butterworth Filter: This is a type of low-pass filter that uses a polynomial function to weigh the samples. Butterworth filters are known for having a flat frequency response in the passband, and a rapid roll-off in the stopband. This type of filter is well suited for applications where a flat frequency response is desired.
- Chebyshev Filter: This kind of low-pass filter weights the samples using a Chebyshev polynomial function. Chebyshev filters are renowned for having a sharp stopband roll-off and a passband

frequency response that is almost ripple-like. This kind of filter works well in situations when a quick roll-off is required yet some passband ripple is acceptable.

The low-pass filter you use will depend on the application's particular needs. The Gaussian and Butterworth filters, respectively, are often well suited for applications where a smooth and flat frequency response is sought. The moving average, weighted moving average, and Chebyshev filters are ideal for applications that require a rapid and simple implementation or where computational resources are limited.
Since there is no need for a simple and rapid implementation, but it is better done in a thorough method the choice is between the Gaussian and Butterworth filters. The frequencies that need to be filtered often are close to each other therefore a flat frequency response is a necessary requirement so the Butterworth filter is used in this research.

C.3.1. Butterworth filter elaboration

The Butterworth filter is implemented as an analog filter, or as a digital filter using an equivalent transfer function. This transfer function is as follows:

$$|H(j\omega)| = \frac{1}{\sqrt{1 + (\frac{\omega}{\omega_c})^{2n}}} \tag{C.1}$$

Where ”s” is the complex frequency variable, ”ωc” is the cutoff frequency, and ”n” is the order of the filter. The order of the filter determines the steepness of the roll-off in the stopband. The higher the order, the steeper the roll-off.

C.4. Differentiation of position signal

A method to overcome this problem is by reducing the sampling rate, so the distance between data points increases, which makes it possible to more accurately resolve changes in position. The data points can be reduced by downsampling or taking the moving average of the signal

Downsampling

Downsampling is done by selecting the nth sample of the original signal where n is the downsampling factor. For example, if the downsampling factor is 2, every second sample is retained, and the rest are discarded. The downside of downsampling is that it can lead to loss of information, for example, aliasing. Aliasing happens when the sampling rate is insufficient to fully record all of the frequency components of the signal. As a result, the reconstructed signal contains errors because high-frequency signal components are mistaken for low-frequency ones.

Downsampling also has the potential to amplify existing noise in the signal. This is due to the fact that by downsampling the signal the number of measurements made is reduced, which raises the signal's uncertainty. As a result, the signal may lose resolution and precision.

Moving average

Another way to make the position signal differentiable is to use a moving average. A moving average smooths out a signal by calculating the average value of the signal over a certain period of time. The moving average can lower the signal's noise and make it simpler to distinguish small changes in position. It is crucial to remember that a moving average will also inject a delay into the signal and may result in a loss of resolution.

Additionally, the size of the window, the time frame over which the average is calculated, must be chosen carefully. A signal will be more responsive to changes in position when the window size is small, but it will also be more susceptible to noise. A signal will be less responsive to changes in position as a result of a bigger window size, but it will also be less vulnerable to noise. It is important to experiment with various window sizes and pick the one that best satisfies the unique needs of the application.

In conclusion, a moving average can be applied to a position signal to enable differentiation between

small changes in position. However, it is crucial to remember that this will cause a delay in the signal and may result in a loss of resolution, so it is crucial to carefully select the window size.

In this data processing campaign, the moving average method will be employed as it effectively reduces the noise present in the signal while the delay introduced can be compensated for. Additionally, the signal under examination is assumed to be a sinusoidal wave, making the selection of an appropriate window size easier as the deviation from the original signal can be easily identified when the averaged signal is no longer representative. The use of the moving average method in conjunction with the sinusoidal nature of the signal ensures a more accurate differentiation for the acquisition of the velocity and acceleration signal.

C.4.1. Fit functions

The Nonlinear Least Squares formulation is used by the Curve Fitting Toolbox to fit a nonlinear model to data. An equation with nonlinear coefficients, or one with both linear and nonlinear coefficients, is referred to as a nonlinear model. For instance, power functions, polynomial ratios, and Gaussians are all nonlinear (Mathworks 2001).

In matrix form, nonlinear models are given by the formula:

$$y = f(X, \beta) + \epsilon \tag{C.2}$$

where:

- y is an n-by-1 vector of responses
- f is a function of β and X
- β is a m-by-1 vector of coefficients
- X is the n-by-m design matrix for the model
- ϵ is an n-by-1 vector of errors

Since simple matrices cannot be used to predict the coefficients, nonlinear models are more challenging to fit than linear models. Instead, an iterative strategy that adheres to the following phases is needed:

1. Start by estimating each coefficient's initial value. A heuristic method is presented for several nonlinear models and yields plausible beginning points.
2. Produce the fitted curve for the current set of coefficients. The fitted response value $\hat{y}$ is given by:
$$\hat{y} = f(X, b) \tag{C.3}$$
and involves the calculation of the Jacobian of $f(X, b)$, which is defined as a matrix of partial derivatives taken with respect to the coefficients.
3. Check to see whether the fit becomes better by adjusting the coefficients. The fitting algorithm determines the direction and size of the modification. These algorithms are:
   (a) Trust-region — This approach must be used if coefficient constraints have to be set because it is the default. It is an enhancement over the well-known Levenberg-Marquardt algorithm and can solve challenging nonlinear problems more effectively than the other algorithms.
   (b) Levenberg-Marquardt - Since it has been in use for so long, this technique has consistently shown to be effective for a variety of nonlinear models and beginning points. Try the Levenberg-Marquardt approach if the trust-region algorithm fails to yield an acceptable fit and you do not have coefficient limitations.
   (c) The Gauss-Newton - This algorithm may be quicker than the other algorithms. However, it makes the assumption that the residuals are almost zero. For the majority of models and data sets, it should be the very last option even if it is included in the toolbox for instructional purposes.
4. Iterate the process by returning to step 2 until the fit reaches the specified convergence criteria.

For nonlinear models, you can employ weights and robust fitting, and the fitting procedure is adjusted as a result. Also bound per parameter can be set to minimize the iterations done.

C.4.2. Elaboration on fitting algorithms

There are several reasons why one might choose to use the trust-region method instead of the Levenberg-Marquardt method:

Global convergence: Trust-region methods are known to converge globally, meaning they are guaranteed to find the global minimum of the objective function. In contrast, Levenberg-Marquardt methods can only guarantee local convergence, meaning they may only find a local minimum.

1. Numerical stability: Trust-region methods are more stable numerically than Levenberg-Marquardt methods, as they do not require the computation of the inverse of the Jacobian matrix.
2. Robustness to ill-conditioning: Trust-region methods are more robust to ill-conditioned objective functions, as they are not affected by the condition number of the Jacobian matrix.
3. Handling non-quadratic objective functions: Trust-region methods can handle non-quadratic objective functions more effectively, as they do not rely on the assumption that the objective function is approximately quadratic.
4. Better control over step size: In the trust-region method, the step size is controlled by the trust region, which can be adjusted dynamically during the optimization process. This allows for better control over the step size, which can improve the convergence rate of the optimization process.

In conclusion, the trust-region method may be preferred over the Levenberg-Marquardt method for optimization problems that are ill-conditioned, have non-quadratic objective functions, or require more control over the step size. However, the choice of method will ultimately depend on the specific problem being solved and the desired trade-off between computational efficiency and solution accuracy.

C.4.3. Robust least squares

It is typically expected that response errors follow a normal distribution and that high values are uncommon. Outliers, or extreme values, do nevertheless exist. Least squares fitting's key drawback is its sensitivity to outliers. Because squaring the residuals multiplies the effects of these extreme data points, outliers have a significant impact on the fit. You can use robust least squares regression to fit your data and reduce the impact of outliers(Mathworks 2001). These two reliable regression approaches are offered by the toolbox:

1. Least absolute residuals (LAR) — Rather of minimizing the squared differences between the residuals, the LAR scheme seeks a curve that minimizes the absolute difference between the residuals. Extreme values hence have less of an impact on the fit.
2. Bisquare weights — This method minimizes a weighted sum of squares, with each data point receiving a different weight based on how far away from the fitted line it is. Nearby points are given full weight. The weight of points farther from the line is diminished. Points that are further from the line than is consistent are given no weight. Because it simultaneously aims to construct a curve that fits the majority of the data using the conventional least squares approach and minimizes the impact of outliers, the bisquare weight scheme is generally favored over LAR.

Since the signal is filtered it has no real outliers. So, the use of a robust function is not necessary.

C.5. Confidence and prediction bounds

Prediction bounds can be computed for new observations or for the fitted function as well as confidence bounds for the fitted coefficients. Furthermore, you can compute simultaneous bounds for prediction bounds, which consider all predictor values, or non-simultaneous bounds, which consider only individual predictor values. The prediction bounds are shown graphically, but the confidence bounds are numerical.

The corresponding interval's lower and higher values, as well as its width, are determined by the prediction and confidence boundaries. How confident you are in the projected observation, forecast fit, or fitted coefficients is shown by the range of the interval. For instance, a very wide interval for the fitted coefficients may suggest that you need to fit with more data before making any firm conclusions about the coefficients.

The degree of confidence with which the boundaries are defined can be chosen. The degree of confidence is frequently 95%, although it can also be any number, including 90%, 99%, 99.9%, and so forth. For instance, a 5% probability of being wrong can suffice while making a prediction on a brand-new observation. Then determine a 95% prediction interval is needed. With a 95% confidence interval, it is very sure that the new observation will fall within the lower and higher prediction ranges(Mathworks 2001).

For this research the prediction and confidence bounds are both set at 95 %. Especially for the confidence bounds a high percentage of accuracy is required since those give the wanted results of the experiments. This gives the most accurate possible results for this research.

C.6. Goodness of fits

The goodness of fit statistics should be looked at after assessing the goodness of fit graphically. For parametric models the following goodness of fit statistics are used(Mathworks 2001):

- Sum of squares due to error: This statistic calculates the overall deviation between the response values and the response values' fit. It is frequently abbreviated as SSE and is also known as the summed square of residuals.

$$SSE = \sum_{i=1}^{n} w_i (y_i - \hat{y}_i)^2 \tag{C.4}$$

  A value that is nearer to 0 denotes a better fit.
- R-square: This measures how well the fit accounts for the data's fluctuation. R-square, or correlation square, measures the relationship between actual and expected response values. It is also known as the coefficient of multiple determination and the square of the multiple correlation coefficient. The ratio of the sum of squares from the regression (SSR) to the entire sum of squares is known as R-square (SST). SSR is defined by:

$$SSR = \sum_{i=1}^{n} w_i (\hat{y}_i - \bar{y})^2 \tag{C.5}$$

  SST is also called the sum of squares about the mean and is defined as:

$$SST = \sum_{i=1}^{n} w_i (y_i - \bar{y})^2 \tag{C.6}$$

  where SST = SSR + SSE. Given these definitions, R-square is expressed as:

$$R_{square} = \frac{SSR}{SST} = 1 - \frac{SSE}{SST} \tag{C.7}$$

  Any value between 0 and 1 can be assigned to R-square, with a value nearer 1 indicating a better fit. An R2 value of 0.8234, for instance, indicates that the fit accounts for 82.34% of the overall variation in the average data. R-square may rise if you add more fitted coefficients to your model, but the fit might not get better. In that case, the degrees of freedom adjusted R-square statistic can be used
- adjusted R-square: This statistic makes use of the R-square statistic previously described and modifies it according to the remaining degrees of freedom. The number of response values n less the number of fitted coefficients m calculated from the response values is known as the residual degrees of freedom.

$$v = n - m \tag{C.8}$$

  In order to calculate the sum of squares, n data points must be involved in v separate bits of information. Be aware that estimations are considered fixed if parameters are constrained and one or more of the estimates are at their boundaries. The quantity of these parameters raises the

degrees of freedom. When you include more coefficients in your model, the adjusted R-square statistic is typically the best measure of the fit quality.

$$adjustedR_{square} = 1 - \frac{SSE(n-1)}{SST(v)} \tag{C.9}$$

The adjusted R-square statistic can take on any value less than or equal to 1, with a value closer to 1 indicating a better fit.

- Root mean squared error: This statistic is also referred to as the fit standard error and the regression standard error.

$$RMSE = s = \sqrt{MSE} \tag{C.10}$$

where MSE is either the residual mean square error or the mean square error

$$MSE = \frac{SSE}{v} \tag{C.11}$$

An RMSE value closer to 0 indicates a better fit.

Due to the huge amount of data points the SSE can become really large, therefore the RMSE says more about the goodness of the fit. The RMSE is also an absolute number so with higher values in the signal it tends to be a relatively better fit than with the same lower values in the signal.

D

Towing results and calibration

D.1. Calibration

Before conducting the experiments the force transducers had to be calibrated. The calibration is done by clamping the force transducer onto a table and starting the force measurement. From then on every 30 seconds, a mass is added seven times, and from a maximum mass of 8 kg every 30 seconds, a mass is subtracted for seven times. The data of this force measurement is implemented in the calibration sheet of figure D.2 and D.3. Using this method both transducers are calibrated. The units to calculate the right force are according to ITTC standards and given in figure D.1.

ITTC-STANDARD			
g value ncg:	9.812	m/s^2	
calculation air density:	1.199	kg/m^3	
correction =	0.9999	[-]	
F = mg*correction			
	09-12-2022	r'dam airport	
ambient pressure	09:00	1006.4	hPa
R (gas-constant)		0.28669	kJ/(kg K)
universal gas constant		8.314	kJ/(kmol K)
molar mass		29	kg/kmol
room temperature		19.7	deg C
absolute temperature		292.85	K
		1kg mean	
		0.99931	kg

Figure D.1: ITTC standards used for calibration

					[kg]	[kg]	[V]	[V]	[N]	[V]	[V]	%
date	9-Dec-22			step	mass step	massa	U	U correct	F	U calc	Residual	norm Res
				1	0.00	0.53	0.52	0.48	5.19	0.49	-0.0016	-0.010%
chan	3			2	1.00	1.53	1.43	1.40	14.99	1.40	-0.0014	-0.009%
name	Kracht 1			3	2.00	2.53	2.35	2.32	24.80	2.32	-0.0009	-0.006%
				4	3.00	3.53	3.26	3.23	34.60	3.23	-0.0007	-0.004%
				5	5.00	5.53	5.09	5.06	54.21	5.06	0.0004	0.002%
sensor no	PB115735			6	6.00	6.52	6.01	5.98	64.01	5.98	0.0006	0.004%
range	8	kg	positive	7	7.00	7.52	6.92	6.89	73.82	6.89	0.0007	0.004%
				8	8.00	8.52	7.84	7.81	83.62	7.81	0.0008	0.005%
amplifier	PICAS			9	7.00	7.52	6.92	6.89	73.82	6.89	0.0008	0.005%
range in	2	mV/V		10	6.00	6.52	6.01	5.98	64.01	5.98	0.0008	0.005%
range out	10	V		11	5.00	5.53	5.09	5.06	54.21	5.06	0.0007	0.004%
R neutral	-7.68	uV/V		12	3.00	3.53	3.26	3.23	34.60	3.23	-0.0001	-0.001%
C neutral	373.3	uV/V		13	2.00	2.53	2.35	2.32	24.80	2.32	-0.0006	-0.004%
				14	1.00	1.53	1.43	1.40	14.99	1.40	-0.0012	-0.007%
calfact	10.714	N/V		15	0.00	0.53	0.52	0.49	5.19	0.49	-0.0009	-0.006%
slope	0.0933	V/N		1	0.00	-0.53	-0.53	-0.48	-5.19	-0.48	-0.0001	-0.001%
intercept	0.0016	V		2	1.00	-1.53	-1.45	-1.40	-14.99	-1.40	-0.0001	0.000%
				3	2.00	-2.53	-2.36	-2.31	-24.80	-2.31	0.0000	0.000%
				4	3.00	-3.53	-3.28	-3.23	-34.60	-3.23	0.0002	0.001%
				5	5.00	-5.53	-5.11	-5.06	-54.21	-5.06	0.0002	0.001%
Measured val (see orange box for ref.				6	6.00	-6.52	-6.02	-5.97	-64.01	-5.97	0.0006	0.004%
offset standing upright				7	7.00	-7.52	-6.94	-6.89	-73.82	-6.89	0.0003	0.002%
-0.0056	V			8	8.00	-8.52	-7.85	-7.80	-83.62	-7.80	0.0009	0.005%
hanging positive bare				9	7.00	-7.52	-6.94	-6.89	-73.82	-6.89	0.0003	0.002%
0.0325	V			10	6.00	-6.52	-6.02	-5.97	-64.01	-5.97	0.0006	0.004%
hanging positive with hook plate				11	5.00	-5.53	-5.11	-5.06	-54.21	-5.06	0.0001	0.001%
	V			12	3.00	-3.53	-3.28	-3.23	-34.60	-3.23	0.0001	0.001%
hanging positive with plate and hanger				13	2.00	-2.53	-2.36	-2.31	-24.80	-2.31	0.0001	0.001%
0.516	V			14	1.00	-1.53	-1.45	-1.40	-14.99	-1.40	-0.0002	-0.002%
hanging negative with hook plate				15	0.00	-0.53	-0.53	-0.48	-5.19	-0.48	-0.0003	-0.002%
-0.5326	V											
hanging negative with plate and hanger				mass hange	529							
	V			g				positive	negative			
hanging negative bare				mass plate	0		slope	0.09337	0.09333			
-0.0499	V			g			intercept	0.0001	0.0014	-0.0012		
				attachments to sensor								
				0.529	kg							

Figure D.2: Calibration force sensor 1

					[kg]	[kg]	[V]	[V]	[N]	[V]	[V]	%
date	9-Dec-22			step	mass step	massa	U	U correct	F	U calc	Residual	norm Res
				1	0.00	0.53	0.52	0.49	5.19	0.48	0.0045	0.029%
chan	4			2	1.00	1.53	1.44	1.40	14.99	1.40	0.0035	0.023%
name	Kracht 2			3	2.00	2.53	2.36	2.32	24.80	2.32	0.0035	0.022%
				4	3.00	3.53	3.27	3.24	34.60	3.23	0.0026	0.016%
				5	5.00	5.53	5.10	5.07	54.21	5.07	0.0010	0.007%
sensor no	PB107404			6	6.00	6.52	6.02	5.99	64.01	5.99	0.0001	0.001%
range	8	kg		7	7.00	7.52	6.93	6.90	73.82	6.90	-0.0016	-0.010%
				8	8.00	8.52	7.85	7.82	83.62	7.82	-0.0024	-0.016%
amplifier	PICAS			9	7.00	7.52	6.93	6.90	73.82	6.90	-0.0018	-0.012%
range in	2	mV/V		10	6.00	6.52	6.02	5.99	64.01	5.99	-0.0002	-0.001%
range out	10	V		11	5.00	5.53	5.10	5.07	54.21	5.07	0.0007	0.005%
R neutral	-13.497	uV/V		12	3.00	3.53	3.27	3.24	34.60	3.23	0.0023	0.015%
C neutral	394.42	uV/V		13	2.00	2.53	2.36	2.32	24.80	2.32	0.0034	0.022%
				14	1.00	1.53	1.44	1.40	14.99	1.40	0.0035	0.022%
calfact	10.693	N/V		15	0.00	0.53	0.52	0.49	5.19	0.48	0.0045	0.029%
slope	0.0935	V/N		1	0.00	-0.53	-0.53	-0.49	-5.19	-0.49	-0.0057	-0.036%
intercept	-0.0010	V		2	-1.00	-1.53	-1.45	-1.41	-14.99	-1.40	-0.0047	-0.030%
				3	-2.00	-2.53	-2.36	-2.32	-24.80	-2.32	-0.0045	-0.029%
				4	-3.00	-3.53	-3.28	-3.24	-34.60	-3.24	-0.0031	-0.020%
				5	-5.00	-5.53	-5.11	-5.07	-54.21	-5.07	-0.0007	-0.005%
Measured val (see orange box fo				6	-6.00	-6.52	-6.03	-5.99	-64.01	-5.99	0.0005	0.003%
offset standing upright				7	-7.00	-7.52	-6.94	-6.90	-73.82	-6.90	0.0023	0.015%
-0.0075	V			8	-8.00	-8.52	-7.86	-7.82	-83.62	-7.82	0.0039	0.025%
hanging positive bare				9	-7.00	-7.52	-6.94	-6.90	-73.82	-6.90	0.0026	0.016%
0.0336	V			10	-6.00	-6.52	-6.03	-5.99	-64.01	-5.99	0.0008	0.005%
hanging positive with hook plate				11	-5.00	-5.53	-5.11	-5.07	-54.21	-5.07	-0.0004	-0.003%
	V			12	-3.00	-3.53	-3.28	-3.24	-34.60	-3.24	-0.0027	-0.017%
hanging positive with plate and ha				13	-2.00	-2.53	-2.36	-2.32	-24.80	-2.32	-0.0035	-0.022%
0.5227	V			14	-1.00	-1.53	-1.45	-1.41	-14.99	-1.40	-0.0037	-0.024%
hanging negative with hook plate				15	0.00	-0.53	-0.53	-0.49	-5.19	-0.49	-0.0048	-0.031%
-0.5317	V											
hanging negative with plate and hanger				mass hang	529							0.029%
	V			g				positive	negative			
hanging negative bare				mass plate	0		slope	0.09343	0.09341			
-0.0396	V			g			intercept	0.0042	-0.0074			
				attachments to sensor								
				0.529	kg							

Figure D.3: Calibration force sensor 2

The other way to calculate the C_D is by using the mean and standard deviation calculated in table 6.1. The standard deviation of the C_D is calculated using error propagation, which calculates how the errors in parameters affect the outcomes' standard deviation. The velocity and force are assumed to be correlated. The last term in the equation accounts for that.

$$\sigma_{C_D} = C_{Dmean} * \sqrt{((2 * \frac{\sigma_v}{v_{mean}})^2 + (\frac{\sigma_F}{F_{mean}})^2) - 2 * \frac{\sigma_{Fv}}{F_{mean} * v_{mean}})} \tag{D.1}$$

The outcomes are shown in table D.1

Table D.1: C_D computed using error propagation

Reynolds mean	Calculated C_D Mean	σ	Cov (%)
$9.6 * 10^4$	1.19	0.011	0.96
$7.9 * 10^4$	1.19	0.011	0.93
$6.2 * 10^4$	1.17	0.012	1.2
$4.5 * 10^4$	1.17	0.021	1.79
$2.8 * 10^4$	1.16	0.036	3.14

The CoV of table D.1 is higher than the ones, which means that the assumption of correlation is false. As stated earlier in the results the force and velocity are not correlated and this emphasizes that.

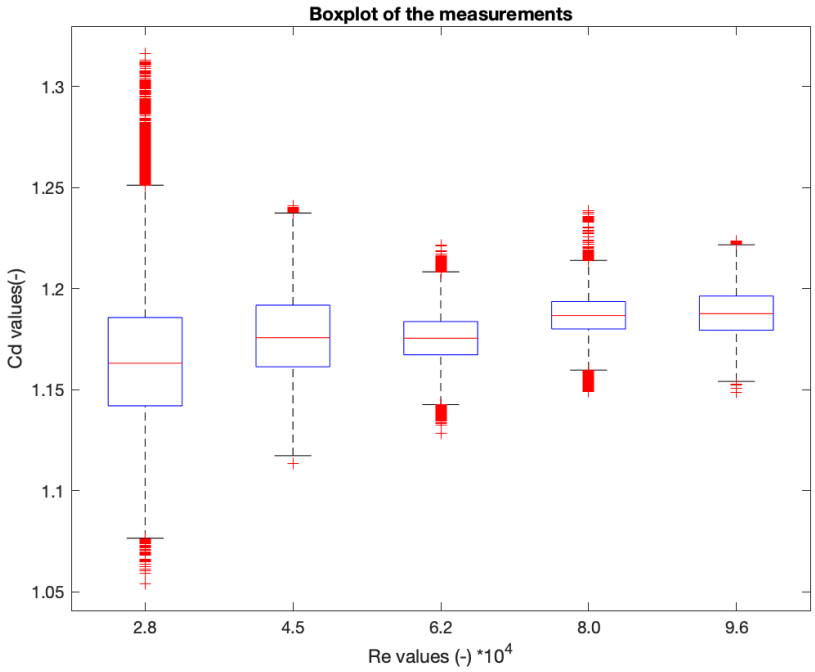

Figure D.4: Boxplots of the different measurements, where the red crosses are the outliers, the red line is the median, and the blue box is the domain of the 25th and 75th percentile

D.2. Measurement uncertainty

After measurement uncertainty that follows out of the calibration is 0.01 % and 0.03 % over 80 N. As the constant force used for calculating the C_D differs from 2.5 N to 25 N the uncertainty in that measurement is different as well. The absolute uncertainty is the same but the relative uncertainty increases when the force decreases.

To put the CoV calculated in the results in perspective the relative measurement uncertainty is given per test results. First, the percentage of the total force range used for each force transducer is given where F_{U1} is the uncertainty of force transducer 1 and F_{U2} is the uncertainty of force transducer 2. In equation D.2 and D.3 the relative uncertainties per force transducer are calculated, where 1.96 is the confidence interval of 95 % and 0.01 and 0.03 the uncertainty of the force transducers.

$$F_{U1} = \frac{2 * 80}{F_{mean}} * 1.96 * 0.01 \tag{D.2}$$

$$F_{U1} = \frac{2 * 80}{F_{mean}} * 1.96 * 0.03 \tag{D.3}$$

With that percentage, the uncertainty per force transducer is calculated, and that is put into perspective compared to the CoV. The results are shown in table D.2.

Table D.2: Uncertainty of force measurement

Re $*10^4$ (-)	F_{mean} (N)	Range (%)	F_{U1} (%)	F_{U2} (%)	CoV (%)	difference (%)
9.6	25.3	15.8	0.1	0.4	0.9	0.4
7.9	17.3	10.8	0.2	0.6	0.9	0.1
6.2	10.4	6.5	0.3	0.9	1.2	-0.1
4.5	5.5	3.5	0.6	1.7	1.8	-1.1
2.8	2.1	1.3	1.5	4.5	3.1	-2.9

In table D.2 is clearly seen that the uncertainty of the force transducers increases when the force decreases. For the three tests with the lowest Reynolds, the CoV is within the uncertainty in the force

transducers. For the test runs with the highest Reynolds the CoV is slightly higher than the uncertainty in the force transducers. The relative bigger measurement uncertainty can be caused by the higher turbulence in the test with a higher Reynolds.

E

Mussels

In this section, the seven different mussels used for the 3D-printed model are shown. The mussels were chosen due to their different sizes and shapes.

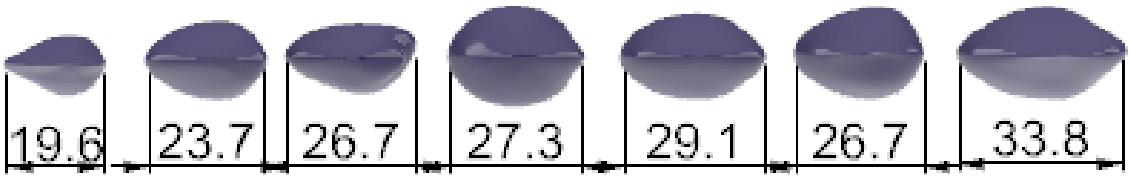

Figure E.1: Front view of the mussels

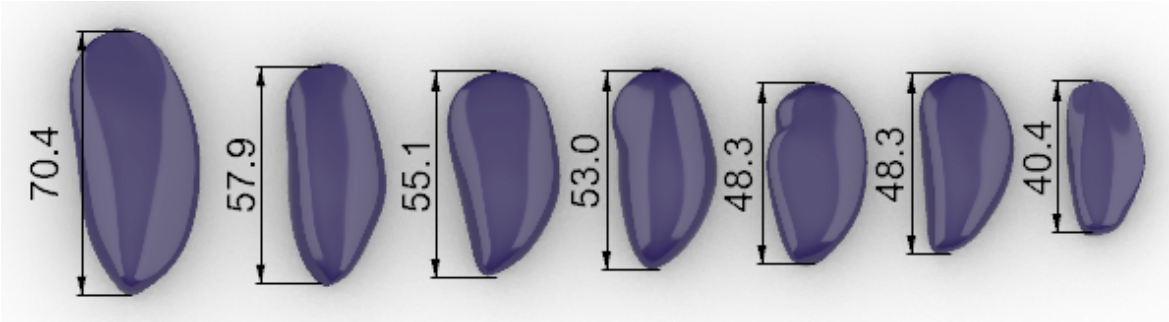

Figure E.2: Top view of the mussels

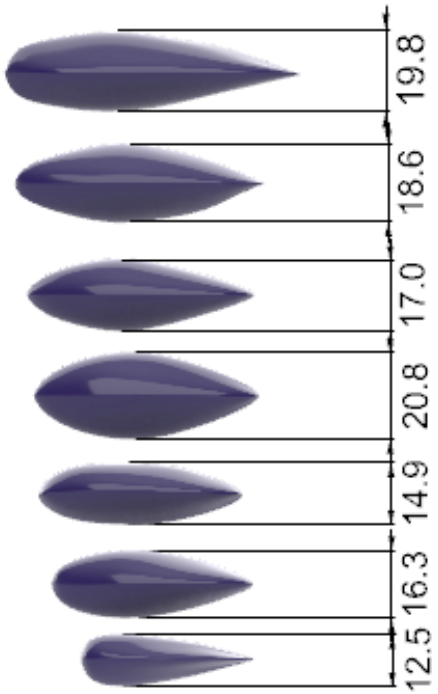

Figure E.3: Side view of the mussels

Figure E.4: Perspective view of the mussels